

GRAN SASSO SCIENCE INSTITUTE

DOCTORAL THESIS

Searching for Core-Collapse Supernovae in the Multimessenger Era: Low Energy Neutrinos and Gravitational Waves

Author:

Odysse HALIM

Supervisor:

Prof. Viviana FAFONE

(supervisor)

Dr. Giulia PAGLIAROLI

(co-supervisor)



*A thesis submitted in fulfillment of the requirements
for the degree of PhD program in Astroparticle physics
in the*

Department of Physics

April 14, 2020

Declaration of Authorship

I, Odysse HALIM, declare that this PhD thesis titled, “Searching for Core-Collapse Supernovae in the Multimessenger Era: Low Energy Neutrinos and Gravitational Waves” and the work presented in it are my own. I confirm that:

- This work was done wholly or mainly while in candidature for a research degree at this Institute.
- Where any part of this thesis has previously been submitted for a degree or any other qualification at this Institute or any other institution, this has been clearly stated.
- Where I have consulted the published work of others, this is always clearly attributed.
- Where I have quoted from the work of others, the source is always given. With the exception of such quotations, this thesis is entirely my own work.
- I have acknowledged all main sources of help.
- Where the thesis is based on work done by myself jointly with others, I have made clear exactly what was done by others and what I have contributed myself.

Signed and Date:

“As far as the laws of mathematics refer to reality, they are not certain; and as far as they are certain, they do not refer to reality.”

Albert Einstein

“All around us are people, of all classes, of all nationalities, of all ages. For three days these people, these strangers to one another, are brought together. They sleep and eat under one roof, they cannot get away from each other. At the end of three days they part, they go their several ways, never, perhaps, to see each other again.”

Agatha Christie, Murder on the Orient Express

“The truth, however ugly in itself, is always curious and beautiful to seekers after it.”

Agatha Christie, The Murder of Roger Ackroyd

GRAN SASSO SCIENCE INSTITUTE

Abstract

Searching for Core-Collapse Supernovae in the Multimessenger Era: Low Energy Neutrinos and Gravitational Waves

by Odysse HALIM

Core-collapse supernovae are fascinating astrophysical objects still puzzling the mind of scientists. Despite the big efforts spent on developing very complex numerical simulations, the mechanism driving the final explosion of the star structure is still not completely understood. Gravitational waves are expected to carry away an imprint of this explosion mechanism, however their detections could be very challenging. Moreover, the modelling of the gravitational wave impulsive emission is also challenging because of the stochastic nature of the dynamics and the landscape of possible progenitors. Low-energy neutrinos will be copiously emitted at the same time during the core-collapse explosion and can provide a nice trigger for the gravitational wave search. The aim of this thesis is to develop a multi-messengers approach to search for such interesting astrophysical objects by using a global network of both low-energy neutrino and gravitational wave detectors. In particular, we discuss how to improve the detection potential of the neutrino sub-network by exploiting the temporal behaviour of a neutrino burst from a core-collapse supernova. This will allow us to better disentangle low statistic signals coming from weak or far supernovae from noise. We also discuss the better strategy to combine the informations provided by neutrinos and gravitational waves and we show that the outlined procedure can give us profit as the increased significance of a neutrino burst to achieve a lower false alarm rate of a combined observation of gravitational and neutrino burst.

Keywords: multimessenger, supernova, core-collapse, low-energy neutrino, gravitational wave.

Acknowledgements

I thank my parents. Without their belief and courage of letting me abroad, I would have not been able to arrive at this point in my life.

My happiness is also given by my girlfriend who is always supportive, especially in my depressing moments in my last year of PhD.

I thank Prof. Viviana Fafone, who has introduced and taught me gravitational waves as well as become my supervisor starting from my master to my PhD.

My gratitude is also to Dr. Giulia Pagliaroli for supervising me on this PhD study as well as guiding me on the research life with many fruitful discussions.

Without the supervisions of Prof. Viviana Fafone and Dr. Giulia Pagliaroli, I would have not been able to finish this PhD thesis.

I thank Dr. Marco Drago who advised me for my PhD study, and particularly taught me `cWB pipeline` as well as programming skills in general.

I thank Dr. Claudio Casentini, as a collaborator and as a friend, who contributes on producing simulated data used for the last part of my thesis.

Last but not least, I also thank Dr. Carlo Vigorito, for contributing to make a script for simulated data.

My regard is to [GSSI \(Gran Sasso Science Institute\)](#) for their PhD program and fellowship.

I thank also [INFN \(Istituto Nazionale di Fisica Nucleare\)](#) for their funding in some conferences during my doctoral research.

I thank also [L'Aquila Questura](#) that grant me a permit of stay every year.

I thank my PhD XXXII fellows during this doctorate program, supporting each other emotionally in these 3 years.

Contents

Declaration of Authorship	i
Abstract	iii
Acknowledgements	iv
Introduction	1
1 Core-Collapse Supernovae	4
1.1 Stellar Core-Collapse Progenitors	5
1.2 Standard Picture of Core-Collapse Supernovae	9
1.3 Shock Revival Mechanisms	19
2 CCSN Detectability	23
2.1 Rate and Distribution	23
2.2 Neutrino Emission	28
2.3 GW Emission (Models)	36
3 Detectors, Analyses, and Detections	44
3.1 The Neutrino Channel	44
3.2 The Gravitational Wave Channel	56
3.3 GW Observations by LIGO-Virgo Collaboration	67
4 Multimessenger Efforts	70
4.1 SNEWS: Supernova Early Warning System	70
4.2 $\text{GW}\nu$ Working Group: LIGO-Virgo, LVD, Borexino, IceCube, and KamLAND	71
4.3 Some Multimessenger Searches	72

4.3.1	Scheme of GW-GRB	73
4.3.2	GW-HEN Paper	79
4.4	The Prospect of Quantitative Analysis Application on GW-LEN Joint-analysis	85
5	Coincidence Analysis	86
5.1	Coincidence Analysis between Two Datasets	86
5.2	The Time-shifting Method	88
5.2.1	Comments on Estimating the Livetime and Expected (Pois- son) Number of Coincidences	91
5.3	The Product Method	95
6	Distinguishing Astrophysical Bursts of Low-energy Neutrinos from the Noise	97
6.1	A Simple Double Exponential Model of the CCSN Events in Detector Data Streams	97
6.2	More Details of the Assumption	99
6.2.1	Background and Injection Behavior	99
6.2.2	Matter Effect	101
6.3	Counting Analysis	106
6.4	A New Cut to Improve the Analysis of Neutrino Data to Hunt CCSNe	108
6.5	The Implementation of the Cut Method on the Network of De- tectors	112
7	The Modified Imitation Frequency to Expand CCSN Search Horizon of Neutrino Detectors	117
7.1	The Modified Imitation Frequency with Two Parameters	119
7.2	Comments on the ξ -background Distribution	123
7.3	Application of the Modified Imitation Frequency to Simulated Data	126
7.4	KamLAND Single Detector Analysis Result	129

7.5	Super-K Single Detector Analysis Result	132
7.6	KamLAND-LVD Coincidence Analysis Result	135
7.7	One-module Hyper-K	138
7.8	Perspectives	139
8	GW-ν Joint Search	142
8.1	Joint GW- ν Study Case	144
	Conclusion	150
A	Chandrasekhar Mass Limit	152
B	Gravitational Wave Solutions from Einstein Field Equations	154

List of Figures

1.1	Schematic stellar evolution tracks for different initial stellar masses M_* (taken from [1]).	8
1.2	Onion-like structure of a star during pre-collapse. Only the main elemental constituents in the different shells (containing the products and ashes of the nuclear fusion stages) are indicated. Figure is taken from [7].	10
1.3	Nuclear binding energy as a function of number of nucleons in the nucleus. Figure is taken from [8].	11
1.4	Neutrino luminosity (upper) and average energy (lower) during the collapse. Figure is taken from [11]. This figure indeed is very old and probably the first simulation study, however, the general behaviour of the curve is still relevant to explain a global picture of the neutrino emission. This figure could be compared with figure 2.8.	19
2.1	Probabilities to find one or more CCSNe in the Galaxy for the next 10, 20, and 30 years, depending on the assumed rate. Figure is taken from [26].	26
2.2	PDF of finding CCSNe from our sun towards the galactic center (taken from [27]).	26
2.3	The CCSN rate estimation in the nearby universe, based on 22 supernovae observations in 1999-2008 (bins), compared with the prediction using B-band luminosity (dashed line). Figure is taken from [26]	27

2.4	Observed CCSN cumulative rate as a function of distance (taken from [28]). It is also shown the expected rate based on different electromagnetic emissions and the distances where the detection probability is 90% & 10% for HK (560 kton Hyper-Kamiokande) & 5Mton neutrino detectors. This figure is based on 22 SN observations in 1998-2008 and in comparison with some theoretical predictions.	28
2.5	Expected number of IBD events gathered by KamLAND [34] during the 48 hours before collapse, taking into account ν oscillation effects, as a function of distance. As the case study here, it is shown the flux for a $15M_{\odot}$ and $25M_{\odot}$ star assuming the normal and inverted neutrino hierarchy. The significance levels are shown with the horizontal dotted lines. Figure is taken from [31].	29
2.6	Time evolution of significance. If Betelgeuse star has a mass of $15M_{\odot}$ and with the distance at 150 pc, the 3σ detection by KamLAND [34] (a dotted horizontal line) is 89.6 (7.41) hours with normal (inverted) hierarchy before its collapse. Meanwhile, if the stellar mass is $25M_{\odot}$ at 250 pc, the pre-supernova alert is detectable within 17.0 (4.54) hours before its collapse at 3σ confidence level. Figure is taken from [31].	29
2.7	The scheme of regions in CCSN core. CC: charged-current, NC: neutral-current. Figure is taken from [44].	31
2.8	Neutrino luminosities and mean energies from simulations. Left figure is the 2D simulation of $M = 27M_{\odot}$ for the burst, accretion, and early explosion phase. The middle is for 3D simulation of $M = 18M_{\odot}$ until the explosion phase where there is somewhat equipartition for different flavors. The right is for $8.8M_{\odot}$ showing the Kelvin-Helmholtz cooling phase. Figure is taken from [44].	33

2.9	A plot of h_+ evolution from a simulated GWs from a rapidly rotating CCSN based on magnetorotational mechanism, at a distance of 10 kpc. Figure is taken from [17] based on [54].	39
2.10	A plot of h_+ evolution from a simulated GW signal from a CCSN due to convection and SASI as seen by an equatorial observer at 10 kpc. This figure is taken from [17] based on the work of [13].	41
2.11	A time-frequency map of a GW simulated signal analysis from [14] model with SFHx EoS from [60]. It is also plotted the different modes from this signal: A due to acoustic mechanism, B due to SASI, C (and C#) due to p -mode, and D due to the overtone of B-mode.	42
2.12	A gravitational waveforms h_{\times} (top) and the spectrogram (bottom) for the Stokes V parameter of SFHx EoS ([60]) taken from [56]. The black line in the spectrogram corresponds to g -mode. In the frequency of 100-200 Hz, there is a phase change in the Stokes V parameter (red to blue) which could explain the frequency difference of the D overtone mode (see text).	43
3.1	R_{mean} distribution generated by Monte Carlo for multiplicity, $m = 2, 3, 4$, and 8. Figure is taken from [64].	48
3.2	The distribution of $Sumdir$. Figure is taken from [64].	51
3.3	The <i>raw</i> detection probability as a function of distance for distant burst search and low energy threshold search. Figure is taken from [64].	51
3.4	The raw efficiency of the method with no oscillation 3.4a, normal hierarchy 3.4b, and inverted hierarchy 3.4c as well as the background rate per 10 seconds of SK detector 3.4d. Figure is taken from [65].	54
3.5	The neutrino energy events as a function of time captured by Kamiokande-II (closed circles) and IMB (open circles) produced by SN1987A. Figure is taken from [70].	56

3.6	The orbital decay of PSR1913+16. The data points are the observed change of the epoch of periastron, while the parabola illustrates the expected change due to the emission of GWs according to general relativity. Figure is taken from [73].	57
3.7	Nautilus gravitational wave bar detector. Figure is taken from [77].	58
3.8	Gravitational wave interferometer detectors around the world. .	59
3.9	The scheme of a gravitational wave interferometer. Figure is taken from [84].	59
3.10	$\psi_{ab}(x)$ for WFT (left) and WT (right). Figure is taken from [93]. .	61
3.11	WFT (left) and WT (right). Figure is taken from [94].	62
3.12	Noise spectral densities of the LIGO and Virgo detectors. O1 and O2 are the upgraded advanced LIGO and advanced Virgo detector sensitivities in their “observing runs” with several GW detections. Figure is taken from [95].	63
3.13	The detection efficiency curves as a function of distance for the numerical waveforms. Figure is taken from [53].	65
3.14	The detection efficiency curves as a function of distance for the extreme waveforms. Figure is taken from [53].	65
3.15	The FAP (false-alarm-probability) curve as a function of distance for the extreme waveforms. Figure is taken from [95]. . . .	66
3.16	The efficiency curve as a function of distance for different waveforms. Panel (a), (b), and (c) show the efficiency using 3 different families of waveforms for the position and time reference of SN 2017eaw with the 50% detection efficiency distances are in parentheses. Meanwhile, panel (d) is for the <i>ad-hoc</i> sine-Gaussian waveforms as a function of h_{rss} , instead, and with the 50% detection efficiency h_{rss} are in parentheses. Figure is taken from [95].	66

3.17	The details of GW150914: The top left is the H1 detector strain, the top right is the L1 and H1 detector strain together. The signal arrived first at L1 and $6.9_{-0.4}^{+0.5}$ ms later at H1. The second row is the numerical relativity waveform with the shades are the 90% credible regions of two independent waveform reconstructions. The third row is the residual. Bottom row is the time-frequency representation of the strain data. Figure is taken from [92].	68
4.1	The on-source (green) and the off-source (red) time segment. . .	74
4.2	The scheme of binomial test in this work. The superscript d stands for data, while s stands for simulation.	76
4.3	Cumulative events vs p_{local} . It consists of distribution of observed p -values (line-dots), the null hypothesis (dashed line) from 1 million simulations, and the $\sim 1\%$ CL (solid line) for which only $i = 5, \dots, 15$ are shown. This figure is taken from paper [108].	78
4.4	The reproduction of figure 4.3 with the null hypothesis (black-dashed line) from 1 million simulation, the $\sim 1\%$ CL exclusion region (blue line), and the estimation of the exclusion region (red line) & the null hypothesis (magenta line) of figure 4.3 taken by using [112].	79
4.5	Cartoon of full run configuration of Antares. There are 12 lines and each consists of photodetectors to detect Cherenkov light from muons due to high-energy astrophysical neutrinos. During January-September 2007, only 5 lines were running. This figure is taken from [114].	80
4.6	The on-source (blue) and the off-source (red) time segment. Figure is taken from [110].	81

4.7	The distribution of observed p -values (blue-line-dots) for LF with most significant excess (red dot), null hypothesis (dashed line), and 5σ exclusion region (solid line). This is taken from paper [109].	82
4.8	The reproduction of figure 4.7. This consists of null hypothesis (black-dashed line), 5σ exclusion region (blue line), and the data of figure 4.7 from [115]: observed p -values (black-line-circles), most significant excess (magenta dot), 5σ exclusion region (red line) & null hypothesis (magenta line).	83
4.9	The distribution of observed p -values (blue-line-dots) for HF with most significant excess (red dot), null hypothesis (dashed line), and 5σ exclusion region (black dot). This is taken from paper [109].	83
4.10	The reproduction of figure 4.9. This consists of null hypothesis (black-dashed line), 5σ exclusion region (blue dot), and the data of figure 4.9 from [115]: observed p -values (black-line-circles), most significant excess (magenta dot), 5σ exclusion region (red dot) & null hypothesis (magenta line).	84
5.1	The scheme for cyclic coincidence analysis. The blue and green color represents the time-series data sets. When the green data set is out of bound like in the second row in Panel (A) due to time-shifting, that part of the green data set is taken and put to the beginning of the blue data set (red chunk), thus the livetime of both data sets will be constant for each shift. This works also for the other time-shift direction like in Panel (B).	89
6.1	The time evolution of injections, following the double-exponential of equation 6.1, is show as blue area. Here, we use $\tau_1 = 10$ ms and $\tau_2 = 1$ s. It is also shown the expected (constant) time evolution of background as orange area.	100

6.2	The fluence Φ_i^0 as a function of neutrino energy E . Blue, red, and green curve are respectively for $\bar{\nu}_e$, ν_e , and ν_x , where x stands for all other flavors of neutrinos and anti-neutrinos. The peak energy is also written above each curve.	101
6.3	The P_H as a function of neutrino energy. Figure is taken from [123].	104
6.4	The number of events in Super-K for normal and inverted hierarchy, with $\theta_{13} \simeq 8.5^\circ$ (see text for the explanation).	105
6.5	A cartoon of a time-series data consisting of injection in 10 kpc (high-statistic signal) seen by LVD.	107
6.6	A cartoon of a time-series data consisting of injection in 65 kpc (low-statistic signal) seen by LVD.	107
6.7	Panel (a): PDF for background (+ injections of several distances) clusters as a function of ξ parameter in the case of Super-K detector. Panel (b): the optimal cut value for the ξ parameter, $\bar{\xi}(D)$, as a function of the source distance D for Super-K detector. Figure is taken from [119].	109
6.8	Panel (a): The efficiency η (red) and the misidentification probability ζ (blue) for Super-K modelled-detector data. Panel (b): The gain factor G in Super-K modelled-detector data. Figure is taken from [119].	111
6.9	Several possible cuts for a network of detectors. The green area is where the coincidences pass the single-cut, the red area is for the product-cut, while the blue area is for the diagonal-cut. See text for the explanation.	114
6.10	Panel (a): The efficiency η^* (red) and the misidentification probability ζ^* (blue) for LVD-KamLAND modelled-detector data where the ξ -cut is represented in the solid line and the standard is in the dashed line. Panel (b): The gain factor G in LVD-KamLAND modelled-detector data. Figure is taken from [119].	115

7.1	PDF histogram of simulated KamLAND data. The histogram has been fitted with several possible distributions such as 4-parameter Gamma distribution (like in chapter 6 and reference [119]), generalized extreme value distribution [132], as well as Burr distribution [133]. It has been also shown the residuals. . .	125
7.2	PDF histogram of simulated KamLAND data with the interpolation and its residual of the histogram. The histogram is the same as in figure 7.1, on the other hand here we use the interpolation method, unlike figure 7.1, which is by fitting. The area under curve is basically: $\int_{\xi=\xi_{\min}}^{\infty} PDF(\xi \geq \xi_{\min} k) d\xi = 1$. In the tail of the interpolation for high ξ , there is some “wobble” that is due to the lower number of counts in the histogram bin, which is related with Poisson uncertainty.	126
7.3	The expected multiplicity as a function of distance for the involved detectors. Here, we can see that Super-K could detect $\lesssim 2$ low-energy neutrino events from a CCSN in Andromeda, while KamLAND and LVD can gather about 8 events from a CCSN happening in Small Magellanic Cloud. Moreover, all detectors are able to see CCSNe in the Milky Way.	128
7.4	KamLAND ξ -multiplicity map. The green-shaded area passes 1/100-year threshold for standard f^{im} , while the red-shaded area is the improvement by using 2-parameter method (this work). The total (red + green) area passes the threshold with the 2-parameter F^{im}	130
7.5	KamLAND ξ -multiplicity map, the same as figure 7.4 with the addition of 10-year simulated background.	131
7.6	KamLAND ξ -multiplicity map, the same as figure 7.5 with the addition of 65-kpc injections. This figure is presented in [129]. .	132
7.7	Super-K ξ -multiplicity map with the 250-kpc injections.	133
7.8	Super-K ξ -multiplicity map with the 65-kpc injections.	134
7.9	Super-K ξ -multiplicity map with the 700-kpc injections.	135

7.10	3D histogram of the ξ distribution of the accidental coincidences between the simulated-10-year KamLAND and LVD data. . . .	136
7.11	Same as figure 7.10 but with the observed injections in 65kpc. . .	137
7.12	Hyper-K ξ -multiplicity map with 10-year simulated background and 700-kpc injections.	139
8.1	Scheme of the method for the joint GW-neutrino analysis to search for CCSNe. We use the c_{WB} pipeline with its default/standard configuration. Meanwhile, we use 2-parameter method for each neutrino detector data analysis (chapter 7). We combine the neutrino data with the coincidence analysis with product method (chapter 5). We combine the list of GWs and neutrinos together in terms of multimessenger via product-method coincidence analysis (chapter 5). The final result will be 3 lists: 1 list of joint GW-neutrino signal signals, 1 list of GW signals from c_{WB} , and 1 list of joint neutrino network signals.	144
8.2	The efficiency curve from c_{WB} of several injection models: Gaussian, sine-Gaussian, and white-noise-burst.	145
B.1	The scheme of the deformation of test masses (dots) passed by gravitational waves based on equation B.7 (taken from [24]). . .	156

List of Tables

2.1	Supernova rates per galaxy type per century per $10^{10} \mathcal{L}_{B,\odot}$, with $h_0 = H_0/(100 \text{ km s}^{-1} \text{ Mpc}^{-1})$, taken from [20].	24
2.2	GW emission processes in CCSNe and the possible emission strength for different possible mechanisms. For a galactic SN, “strong” means a high probability of detection by initial and advanced LIGO, “weak” is referred to marginal probability to be detected by advanced LIGO, and “none” means probability of non detection by advanced LIGO. These three explosion mechanisms likely produce exclusive GW signatures and the detection or non-detection of a GW signal may give a hint of the mechanism. MHD stands for Magnetohydrodynamics and PNS is the abbreviation of proto neutron star. Table is taken from [52].	43
3.1	Summary of different neutrino detectors (taken from [61, 62]).	45
3.2	Specific SN neutrino detectors and some proposed projects (taken from [61, 62]).	46
6.1	The model comparison used in [127] versus our work. *estimated from figure 1.4.	103
6.2	Expected number of events in Super-K from a CCSN at 10 kpc. Here, we compare our simple result with the result of [127] with different models such as Wilson [11] as well as NK1 and NK2 [128] and $E_{\text{thr}} = 7 \text{ MeV}$	104
6.3	The details of involved detectors	110

7.1	Simulation details of some detector models. Here, there are two types: liquid scintillator and water Cherenkov. The main detection channels is the $\bar{\nu}_e$ from IBD. It is also provided the mass, background frequency f_{bkg} , as well as energy threshold E_{thr}	127
7.2	Single detector KamLAND analysis with 65-kpc injections. The data set is 10-year long. See text for the explanation.	132
7.3	Single detector Super-K analysis with 250-kpc injections. The data set is 10-year long. See text for the explanation.	133
7.4	Efficiency η and misidentification probability ζ for KamLAND-LVD 10 year - 65 kpc.	138
7.5	One-module Hyper-K with 700-kpc injections.	138
8.1	Details of GW- ν coincidences for 8 kpc. Column 2-5 are for KamLAND multiplicity, KamLand ξ [Hz], LVD multiplicity, and LVD ξ [Hz]. Column 6 and 7 are for the joint f^{im} [Hz] and the joint F^{im} [Hz] between KamLAND and LVD. Column 8, 9, and 10 are for the FAR [Hz] of GW candidates, the jointFAP of KamLAND-LVD-GW coincidences with the standard f^{im} , and the jointFAP of triple coincidences with the new F^{im}	146
8.2	Details of GW- ν coincidences for 16 kpc. The legends are the same as in table 8.1.	147
8.3	Details of GW- ν coincidences for 32 kpc. The legends are the same as in table 8.1.	147
8.4	Details of GW- ν coincidences for 64 kpc. The legends are the same as in table 8.1.	147
8.5	Details of GW- ν coincidences for 128 kpc. The legends are the same as in table 8.1.	147

8.6 Details of background coincidences for 2ν network analysis. Column 2-5 are for KamLAND multiplicity, KamLand ξ [Hz], LVD multiplicity, and LVD ξ [Hz]. Column 6 and 7 are for the joint f^{im} [Hz] and the joint F^{im} [Hz] between KamLAND and LVD. Column 8 and 9 are for their FAPs with the f^{im} and F^{im} . . 149

For/Dedicated to My Universe

Introduction

A core-collapse supernova (CCSN) is the final phase of a massive star, whose mass is $M \gtrsim 8M_{\odot}$, that ends up its life with a huge explosion lasting a fraction of a second and releasing an impressive energy of several 10^{53} ergs. The electromagnetic emission from this type of supernovae has been the first studied from human being since the old, first by eyes then with telescopes. In 1987 a new way to observe this event became a reality: the observation of the low-energy neutrino (LEN) emission during the explosion of a massive star ($M \approx 20M_{\odot}$) in the Large Magellanic Cloud. The event, called SN1987A, with a bunch of few neutrinos detected (~ 20 events), not only ratified the beginning of the neutrino astronomy but also allowed scientists to test and improve the actual knowledge about this phenomenon. Moreover, in 2015 the two LIGO detectors simultaneously observed a transient gravitational wave (GW) signal, named GW150914, associated with the merger of two black holes. This event opened up the era of the GW astronomy and the possibility to combine information provided by three different probes, namely photons, neutrinos and GWs, becomes within reach.

CCSNe are expected to emit all these messengers and their observations could be the only way to really understand the physical mechanism triggering the final explosion of the progenitor stars. Indeed, as it will be discussed in the beginning of this thesis, despite the big effort spent on developing very complex numerical simulations, this mechanism is still uncertain. The different processes that could generate the GW emission during the explosion of a massive star seems to be one-to-one connected with the explosion mechanisms at work inside the star structure. For this reason the detection of the GW signal from a CCSN deserves a special effort.

LENs (with the average energy of around 10 MeV) will carry away the $\sim 99\%$ of the total energy emitted from a CCSN in a time scale of tens of seconds. These neutrinos, thanks to their weak cross section, can escape from the innermost region of the stellar structure during the core-collapse explosion and the starting time of the neutrino luminosity can be used to trigger for the GW search within a small temporal window ($\lesssim 1$ second). The correlated observation of both LENs and GWs can reduce the *false-alarm-rate* of some order of magnitude.

With the goal to exploit and develop this basic idea, a global inter-collaboration activity is born to implement a combined search of CCSNe with a network of neutrino and GW detectors. In 2015 a memorandum of understanding has been signed among LIGO, Virgo, LVD, Borexino, IceCube and KamLAND collaborations to have a complete data sharing and to look for correlated signals.

This PhD thesis is born within this inter-collaboration working group, that we call “GW ν ”, with the aim to implement and improve the method and the detection efficiency of the CCSN search. In particular, while the GW detectors work as a network since the beginning of their science runs, the neutrino detectors usually work independently, without sharing and combining their data. For this reason we will discuss deeper in organizing the sub-network of neutrino detectors in an efficient and correct way. Then, we will concentrate on the possibility to improve the detection potential of the neutrino sub-network by exploiting the temporal behaviour of a neutrino burst from a CCSN. This will allow us to better disentangle low-statistics signals coming from weak or far supernovae from noise. We will also discuss a better strategy to combine the information provided by LENs and GWs. Particularly, we will show that the outlined procedure allows us to achieve a lower false-alarm-rate of a combined observation of GW and neutrino burst, which means the increase of significance values of astrophysical signals.

In order to pursue these goals, we will introduce the astrophysical context in chapter 1 in order to summarize our knowledge of the different phases in

a CCSN event and outlining the different hypotheses for the unknown explosion mechanism. Chapter 2 will be devoted to the discussion of the expectations for the two different probes we are interested in, particularly the different phases for the LEN emission and the several emission processes that can give rise to the emission of impulsive burst of GWs. In chapter 3 we will face the detection strategy and problems for both kinds of detectors: neutrino detectors looking for a bunch of few neutrino interactions between the background, and GW interferometers trying to identify an un-modelled burst lasting few tens of milliseconds among several identical spikes due to the noise.

In chapter 4 we will start to discuss the multimessenger search performed within the GW ν working group and we will also describe the methods used in different astrophysical contexts to perform multimessenger search/analysis. In chapter 5 we will focus on the method to look for temporal coincidences in the global network of detectors. Here, we will face a serious problem on how to estimate the statistical significance of a temporal coincidence between a cluster of neutrino events and a burst of GWs in which both of them are sub-threshold signals for the respective detectors.

In order to solve this problem we will discuss in chapter 6 the possibility to exploit the temporal behaviour expected for a neutrino burst from a CCSN in order to disentangle real astrophysical signals from noise fluctuations. This method will be refined in chapter 7 in terms of providing a new *false-alarm-rate* for each neutrino cluster, enabling us to increase the statistical significance of real astrophysical signals while keeping the significance of noise unchanged. Finally, these results can be applied to a global network of neutrino and GW detectors to provide a robust statistical assessment for a multimessenger CCSN search.

Chapter 1

Core-Collapse Supernovae

Massive stars ($M \gtrsim 8M_{\odot}$) end up their stellar evolution in a final phase characterized by the gravitational collapse of their inner core, this phase may terminate with the final explosion of the structure giving rise to CCSNe. The challenge in understanding the CCSNe lies on the fact that we need to reverse an implosion (collapsing inward) to an explosion (ejecting outward) powered by the transfer of energy from the core (proto neutron star) to the envelope. Not all core-collapsing stars could explode as supernovae, indeed. In fact, some may not have explosions, known as failed supernovae. However, we will focus on core-collapse processes that give rise to explosions as a supernovae. In this chapter, we will discuss more on the astrophysical processes of these CCSNe.

After a CCSN happens, a remnant either being a neutron star (NS) or a black hole could form. The total energy budget of a core-collapsing star is indeed the conversion from a progenitor massive star to this remnant. In other words, the energy is simply the difference of the gravitational binding energy of the progenitor and of the remnant. Almost all of this energy is carried away in the form of neutrinos. This is observed for (the only) example of the neutrino observation¹ from core-collapse SN1987A (see chapter 3.1). To give some idea, here we will estimate this total energy of a CCSN with the remnant being a neutron star. Let us assume G , R_{\odot} , and M_{\odot} as our gravitational constant, solar radius, and solar mass². The energy difference of a spherical body of a

¹The only neutrino detection from a CCSN till now.

² $G = 6.67 \times 10^{-8} \text{ cm}^3 \cdot \text{g}^{-1} \cdot \text{s}^{-2}$, $R_{\odot} = 6.96 \times 10^{10} \text{ cm}$, and $M_{\odot} = 2 \times 10^{33} \text{ g}$.

Chapter 1. Core-Collapse Supernovae

star of $8M_{\odot}$ and $200R_{\odot}$ collapsing to a NS of $1.4M_{\odot}$ and $R_{\text{NS}} = 15 \text{ km}$ can be written as,

$$\begin{aligned}\Delta E_{\text{grav}} &= E_{\text{NS}} - E_{*} \\ &= \frac{3}{5} \frac{GM_{\text{NS}}^2}{R_{\text{NS}}} - \frac{3}{5} \frac{GM_{*}^2}{R_{*}} \ll E_{\text{NS}} \\ &\approx \frac{3}{5} \frac{GM_{\text{NS}}^2}{R_{\text{NS}}} \\ &\approx \frac{3}{5} \frac{G(1.4M_{\odot})^2}{15\text{km}} \\ &\approx 2 \times 10^{53} \text{ erg} \equiv \varepsilon_b,\end{aligned}\tag{1.1}$$

which is the rough total energy estimation of a CCSN. This binding energy difference will be carried away from a CCSN in some forms:

- * around $99\% \cdot \varepsilon_b$ is in the form of neutrinos,
- * about $1\% \cdot \varepsilon_b$ is in kinetic energy of gas in a form of shock waves,
- * approximately $0.01\% \cdot \varepsilon_b$ is in electromagnetic waves (photons),
- * and $\lesssim 0.0001\% \cdot \varepsilon_b$ is in gravitational waves.

Furthermore, there are actually several types of possible progenitors for these collapsing objects with different masses, magnetic field and rotation. Later on, we will discuss the several possible progenitor stars that can undergo the core-collapse in section 1.1 (based mostly on [1]). More importantly, we will also discuss several phases (in section 1.2, referred mostly to [2]) happening in the core-collapse to drive the explosion. In section 1.3 we will also discuss the shock revival mechanisms that are important to successfully produce an explosion in CCSN simulations.

1.1 Stellar Core-Collapse Progenitors

A stellar lifetime, starting from burning H in the core to ending up as a white dwarf, neutron star, or blackhole, can be estimated mainly by how long

Chapter 1. Core-Collapse Supernovae

is the period of the star in the main sequence (H burning³ in the core) of the Hertzsprung-Russell diagram. It depends on its mass M_* and luminosity L_* (of the main sequence) and can be approximated⁴ as $t_{\text{evol}} \approx 7.3 \times 10^9$ [years] $(M_*/M_\odot)/(L_*/L_\odot) \approx 7.3 \times 10^9$ [years] $(M_*/M_\odot)^{-2.5}$. Thus, more massive stars are quicker to exhaust their fuel during the stellar evolution than the less massive ones.

After finishing H core burning and leaving the main sequence, massive stars ($M_* \gtrsim 8M_\odot$) will contract due to gravitation, then, their temperature and pressure will increase which could ignite other burning phases. The late phases of stellar evolution of these massive stars undergo faster than the early main sequence phase due to the lower efficiency of energy production in higher stages of nuclear burning in the later phases. More massive stars can burn heavier elements in the core during their late phases. For less massive stars, they will end up in their last evolution phase of being He (or C/O) white dwarfs stabilised by lepton degeneracy pressure and cooling at a generally fixed density. These less massive star evolution can be seen in figure 1.1 from the line of $M_* \lesssim 0.08M_\odot$ up to the line of $7M_\odot \lesssim M_* \lesssim 8M_\odot$ with the end paths of those lines being almost vertical, meaning that each ending path has a constant ρ_c but a gradually decreasing T_c .

Stars having initially higher masses during the zero age main sequence will be able to reach the “death zones” where the stellar cores become gravitationally unstable and undergo a runaway process. Contraction, and in a runaway process, collapse, happens when the effective adiabatic index drops below the critical value of $4/3$ (appendix A) and the star structure will be mechanically unstable. There are four different types of runaway processes, based on mass range, for this collapsing (implosion) phase and will be discussed in the following.

The first type of the runaway processes is the electron-capture supernova,

³The hydrogen burning is the longest period in the stellar evolution. See more details for example in reference [3].

⁴Solar luminosity $L_\odot = 3.85 \times 10^{33}$ erg s⁻¹.

Chapter 1. Core-Collapse Supernovae

which holds for the lowest-mass ($8M_{\odot} \lesssim M_* \lesssim 9M_{\odot}$ line in figure 1.1) progenitor of CCSNe, having O-Ne-Mg core during their evolution and cannot do higher stages of nuclear burning. This is due to the fact that in these progenitors, the electron degeneracy (which overcomes the contraction) in their core is achieved before reaching the condition necessary for Ne burning ignition. Then, the increase of electron Fermi energy enables electron captures in the core triggering the gravitational core-collapse. This type contributes to about 20-30% of all SNe. The electron-capture supernovae eject little C & O and very little Ni due to their steep density decline in a thin C-O shell ($\sim 0.1M_{\odot}$ between $3 \times 10^4 \text{ g cm}^{-3}$ and $4 \times 10^8 \text{ g cm}^{-3}$) at the edge of O-Ne core, and therefore being relatively faint SNe. One of the most famous possible examples is the Crab SN1054. Other SNe may also be on this type such as SN1997D, 1999br, 2005cs, and 2008s.

The second type is called the iron-core supernova coming from a progenitor that can burn Ne in the core to form Fe. The iron in the core becomes gravitationally unstable when the core undergoes the dissociation of Fe nuclei to α particles and free nucleons (figure 1.1 for the $9M_{\odot} \lesssim M_* \lesssim 100M_{\odot}$ line). This dissociation process happens when the core temperature reaches $\sim 10^{10}\text{K}$ ($k_{\text{B}}T \sim 1\text{MeV}$). The stellar cores of pre-SN stars are expected to rotate slowly, therefore the stellar rotation does not play a crucial role for this iron-core supernova type. This slow rotation is of the order of tens of seconds, due to the angular momentum loss during the evolution phases of the progenitors (in particular the red giant stage in which mass-loss plays a significant role). The mass-loss in that phase is caused by the magnetic torques from differential core-envelope rotation.

Unlike the case for the iron-core supernova in which stellar rotation does not play a significant role, another type of supernovae called the gamma-ray burst supernova, as well as hypernova⁵, are thought to be highly affected by

⁵Hypernovae are stellar explosions with unusually high ejecta velocities (broad spectral lines). They are associated with long-duration gamma-ray bursts (GRBs) with the time span $t_{\text{GRB}} \geq 2 \text{ s}$, observed spectroscopically or as late light-curve humps during the afterglow. Examples: SN1998bw with GRB980425, SN2003dh with GRB 030329, etc.

Chapter 1. Core-Collapse Supernovae

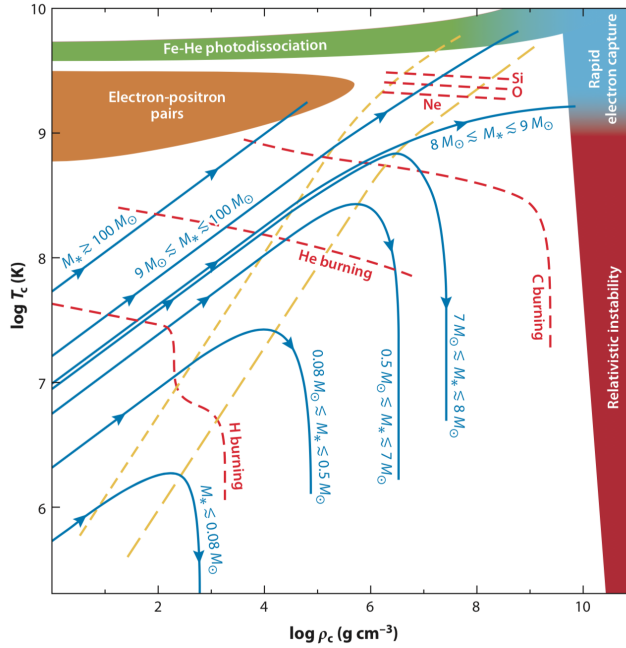


FIGURE 1.1: Schematic stellar evolution tracks for different initial stellar masses M_* (taken from [1]).

the rapid stellar rotation. Here, we will discuss in a general way and for more details see e.g. reference [4]. Gamma-ray bursts (GRBs) are understood to be ultrarelativistic jets interpreted as a signature of a blackhole-forming stellar collapse. Alternatively, they are powered by a nearly critically rotating neutron star with $t_{\text{rot}} \sim 1$ ms and an ultrastrong magnetic field $\langle B \rangle \gtrsim 10^{15}$ G, called millisecond magnetar. The jet and explosion could be powered by rotational energy of the magnetar itself or by gravitational and rotational energy of accretion flow. Besides, they could be also due to a blackhole through magnetohydrodynamic effects as well as through neutrinos radiated from the heated matter because of a magnetic dissipation. The progenitors of the GRBs and hypernovae are believed to have cores already evolving to be blackholes before their explosions. Thus, they must be compact stars without an extended H envelope to allow ultrarelativistic jets. This means, Wolf-Rayet stars are favourable as the progenitors, but with high birth spin and evolution paths avoiding mass & angular momentum loss, else, in binaries. In today's universe, there are only ~ 1 GRB in 1000 SNe [1], but in the early (low metallicity, 1/10 of the solar) universe, GRBs and hypernovae could be very common.

This fact is supported by the GRB observations which are preferentially in low-metallicity regions.

The last type that we will discuss is called pair-instability supernovae. They occur for progenitors whose mass $M_* \gtrsim 100M_\odot$ (see figure 1.1 for the plot). This means that the stars are very hot and encounter pair instability, occurring after the central C burning at $T \sim 10^9$ K. The e^+e^- pair formation, reducing adiabatic index of the *equation-of-state* (EoS) to be below 4/3 (appendix A), gives rise to the gravitational instability. The stars whose masses $100M_\odot \lesssim M_* \lesssim 140M_\odot$ and $M_* \gtrsim 260M_\odot$ will collapse to a BH, while for the intermediate mass range ($140M_\odot \lesssim M_* \lesssim 260M_\odot$), the complete disruption of the stars will happen due to the ignition of the still-available thermonuclear fuel. The explosion energy can be more than 10^{53} erg and with the production of ^{56}Ni of about $\gtrsim 50M_\odot$. For the BH formation case, particularly with the presence of rotation resulting accretion torus, a huge amount of energy is released in neutrinos ($\sim 10^{55}$ erg) [1]. There are some possible examples of this pair-instability supernovae, such as SN2002ic, SN 2005gj, etc. Moreover, the rate of this type is of about 1 in 100-1000 CCSNe and this type is expected to be in metal-poor host galaxies. In the Milky Way, it is estimated there are around two dozens of progenitor stars (for example η Carinae) may finish their evolution to be this kind of supernovae [1].

1.2 Standard Picture of Core-Collapse Supernovae

Almost all of the total energy ε_b of the core-collapses will be carried away by neutrinos in CCSNe. But, what is the main mechanism driving these core-collapses and which processes play a role during the explosion? How does this core-collapse energy carried away by neutrinos work? In the following, we will discuss the neutrino-heating mechanism, also known as Bethe-Wilson delayed scenario [5, 6], which is based on c.f. chapter 1 in [2]. This purely delayed scenario cannot produce an explosion in many simulations [1]. However, this scenario is the basic understanding in the core-collapse itself, and

Chapter 1. Core-Collapse Supernovae

together with some additional mechanisms (section 1.3) after the collapse (implosion) can successfully drive the ejection of the envelope of the stars (explosion).

The Astrophysical Phases of Core-collapse Supernovae

As stated before, stars having a stellar mass $M_* \gtrsim 8M_\odot$ will experience core-collapse as their final evolution phase. In the beginning of their life (starting from the zero-age main sequence, explained in detail in reference [3]), they will burn lighter elements in the core (and then move to the envelope) to heavier ones by fusion processes to produce energy counterbalancing the gravity. When one type of light element⁶ is exhausted, the core contracts causing the temperature to increase. Then, the next stage burning happens, which is the burning of a heavier element producing even a heavier one. This process first happens in the convective core and when the fuel is exhausted, the burning moves to the outer layer where there is still available fuel. In the end, the star will have an onion-like model in which the innermost consists of ^{56}Fe (see figure 1.2).

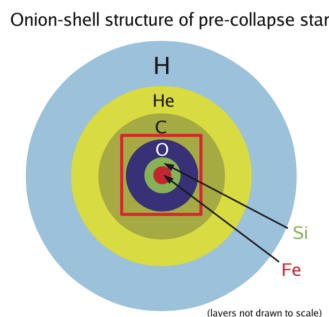


FIGURE 1.2: Onion-like structure of a star during pre-collapse. Only the main elemental constituents in the different shells (containing the products and ashes of the nuclear fusion stages) are indicated. Figure is taken from [7].

Each stage of fusion processes produces some energy necessary to hold the stellar structure not to collapse due to gravity. However, when the core consists of ^{56}Fe , the stars cannot produce energy anymore by burning iron.

⁶It starts from burning H to produce He, then as a next step is burning He to produce C/O, then, C/O burning to produce Si, and Si burning to produce Fe.

Chapter 1. Core-Collapse Supernovae

To do the iron fusion, instead of producing energy, it needs energy from the surrounding to happen. Thus, the iron fusion do not occur. This can be understood by looking at the graph of nuclear binding energy as a function of number of nucleons (A) in figure 1.3. The binding energy increases steeply (starting from H) and peaks at $A = 56$ which is the value for ^{56}Fe . Then, the binding energy decreases steadily. This means ^{56}Fe is the tightest nuclear species and its fusion is endothermic (by absorbing energy from the structure). This is the end of energy production processes by fusions in the stars. Moreover, the stars may not collapse directly since there is another way of counterbalancing the gravity: degenerate electrons produce a pressure to overcome gravity.

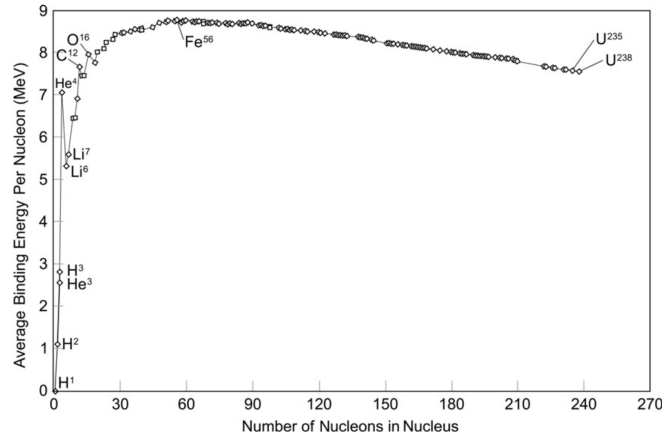


FIGURE 1.3: Nuclear binding energy as a function of number of nucleons in the nucleus. Figure is taken from [8].

In the center of the stars, the temperature $T_c \approx 10^9$ ($k_B T_c \approx 1.7m_e c^2$) changes electrons to be relativistic and the density $\rho_c \approx 10^9 \text{ gr/cm}^3$ causes the electrons to be degenerate. Let's define the degeneracy parameter ψ and the chemical potential χ_e in which $\psi \equiv \chi_e/(k_B T)$. As we know, the electron distribution follows Fermi-Dirac statistics,

$$f(p)dV dp = \left[\frac{8\pi p^2}{h^3} dp dV \right] \left[\frac{1}{1 + \exp \{E/(k_B T) - \psi\}} \right], \quad (1.2)$$

where p , V and h stand for momentum, volume, and the Planck constant. The form inside left parentheses after the equal sign of equation 1.2 can be understood as the occupation number, while the object inside the right parentheses

Chapter 1. Core-Collapse Supernovae

is the “filling factor” (a fraction of occupied cells, ≤ 1). The complete degeneracy happens when all phase cells up to Fermi momentum $p_F = \left(\frac{3h^3 n_e}{8\pi}\right)^{1/3}$ are occupied (with n_e stands for the number density of electron). This complete degeneracy can happen when $T \rightarrow 0$.

In our case for stellar core-collapse, we face the partial degeneracy regime with extreme relativistic electrons (momentum $p \approx E/c$ and velocity $v(p) \approx c$). The number density of electrons becomes,

$$n_e = \frac{8\pi}{h^3} \int_0^\infty p^2 \frac{dp}{1 + \exp(E/(k_B T) - \psi)} \approx 8\pi \left(\frac{k_B T}{hc}\right)^3 F_2(\psi), \quad (1.3)$$

where $F_2(\psi)$ is the Fermi-Dirac integral under the form of $F_z(\psi) = \int_0^\infty du \frac{u^z}{1 + \exp(u - \psi)}$, in which the values can be seen in some Fermi-Dirac integral table [3]. Meanwhile, the pressure from this Fermi-Dirac distribution can be written as,

$$\begin{aligned} P_e &= \frac{8\pi}{h^3} \int_0^\infty p^3 v(p) \frac{dp}{1 + \exp(E/(k_B T) - \psi)} \approx \frac{8\pi}{3h^3 c^3} (k_B T)^4 F_3(\psi) \\ &= \frac{hc}{3(8\pi)^{1/3}} \frac{F_3(\psi)}{F_2(\psi)} n_e^{4/3} \\ &= \frac{hc}{3(8\pi)^{1/3}} \frac{F_3(\psi)}{F_2(\psi)} \left(\frac{Y_e \rho}{m_u}\right)^{4/3}, \end{aligned} \quad (1.4)$$

in which $Y_e = N_e/N_n = \frac{\rho_e m_u}{\rho m_e}$ is the fraction of electron per nucleon for total density (ρ), atomic mass unit (m_u), electron mass (m_e), and electron density (ρ_e). The electron chemical potential is thus,

$$\chi_e = E_F = hc \left(\frac{3}{8\pi}\right)^{1/3} n_e^{1/3} \sim 11 \text{ MeV} \left(\frac{\rho_c Y_e}{10^{10} \text{ gr/cm}^3}\right)^{1/3}, \quad (1.5)$$

and for the complete degeneracy regime, $T \rightarrow 0$ and $\psi \rightarrow \infty$,

$$P_e = \left(\frac{3}{\pi}\right)^{1/3} \frac{hc}{8} \left(\frac{Y_e \rho}{m_u}\right)^{4/3}. \quad (1.6)$$

The pressure in equation 1.6 can balance the gravity (hydrostatic equilibrium) only until the maximum central iron mass equals the Chandrasekhar mass limit (appendix A).

Chapter 1. Core-Collapse Supernovae

The solution for density and pressure from equation A.7 in Appendix A will be $\rho(r) = \rho_c w^n$ and $P(r) = P_c w^{n+1}$. Thus, the mass can be calculated as,

$$\begin{aligned} m(r) &= \int_0^r 4\pi r^2 \rho(r) dr = \int_0^r 4\pi r^2 \rho_c w^n dr = \frac{4\pi \rho_c}{A^3} \int_0^z z^2 w^n dz, \\ \Rightarrow M &= \frac{4\pi \rho_c R^3}{z^3} \int_0^z \frac{d}{dz} \left(z^2 \frac{dw}{dz} \right) dz = 4\pi \rho_c R^3 \frac{1}{z} \frac{dw}{dz} \Bigg|_{z=z_n}, \end{aligned} \quad (1.7)$$

where the value depends on n and can be seen from the Fermi-Dirac table. For our case, we can choose $n = 3$ (or $\gamma = 4/3$) in which the pressure mainly comes from electron degeneracy pressure and the electrons are in the relativistic regime. So, the total mass (equation 1.7) as Chandrasekhar mass limit becomes,

$$M_{\text{Ch}} \equiv M = 5.836 Y_e^2 F M_{\odot}, \quad (1.8)$$

where,

$$F = \left[1 + \left(\frac{s_e k_B}{\pi Y_e} \right)^2 \right], \quad (1.9)$$

in which $s_e = (Y_e \pi^2 T)/E_F$ is the electron entropy per nucleon for high degeneracy, by looking at equation 1.5, $F \rightarrow 1$ since $\left[\frac{s_e k_B}{\pi Y_e} \right] = \left[\frac{Y_e \pi^2 T k_B}{E_F \pi Y_e} \right] = \left[\frac{\pi}{\Psi} \right] \rightarrow 0$.

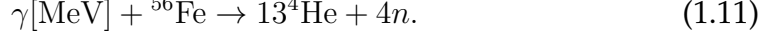
When the central mass grows bigger than the Chandrasekhar mass limit M_{Ch} , the pressure cannot hold the gravity and the star starts collapsing. What drives the collapse? Let's have a look at equation 1.4 in high degeneracy ($\Psi \gg 1$), and expanding equation 1.6 for the first order in its Fermi integral,

$$P_e = \left(\frac{3}{\pi} \right)^{1/3} \frac{hc}{8} \left(\frac{Y_e \rho}{m_u} \right)^{4/3} \left\{ 1 + \frac{2}{3} \left[\frac{s_e k_B}{\pi Y_e} \right]^2 \right\}, \quad (1.10)$$

and when $\Psi \rightarrow 0$ equation 1.10 becomes equation 1.6.

Infall and ν Trapping

Stars whose core mass $\gtrsim 1.4M_\odot$ (progenitors $\gtrsim 13 \pm 3M_\odot$) have instability mainly due to photodissociation,



It is an endothermic reaction and absorbs energy ~ 124.4 MeV [9] from electrons losing entropy with loss of thermal pressure (equation 1.10). The entropy of electrons is transferred to nucleons (keeping the conservation of total entropy during the contraction and the collapse). In the early stage of collapse, central density increases and electron capture is favorable,



From that reaction, Y_e will decrease and so does P_e (equation 1.10), and thus the collapse accelerates. This situation happens when $R_{\text{Fe}} \sim 3000$ km and $M_{\text{Fe}} \sim M_{\text{Ch}}$. In this case, ν_e 's escape freely due to the low density. The time scale of the collapse is the free-fall time,

$$\tau_{ff} = \left[\frac{3\pi}{32G\rho_c} \right]^{1/2} \approx 0.01 \text{ sec}. \quad (1.13)$$

That result in equation 1.13 is an approximation. Anyway, complete hydrodynamical calculations find that the collapsing time-scale should be of the order of $\tau_{coll} \approx 0.1$ sec.

The contraction and collapse of the stars happens when its core mass $M_c > M_{\text{Ch}}$. This collapse happens in a homologous manner, meaning that the velocity profile — found by Goldreich & Weber 1980 [10] — is proportional to the radial position $v(r) \propto r$. It has also been observed that the core mass collapsing in this way satisfies $M_{\text{Ch}} \leq M_{\text{hc}} \leq 1.0499M_{\text{Ch}}$. Noted that M_{Ch} depends on Y_e (equation 1.8) and the electron fraction decreases during the collapse (due to the electron capture in relation 1.12). If the initial condition of

Chapter 1. Core-Collapse Supernovae

Chandrasekhar mass and electron fraction are $M_{\text{Ch}0}$ and Y_{e0} respectively, the homologous core mass M_{hc} will be,

$$M_{\text{hc}} = 1.0499 M_{\text{Ch}} = 1.0499 \left(\frac{Y_e}{Y_{e0}} \right)^2 M_{\text{Ch}0}. \quad (1.14)$$

The central region of the star collapses homologously, while the outer (Fe) region collapses following the free-fall velocity. If the electron capture works forever, based on equation 1.14, the homologous core will be extremely small and prohibits the final explosion of the structure. Luckily, this is not the case since there is neutrino trapping. When the core becomes very dense, neutrinos cannot escape freely anymore (ν trapping) due to ν (neutral-current) scattering,

$$\nu_e + (Z, A) \rightarrow \nu_e + (Z, A), \quad (1.15)$$

with its mean free path,

$$\lambda_{\nu_e} \sim (\sigma_A^{\text{coh}} \cdot n_A)^{-1}, \quad (1.16)$$

where σ_A^{coh} is the cross section in nucleus rest frame, $n_A \equiv \rho Y_A / m_u$ is the number density of A element ($Y_A \approx 1/A$ fraction of nuclei in core), ρ is the core density, and m_u is mass unit. When $R_{\text{core}} \approx \lambda_{\nu_e}$, neutrinos are trapped and this happens when the core density $\rho_c \approx 10^{12} \text{ g/cm}^3$. The neutrino trapping stops the neutronization since ν 's are degenerate with high Fermi energy. In conclusion, there are two parts of the core:

- *Inner core*: $M_{\text{hc}} \sim 0.5 - 0.8 M_{\odot}$, homologous collapse, subsonic velocity.
- *Outer core*: supersonic speed with free-fall velocity $v_r \sim -\alpha \sqrt{2GM_r/r}$, for $\alpha \approx 1/2$ and M_r as mass enclosing r from the center.

In the infalling phase (beginning of the collapse, before ν -trapping), ν_e 's are emitted freely and this emission is called early neutronization ν burst (following relation 1.12). In this phase, it is difficult to determine ν_e spectrum since the spectrum is the superposition of different ν spectra from a nuclear species. We need to know the abundances of the nuclear species and the free

proton fraction. This phase happens for about 10 – 100 ms with very low ν luminosity making it difficult to observe. The energy of this infalling phase is of the order of 10^{51} erg, accounting for 1% of the total energy of a CCSN.

Bounce and ν Burst

The core-collapse continues until the central density $\rho \approx 10^{14}$ g/cm³. The nuclear (degeneracy) pressure slows down the collapse and even stops it⁷. Then, the outer region of the collapsing core bounces on the inner core and produces a shock wave. This bounce happens when the polytropic index n (appendix A) increases at the center and the collapse rate slows down.

During this bounce, an acoustic wave is generated. The amplitude of this acoustic wave is gradually increasing following the continuous increase of the density. Moreover, this wave is propagating outward until the so-called “sonic point” where it cannot propagate further. The sonic point is basically where the sound velocity is the same as the homologous matter velocity. The wave is accumulated in this point, in terms of momentum in the outward direction, and this accumulation leads to produce a discontinuity in velocity, pressure, and density, defining the *shock wave*. The strength of the shock wave depends on the maximum value of central density, ρ_c . Moreover, this ρ_c depends on the EoS (see equation A.3). The softer (small γ) the EoS is, the higher the maximum density is. When the nuclear density ρ_0 is reached in the center, its EoS becomes stiffer and the inner region begins to compress like a spring. The compression happens until the maximum value of $\rho_c \approx 9.7 \cdot 10^{14}$ (maximum scrunch) is obtained. At this point, the shock then propagates outward. If the explosion happens, this is called the *prompt mechanism (bounce-shock mechanism [1])*. However, from simulations, this scenario does not lead to the final explosion.

The failure of this prompt mechanism happens due to the fact that the shock loses energy by two ways:

⁷For a very massive star, the collapse continues until a blackhole is formed.

Chapter 1. Core-Collapse Supernovae

1. Heavy nuclei dissociation
2. ν emission

The heavy nuclei dissociation⁸ to neutrons subtracts ~ 8.8 MeV per nucleon, about $1.7 \cdot 10^{51}$ erg per $0.1M_{\odot}$ traversed. The total energy of the shock is of the order of 10^{52} erg. Thus, the energy loss due to the total amount of material the shock needs to travel is significant.

The shock consists of neutrons, protons, and electrons (for neutrality condition). The favorable reaction is electron capture by proton producing neutrino electron,



Moreover, the positron (from $\gamma \rightarrow e^{+}e^{-}$) can produce neutrinos with $e^{+}e^{-} \rightarrow \nu_i\bar{\nu}_i$, in which $i = \{e, \mu, \tau\}$.

The high value of density traps the neutrinos. However, when the shock propagates outward, the density decreases and when $\rho < \rho_{\text{trap}} = 10^{12}$ g/cm³, neutrinos are released. Let's define the optical depth,

$$\tau = \int_0^R \frac{1}{\lambda_{\nu}} dr, \quad (1.18)$$

with $\lambda_{\nu} \equiv 1/(n_t\sigma)$ mean free path with number density of target n_t and cross section σ . In this case, we can define the neutrino sphere dividing the inner opaque core and the outer transparent region. Bethe and Wilson [5] calculates that this neutrino sphere (taking into account that ν 's do not propagate radially) lies on $\tau(R_{\nu}) = 2/3$. This τ value lies in a place far away outside from the ν -trapping region ($R_{\nu} \gg R_{\text{trap}}$). Thus, ν 's propagate diffusively for a long time before being emitted. The ν sphere is different for each different ν species (due to the difference in σ). When shock crosses the ν sphere, prompt emission of neutrinos happens with a peak ν luminosity (flash). This flash is also called the prompt neutronization peak since the ν_e 's are produced by the

⁸Including iron. For iron, the energy (see 1.11) per nucleon is $124.4/56 \sim 2.2$ MeV. There is also ⁴He dissociation $28.3/4 \sim 7$ MeV, and thus on average it will be ~ 8.8 MeV per nucleon.

neutronization processes. The electron neutrino luminosity rises at about 2 ms after the bounce ($R_{\nu_e} \sim 100$ km), so does simultaneously for $\bar{\nu}_e$ & ν_x . The energy involved in this prompt neutronization is of the order of 10^{51} erg — see the dashed line in figure 1.4.

Accretion and Cooling

The shock loses energy from the iron dissociation and neutrino emission and stops at $r \sim 100 - 200$ km. At this point, an accretion is created due to the fact that the matter from outward keeps falling with the free-fall velocity. This phase is called **accretion phase**. In this case, there will be a region between the core and the proto neutron star, that can be separated in,

- ν cooled region: emission of $\nu >$ absorption, for $r < R_g$, where the rate of cooling [7] is,

$$q_{\nu_e+\bar{\nu}_e}^+ \approx 160 \frac{L_\nu}{[10^{52} \text{ erg/s}]} \left(\frac{r}{[100 \text{ km}]} \right)^{-2} \left(\frac{k_B T_\nu}{[4 \text{ MeV}]} \right)^2 \text{ MeV s}^{-1} \text{ per nucleon,} \quad (1.19)$$

- ν heated region: emission of $\nu <$ absorption, for $r > R_g$, where the rate of heating [7] is,

$$q_{\nu_e+\bar{\nu}_e}^- \approx 145 \left(\frac{k_B T_\nu}{[2 \text{ MeV}]} \right)^6 \text{ MeV s}^{-1} \text{ per nucleon,} \quad (1.20)$$

where R_g is called gain radius. The time evolution of all-flavor neutrino luminosities during the collapse can be seen in figure 1.4. It is clearly visible that most of the total energy ($\sim 90\%$ of the total energy) is emitted in neutrinos in the time span of the order of 10 seconds. We will discuss the production of neutrinos during this phase deeper in chapter 2.

In the next section, we will discuss the possible shock revival mechanisms to trigger the explosion.

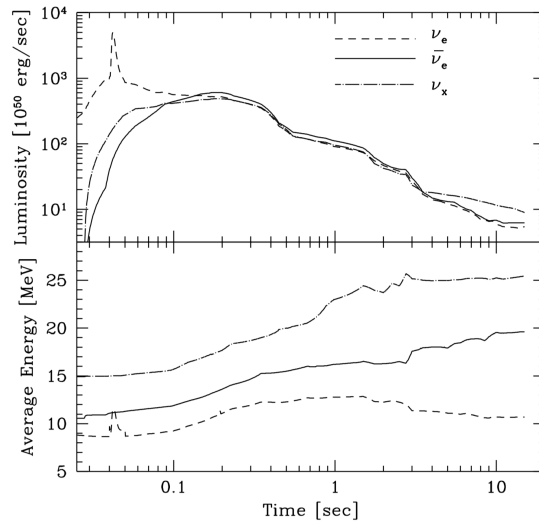


FIGURE 1.4: Neutrino luminosity (upper) and average energy (lower) during the collapse. Figure is taken from [11]. This figure indeed is very old and probably the first simulation study, however, the general behaviour of the curve is still relevant to explain a global picture of the neutrino emission. This figure could be compared with figure 2.8.

1.3 Shock Revival Mechanisms

In order to trigger an explosion, during the delayed heating by neutrinos, we need other mechanisms to optimise this heating and to revive the shock until it finally explodes. What will be the mechanisms? we will address this issue in this section.

We know that the neutrino-delayed mechanism is challenging for the simulations of the explosion since the shock loses energy and stops before being able to successfully explode the stars. However, there are several mechanisms that can revive the shock leading to the ejection of materials (more detailed review can be seen in [1]).

The simulations of low mass electron-capture supernovae (section 1.1) with neutrino-driven mechanism (section 1.2) can produce an explosion of the stars since they have ideal conditions for neutrino-energy transfer. The extremely steep gradient at the edge of O-Ne-Mg core causes the accretion shock to increase continuously. The explosion energy in this case is of the order of 10^{50} erg. This low energy (and low Ni ejection) is compatible with

the Crab SN. For more massive Fe-core progenitors we need nonradial hydrodynamic instabilities [12–14] (combined with standing accretion shock instability, SASI [15]) in order to give positive result for the neutrino-heating mechanism. SASI is a nonradial instability of stalled accretion shocks, leading to a large-scale shock deformation [16]. In other words, it is a large-amplitude sloshing and spiral motions of the shock with some harmonic modes. The growth of SASI comes from an advective-acoustic cycle in the region between the stalled shock and the accreting proto neutron star.

Moreover, nonradial-turbulent flows (more detail in [16]) can increase the time of matters in the gain layer as well as the total mass in the gain layer M_g (c.f. equation 5 in [1]). This could lead to higher total energy deposition rate by neutrinos ($Q_\nu^+ \sim q_\nu^+ \cdot M_g$) and to increase the total energy transfer. The enhanced energy transfer can push the shock further outwards and leads to an explosion. Moreover, SASI, especially the spiral modes [16], can also give a similar effect leading to secondary shocks. These secondary shocks dissipate kinetic energy and produce extra heating and higher entropy to strengthen convective activity and give additional push to the shock. However, we need to bear in mind that the nature of SASI, the role of hydrodynamic instabilities and turbulent motions leading the explosion are still ongoing research.

Additionally, in magnetohydrodynamic phenomena, especially the magnetorotational mechanism may lead to an explosion. Magnetorotational mechanism requires the progenitors having some value of stellar core-rotation and magnetic field configuration. These magnetorotational mechanism processes are considered to be able to tap energy from a highly magnetised-rotating neutron star and expel violently the outer parts of the stars. The rotational energy itself can be of a value of about 10^{52} erg [17] and if a small energy fraction can be tapped by some mechanism, this energy fraction may drive an explosion. During core-collapse, magnetic field lines are frozen and leads to compressional amplification of the nonradial field. Besides, and more importantly, a huge rotational energy can be converted to the amplification of the field by either wrapping a poloidal field and stretching it to a toroidal one or by

an exponential amplification through magnetorotational instability. Then, the ejection of matters can be driven by magnetic pressure, magnetic buoyancy or gas heating due to dissipation of rotational energy. To successfully explode the star via this magnetorotational mechanism, it is required that the core rotation period should be of the order of ~ 1 millisecond [1]. However, present stellar evolution suggests the typical core rotation period is of the order of ~ 100 seconds before the collapse⁹, which is too slow for the requirement of the magnetorotational mechanism. Indeed, other possible solutions to speed up the rotation may make the explosion via magnetorotational mechanism works.

In addition, at late times after bounce ($\gtrsim 1$ s), large-amplitude dipole gravity-mode oscillations of the proto neutron star core emerge due to SASI [15, 16, 18] and anisotropic accretion [1]. These proto neutron star core oscillations may have amplitude of several kilometers [1] and they propagate away to the surrounding medium in the form of strong sound waves. Then, the energy of these sound waves is dissipated in the stalled shock region. The stalled shock region will heat up and can lead to a strong explosion. Basically, the power of anisotropic accretion ($\sim 10^{52}$ erg/s) is converted to the acoustic power (of the order of $\sim 10^{51}$ erg/s). However, the fraction of the accretion power converted to g -mode in numerical calculations as well as the explosion energies are still uncertain.

Besides, a first-order hadron-to-quark matter phase transition (at a low density) may happen during the postbounce accretion phase of the core-collapse stars. This transition may have dynamical consequences towards an explosion. Thus, it is possible to use a hybrid EoS with a mixed phase (hadron & quark) [1]. This hybrid EoS drives the proto neutron star to be gravitationally unstable when it has accreted matter and heated up during the contraction. This can lead to a release of a fraction of gravitational binding energy and the formation of a strong second bounce shock (catching up the first stalled shock)

⁹that is consistent with the observations of newborn white dwarfs and pulsars (~ 10 ms).

Chapter 1. Core-Collapse Supernovae

which can drive an explosion. However, the quantum chromodynamics phase transition is still under development.

A thermonuclear mechanism can also give an explosion (in a different way from section 1.3, which is on the revivals of the stalled shock) for very massive progenitors ($M_* \gtrsim 100M_\odot$). This is due to the ignition of the still available thermonuclear fuel. This mechanism happens presently for pair-instability supernovae (section 1.1). Moreover, there is a proposed idea that neutrino radiation from the collapsing stellar core heats (mainly by neutrino-electron scattering) the degenerate C and O shell of low mass progenitors and igniting a thermonuclear burning leading to an explosion. However, this idea could not be verified by detailed progenitor and explosion models. In the low mass (O-Ne-Mg core progenitors), the C and O shell fall inward long before being exposed by a high fluence of neutrinos. While for Fe-core progenitors, O and C are too far outward to be exposed by a strong neutrino flux and electron densities there are very low which cannot raise the temperature (by neutrino-electron scattering) needed for explosion [1].

These mechanisms that we have discussed above will be tightly related to the emission of gravitational waves. This will be discussed deeply in the next chapter, particularly in section 2.3.

Chapter 2

CCSN Detectability

In the previous chapter, we have summarized the main astrophysical features of CCSNe from their different progenitors as well as the main phases of these core-collapsing events. Now, we are going to discuss the detectability of these objects. We will start by discussing the rate and distribution of CCSNe in our surroundings in section 2.1, then, we are going to move on to the discussion of their detection channels, i.e. low energy neutrinos in section 2.2 and GWs in section 2.3.

2.1 Rate and Distribution

We will summarize here the rate and distribution of supernovae from recent several studies based on the summary in [19]. Most information of supernova rate actually comes from the observations of extragalactic supernovae [19] in some galaxies. From the observations of supernovae in a certain galaxy, we can estimate the rate of supernovae in that galaxy. Then, that rate can be normalized to the rate for our Milky Way by using some quantity correlated with the stellar mass of the galaxy.

The B-band luminosity of the galaxy in question is commonly used to estimate the rate since it is a measure of a galaxy stellar mass, at least for galaxies inside the same morphological type. The rate is written basically as the number of supernovae per century per $10^{10} \mathcal{L}_{B,\odot}$, where $\mathcal{L}_{B,\odot}$ is the B-band solar

Chapter 2. CCSN Detectability

luminosity and the B-band luminosity of our galaxy is,

$$\mathcal{L}_{B,\text{Gal}} \simeq 2.3 \cdot 10^{10} \mathcal{L}_{B,\odot}. \quad (2.1)$$

With its given B-band luminosity, we can go further to normalize the supernova Milky Way rate in order to have the rate unit in events per century. There has been a study [20] of the supernova rates from the database of extragalactic supernova observations, for the different types of supernovae as well as for different classes of host galaxies. The summary of that study can be seen in table 2.1. Taking into account that our Galaxy to be the type of Sb-Sbc

TABLE 2.1: Supernova rates per galaxy type per century per $10^{10} \mathcal{L}_{B,\odot}$, with $h_0 = H_0/(100 \text{ km s}^{-1} \text{ Mpc}^{-1})$, taken from [20].

Galaxy type	SN type			
	Ia	Ib/c	II	All
E-S0	$0.32 \pm 0.11 h_0^2$	$< 0.02 h_0^2$	$< 0.04 h_0^2$	$0.32 \pm 0.11 h_0^2$
S0a-Sb	$0.32 \pm 0.12 h_0^2$	$0.20 \pm 0.11 h_0^2$	$0.75 \pm 0.34 h_0^2$	$1.28 \pm 0.37 h_0^2$
Sbc-Sd	$0.37 \pm 0.14 h_0^2$	$0.25 \pm 0.12 h_0^2$	$1.53 \pm 0.62 h_0^2$	$2.15 \pm 0.66 h_0^2$
All	$0.36 \pm 0.11 h_0^2$	$0.14 \pm 0.07 h_0^2$	$0.71 \pm 0.34 h_0^2$	$1.21 \pm 0.36 h_0^2$

with its rate following equation 2.1 and using $h_0 = 0.7$, the rate for different supernova types can be calculated as,

$$\begin{aligned} \mathcal{R}_G(\text{type Ib} + \text{Ic} + \text{II}) &= (1.7 \pm 1.0) \text{ events/century} \\ \mathcal{R}_G(\text{type Ia}) &= (0.5 \pm 0.2) \text{ events/century} \\ \mathcal{R}_G(\text{all}) &= (2.2 \pm 1.2) \text{ events/century} \end{aligned} \quad (2.2)$$

which is basically between 1 and 3 events per century. From that result, indeed we are interested in the joint rate for type Ib+Ic+II for which they undergo the core-collapsing processes¹.

¹This classification type Ib, Ic, and II are based on their light curves and the absorption lines of different chemical elements appearing in their spectra. Meanwhile, type Ia supernovae do not undergo the core-collapse processes and instead they are produced by a thermal runaway process.

Chapter 2. CCSN Detectability

The detection of neutrinos from *extragalactic* SN1987A in Large Magellanic Cloud² [21–23] shows that we have the capability to observe neutrinos from CCSNe, with clarity, in our Milky Way galaxy. Taking into account that we have not received yet any astrophysical neutrinos from *galactic* CCSNe until now in our neutrino detectors, we can estimate an upper bound of galactic CCSN rate. The upper bound rate [24] can be written as,

$$\mathcal{R}_G(\text{type Ib} + \text{Ic} + \text{II}) < 7.7 \text{ events/century.} \quad (2.3)$$

Furthermore, a direct estimation of CCSNe rate in our Galaxy can also be done via the γ -rays produced by the radioactive decay of ²⁶Al [25], taking into account that ²⁶Al is mostly produced by massive stars. This gives us a prediction of,

$$\mathcal{R}_G(\text{type Ib} + \text{Ic} + \text{II}) = (1.9 \pm 1.1) \text{ events/century,} \quad (2.4)$$

which is in a quite good agreement with equation 2.2. Based on all the studies above, we can more or less conclude that CCSNe in our Galaxy may happen as often as 1 per 30 years.

From the study of the rate of CCSNe in our Galaxy, in fact, we can also make a prediction how probable it is to detect one or more CCSNe in our Galaxy let's say for the next 10, 20, and 30 years depending on the rate that we assume. This prediction can be seen in figure 2.1 based on the study of [26] taking into account the Poisson distribution for a given supernova rate.

For astronomers, besides the rate, it is also important to understand the (expected) distribution of supernovae in our Galaxy. The probability density function (PDF) of finding supernovae as a function of distance from our sun towards the galactic center can be seen in figure 2.2. That figure is estimated by performing Monte Carlo simulations based on the distribution of supernova remnants in our galaxy also taking into account the spiral arms in order to

²We will discuss SN1987A in more detail in chapter 3.

Chapter 2. CCSN Detectability

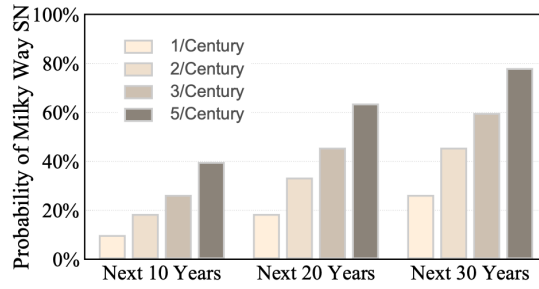


FIGURE 2.1: Probabilities to find one or more CCSNe in the Galaxy for the next 10, 20, and 30 years, depending on the assumed rate. Figure is taken from [26].

perform the simulation in a realistic galaxy model [27]. The probability spans in a broad range and we can also say that there is a bigger probability to find supernovae in a range of 5 to 18 kpc from us.

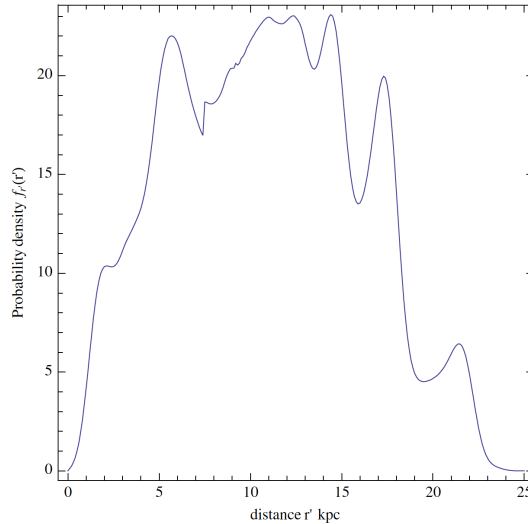


FIGURE 2.2: PDF of finding CCSNe from our sun towards the galactic center (taken from [27]).

This 5-18 kpc distance range will be crucial since this means there is a probability that a CCSN happens on the other side of the galactic center that could be unobservable electromagnetically due to the “pollution” by the galactic center and therefore neutrino detectors will play an important role here. The current neutrino detectors (more in chapter 3) have CCSN horizon of up to Large/Small Magellanic Cloud (~ 60 kpc). In terms of GWs, this distance range could be also a problem since it is actually on the sensitivity edge of GW detectors (more in chapter 3) to detect CCSNe.

Chapter 2. CCSN Detectability

Let us move further from our Galaxy and then we can also see the cumulative supernova rate in the nearby universe. Figure 2.3 from [28] is the result of the actually detected CCSNe in the local universe (distance $\lesssim 10$ Mpc) during 1999-2008 period. The dashed line is the prediction rate from table 2.1. It shows that the CCSN rate can reach 1 event per year at a distance of about 6 Mpc. In addition, at 10 Mpc, the rate could be around 2 events per year. This

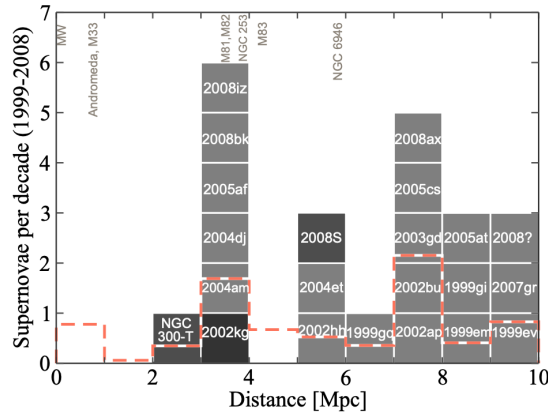


FIGURE 2.3: The CCSN rate estimation in the nearby universe, based on 22 supernovae observations in 1999-2008 (bins), compared with the prediction using B-band luminosity (dashed line). Figure is taken from [26].

knowledge can also be acquired, for the cumulative CCSN rate as a function of distance, from figure 2.4, based on 22 supernova observations in 1999-2008. In figure 2.4, it is also plotted, for a comparison, the theoretical predictions in B-band from 451 galaxies and UV from 315 galaxies as well as their combination and the detection probability of several future detectors is also shown.

Based on our study on the rate and distribution of CCSNe, it can be seen that we need to further improve our capability to detect CCSNe to the scale of a Mpc horizon in order to get a reasonable rate to observe them ($\lesssim 1$ per year), which is basically the horizon goal of future neutrino detectors. After reviewing this rate and distribution, we will move on to the discussion of the detection channels of CCSNe in the following section.

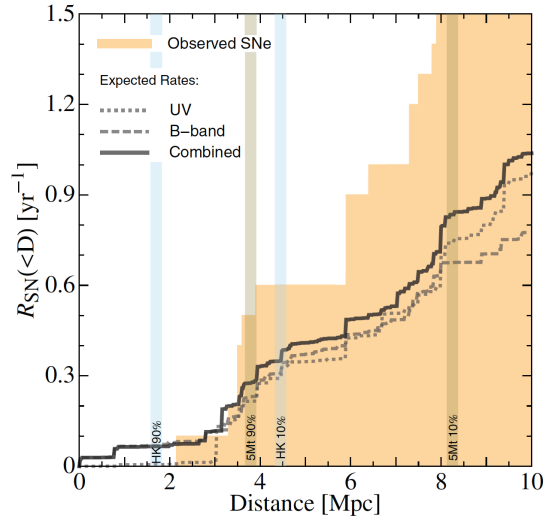


FIGURE 2.4: Observed CCSN cumulative rate as a function of distance (taken from [28]). It is also shown the expected rate based on different electromagnetic emissions and the distances where the detection probability is 90% & 10% for 560 kton HK (Hyper-Kamiokande) & 5Mton neutrino detectors. This figure is based on 22 SN observations in 1998-2008 and in comparison with some theoretical predictions.

2.2 Neutrino Emission

As stated before, low-energy neutrinos are important messengers to study CCSNe, which is evident from the neutrino detection of SN1987A [21–23]. Here we will focus on a brief explanation of neutrino emission and its detectability before the collapse, during the bounce, accretion, and cooling phase.

Indeed, even before the collapsing phase, supernova progenitors already produce strong-luminosity MeV-neutrinos from thermal emission of advanced burning phases, as for example the Si burning. These pre-supernova neutrinos could be possibly detected [29–32] by the ultrapure liquid scintillator detectors such as Borexino [33], KamLAND [34], JUNO [35], as well as DUNE [36] (or even Super Kamiokande [37] with the help of Gadolinium). The main detection channel to detect these low-energy CCSN neutrinos is basically the inverse beta decay (IBD) happening in neutrino detectors³,

$$\bar{\nu}_e + p \rightarrow n + e^+ \quad (2.5)$$

³The detector discussion is in chapter 3.

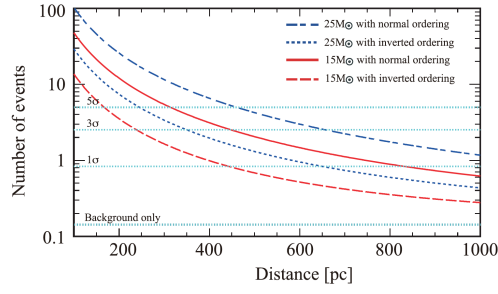


FIGURE 2.5: Expected number of IBD events gathered by KamLAND [34] during the 48 hours before collapse, taking into account ν oscillation effects, as a function of distance. As the case study here, it is shown the flux for a $15M_{\odot}$ and $25M_{\odot}$ star assuming the normal and inverted neutrino hierarchy. The significance levels are shown with the horizontal dotted lines. Figure is taken from [31].

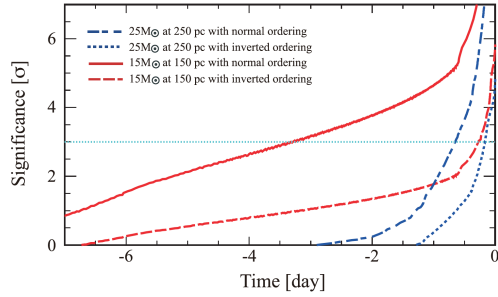


FIGURE 2.6: Time evolution of significance. If Betelgeuse star has a mass of $15M_{\odot}$ and with the distance at 150 pc, the 3σ detection by KamLAND [34] (a dotted horizontal line) is 89.6 (7.41) hours with normal (inverted) hierarchy before its collapse. Meanwhile, if the stellar mass is $25M_{\odot}$ at 250 pc, the pre-supernova alert is detectable within 17.0 (4.54) hours before its collapse at 3σ confidence level. Figure is taken from [31].

KamLAND [34] collaboration has studied that their detector can detect these pre-supernova neutrinos from a star with a mass of $25M_{\odot}$ at a distance less than 690 pc with 3σ significance before the supernova, dependent on the neutrino mass ordering and background levels [31]. The detector gathers data continuously and can provide this pre-supernova alert. The expected number of IBD events detected by KamLAND from a pre-supernova can be seen in figure 2.5, meanwhile, its significance level as a function of pre-collapse time can be seen in figure 2.6. This detection will be a well advanced warning of the order of a few to tens of hours before a CCSN happens⁴ as well as revealing the timing of the final core and the shell burning phases.

⁴The $t = 0$ is when the bounce happens.

Bounce and Burst

During the Fe-core collapse, electron neutrinos are produced by electron captures on heavy nuclei and few free protons. Around the time of trapping ν_e luminosity reaches $\sim 10^{53}$ erg/s with the mean energy of ~ 10 MeV. The trapping makes a small dip of luminosity due to the fact that neutrinos only come from a narrow region around the newly formed neutrinosphere. Neutrino emission again increases rapidly after the core bounce as newly formed shock propagates into regions of sufficiently low density and reaches neutrinosphere thanks to the shock heating and low optical depth. The dominant production is still ν_e due to the high Y_e in the shock. The luminosity of this *burst* of neutrinos can reach $\sim 3.5 \times 10^{53}$ erg/s, known as neutronization burst (or prompt neutronization peak in subsection 1.2). A Mton water Cherenkov detector like Hyper Kamiokande [38] can observe this burst, which would be a *standard candle* with distance error measurement of $\sim 5\%$. Moreover, the nonobservation of this peak will support the normal mass hierarchy in neutrinos, while the observation will be consistent with the inverted hierarchy⁵ (see more in [40]).

Electron neutrino burst and the rise phase of $\bar{\nu}_e$ & ν_x give precise timing of the bounce. Assuming the normal hierarchy, IceCube [41] can determine the bounce ~ 3.5 ms using the rise of $\bar{\nu}_e$ flux [42], which is very important in terms of multimessenger with GWs. If both messengers are correlated, they will improve the parameter estimation, especially for the bounce of rotating progenitors [43].

Accretion and Cooling

Around ten of millisecond timescale, the CCSN core develops a structure like in figure 2.7. Accretion shock lies on $\sim 100 - 200$ km from the center. Then,

⁵In addition, the rise time of $\bar{\nu}_e$ light curve can also be a probe to this problem [39], where the fast rise time ($O(100$ ms)) will agree with the inverted hierarchy.

Chapter 2. CCSN Detectability

below it, there is a hot bubble region with high entropy dominated by photons and electron-positron pairs, as well as heating by neutrinos from inside dominates the neutrino cooling. Further inside, there is a high density region, spanning from $\sim 10^{10}$ to a few 10^{13} g/cm³, and the pressure is described by ideal gas. Between the hot bubble and this ideal gas region, neutrino cooling dominates over the heating.

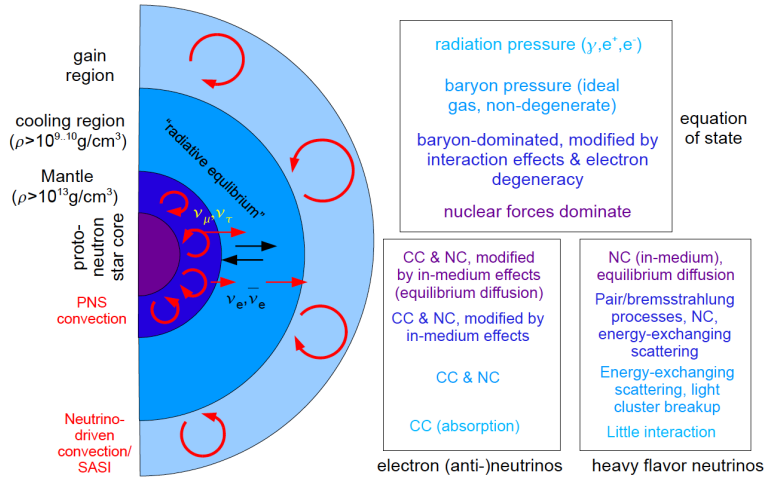


FIGURE 2.7: The scheme of regions in SN core. CC: charged-current, NC: neutral-current. Figure is taken from [44].

Neutrino emission for electron and heavy flavor is quite different in this phase. For all flavors during this phase, there is a diffusive flux to proto neutron star surface region driven by temperature gradient and neutrino chemical potential. This diffusive flux is determined by temperature and radius of neutrino sphere near the proto neutron star surface. The diffusive neutrino flux is well described by gray-body emission law,

$$L_{\text{diff}} = 4\pi\phi\sigma_{\text{Fermi}}R^2T^4, \quad (2.6)$$

where ϕ is a *grayness factor*, meaning that it is a deviation from Stefan-Boltzmann. This equation is sufficient to describe the heavy-flavor neutrino luminosity in which the grayness parameter $\phi = [0.4 - 0.6]$ during the pre and early explosion [45].

Moreover, for electron flavor neutrinos, the emission is not only due to the diffusion of thermal energy from the proto neutron star core, but also from the accretion. Accreted matter is accumulated on proto neutron star surface and is in a state of radiative equilibrium with deeper layers, thus, must undergo net neutrino cooling to maintain constant temperature when it is compressed to higher densities. Heavy flavor neutrinos can only be produced in high density and not by charged-current processes, therefore, the only dominant process to the cooling is by emission of ν_e & $\bar{\nu}_e$. Only about half of accretion energy goes to electron-flavor neutrinos since the accreted matter cannot cool down below the radiative equilibrium temperature. Thus, the luminosities,

$$L_{\nu_e} + L_{\bar{\nu}_e} = 2\beta_1 L_{\nu_x} + \beta_2 \frac{GM\dot{M}}{R} \approx 2L_{\nu_e} \approx 2L_{\bar{\nu}_e}, \quad (2.7)$$

where M stands for the proto neutron star mass, \dot{M} is accretion rate, $\beta_1 = 1.25$ and $\beta_2 = 0.5$ are nondimensional parameters. Moreover, simulations show that the mean energy of electron antineutrinos $\langle E_{\bar{\nu}_e} \rangle$ is somewhat proportional to proto neutron star mass during the accretion (see equation 8 in reference [44]),

$$\langle E_{\bar{\nu}_e} \rangle \approx 10 \text{ MeV} (M/M_\odot). \quad (2.8)$$

During the cooling phase, the electron flavor and heavy flavor luminosity become relatively similar (see figure 2.8 right column). The luminosity of all flavors decreases roughly exponentially with a decay time-scale of seconds. Despite this decrease, the surface temperature as well as the mean energies of neutrinos still increase in around 1 second after the bounce due to the contraction of the proto neutron star [44]. Later on, when the proto neutron star cools down, the mean energies of all flavors converge to one single value.

From chapter 1 regarding the astrophysical phases of CCSNe, it has been seen that there is an accretion phase that lies on the accretion region between the core and the proto neutron star. During this accretion phase in the delayed neutrino heating mechanism, the ν 's from the cooled region (equation 1.19) are

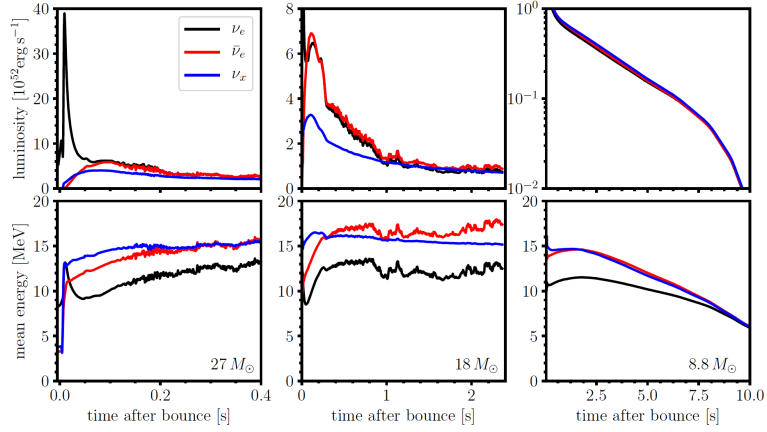


FIGURE 2.8: Neutrino luminosities and mean energies from simulations. Left figure is the 2D simulation of $M = 27M_{\odot}$ for the burst, accretion, and early explosion phase. The middle is for 3D simulation of $M = 18M_{\odot}$ until the explosion phase where there is somewhat equipartition for different flavors. The right is for $8.8M_{\odot}$ showing the Kelvin-Helmholtz cooling phase. Figure is taken from [44].

absorbed in the heated region (equation 1.20) by,



Due to this neutrino heating, the pressure increases behind the shock and the heated layers expand. During this phase, 10-20% of ν_e - $\bar{\nu}_e$ energy is converted to thermal energy and can revive the shock. The timescale in this phase is $t \sim 0.5$ sec.

Then, a fraction of infalling materials adds to the proto neutron star until the explosion. The proto neutron star evolves to be a neutron star with the radius R_{NS} . Most of CCSN energy is emitted in this phase (called **cooling phase**), accounting for $\sim 90\%$ in the form of all neutrino and antineutrino species with high luminosity (see figure 1.4 and 2.8). The primary production of neutrinos in this phase is the neutral current (for all neutrino and antineutrino species),

$$\begin{aligned}
 e^+ e^- &\rightarrow \nu_i \bar{\nu}_i && \text{pair annihilation} \\
 e^\pm + (p, n) &\rightarrow e^\pm + (p, n) + \nu_i + \bar{\nu}_i && \text{electron - nucleon Bremsstrahlung} \\
 \gamma_p &\rightarrow \nu_i + \bar{\nu}_i && \text{plasmon decay} \\
 \gamma + e^\pm &\rightarrow e^\pm + \nu_i + \bar{\nu}_i && \text{photo annihilation,}
 \end{aligned}
 \tag{2.10}$$

and, similar to the accretion phase, the charged current (for electron neutrinos and antineutrinos),

$$\begin{aligned}
 e^- + p &\rightarrow n + \nu_e \\
 e^+ + n &\rightarrow p + \bar{\nu}_e.
 \end{aligned}
 \tag{2.11}$$

In this last phase, a large amount of (anti)neutrinos from all species is produced with a thermal⁶ emission due to the ν production in an opaque region.

Pagliaroli Parametrization for the Accretion and Cooling

Based on the previous description on the different neutrino emission phases, it is possible to parametrize the electron antineutrino flux from the accretion and cooling phase. Detailed explanation on this parametrization can be seen in [2, 46, 47]. As we know that the main detection channel of these neutrinos coming from CCSNe is basically the IBD (equation 2.5), therefore, we will focus on this channel. The number of expected neutrino events from IBD can be written as,

$$\begin{aligned}
 R(t, E_e, \cos(\theta)) &= N_p \frac{d\sigma_{\bar{\nu}_e, p}}{d \cos(\theta)}(E_\nu, \cos(\theta)) \cdot \Phi_{\bar{\nu}_e}(t, E_\nu) \\
 &\quad \times \xi_d(\cos(\theta)) \cdot \eta_d(E_e) \cdot \frac{dE_\nu}{dE_e},
 \end{aligned}
 \tag{2.12}$$

where N_p is the number of free protons in a detector, $\sigma_{\bar{\nu}_e, p}$ is the inverse beta decay cross section (see [48]), η_d is the detection efficiency of each detector,

⁶Thermal: Maxwellian distribution of plasma, energy exchange by collision & photon exchange; nonthermal: sort of power law distribution.

Chapter 2. CCSN Detectability

ξ_d is the angular bias⁷, and $\Phi_{\bar{\nu}_e}$ is the electron antineutrino flux. The electron antineutrino flux in the *accretion* phase⁸ can be parameterized as,

$$\Phi_a^0(t^{\text{em}}, E_\nu) = \frac{1}{4\pi D^2} \frac{8\pi c}{(hc)^3} \times [N_n(t^{\text{em}}) \sigma_{e+n}(E_\nu) g_{e+}(\bar{E}_{e+}(E_\nu), T_a(t^{\text{em}}))], \quad (2.13)$$

where t^{em} is the emission time⁹, $N_n(t^{\text{em}})$ is the number of target neutrons at rest in the cooling region between the proto neutron star and the shock, σ_{e+n} is the IBD cross section as a function of neutrino energy, and $g_{e+}(\bar{E}_{e+}(E_\nu), T_a(t^{\text{em}}))$ is the thermal flux of positron. The electron antineutrino spectrum is slightly nonthermal because of the presence of σ_{e+n} includes an additional E_ν dependence. Thus, the average neutrino energy is $\sim 5T_a$. Moreover, the scaling of luminosity with temperature becomes $\propto T_a^6$ which means nonthermal instead of $\propto T_a^4$ for thermal scaling. If suppose at $t^{\text{em}} = 0$ we have $T_a = 2.5$ MeV and $M_a = 0.15 M_\odot$, with the nonthermal scaling, we will get luminosity of $\sim 1.1 \times 10^{53}$ erg/s while if we use a thermal black-body scaling, we need $T = 4.1$ MeV and $R = 82$ km.

On the other hand, the cooling phase¹⁰ is consistent with thermal black-body emission. The electron antineutrino flux can be written as,

$$\Phi_c^0(t^{\text{em}}, E_\nu) = \frac{1}{4\pi D^2} \frac{\pi c}{hc^3} [4\pi R_c^2 g_{\bar{\nu}_e}(E_\nu, T_c(t^{\text{em}}))], \quad (2.14)$$

with,

$$T_c(t^{\text{em}}) = T_c \exp[-t^{\text{em}}/(4\tau_c)], \quad (2.15)$$

where R_c is the radius of the emitting region (neutrino sphere), T_c is the initial temperature, and τ_c is the time constant of the process, respectively, in addition, $g_{\bar{\nu}_e}$ is the Fermi-Dirac spectrum,

$$g_{\bar{\nu}_e}(E_\nu, T_c(t^{\text{em}})) = \frac{E_\nu^2}{1 + \exp(E_\nu/T_c(t^{\text{em}}))}. \quad (2.16)$$

⁷ $\xi_d = 1$ for Kamiokande-II and Baksan, while $\xi_d(\cos(\theta)) = 1 + 0.1 \cos(\theta)$ for IMB [46].

⁸The subscript "a" stands for accretion.

⁹ $t^{\text{em}} = 0$ for the start of emission, by definition.

¹⁰The subscript "c" for cooling.

We recall which are the generic expectations: $R_c \sim R_{\text{NS}} = 10 - 20$ km, $T_c = 3 - 6$ MeV, and $\tau_c = \text{few-many}$ seconds, which is the result in [2, 46]. This parametrization has been proven useful in improving the analysis of SN1987A [46] to determine its astrophysical quantities, such as T_c , M_c , R_c , etc. Thus, this may allow us to fit the future neutrino data from CCSNe to determine such quantities.

We have discussed the neutrino emission in CCSNe. Therefore, from the neutrino emission in CCSNe, we will move to the next section on how these same CCSNe can also become the powerhouse of GWs.

2.3 GW Emission (Models)

A source that generates the gravitational waves must have quadruple mass moment rapidly changing in time. With some algebra, based on [24], we can derive that the GW equation will have the form of,

$$\begin{aligned} [h_{ij}^{\text{TT}}(t, \mathbf{x})]_{\text{quad}} &= \frac{1}{r} \frac{2G}{c^4} \Lambda_{ij,kl}(\hat{n}) \ddot{I}_{kl}(t - r/c) \\ &= \frac{1}{r} \frac{2G}{c^4} \ddot{I}_{ij}^{\text{TT}}(t - r/c), \end{aligned} \quad (2.17)$$

where r is the distance from the source, c is the speed of light, G is the gravitational constant, $\Lambda_{ij,kl}(\hat{n})$ is a projector tensor (explained in [24]) to the transverse-traceless gauge (appendix B), written with the superscript “TT”, and \ddot{I}_{kl} is the second time-derivative of quadrupole mass moment,

$$\ddot{I}_{kl} = \int \rho \left(x_k x_l - \frac{1}{3} \delta_{jk} r^2 \right) d^3x \quad (2.18)$$

The derivation of this formula can be seen in many literatures such as [24, 49–51] just to name some.

Many simulations have been developed on the gravitational waves coming from CCSNe under the quadruple approximation as numerical and phenomenological waveforms. A thorough review for this topic can be seen such

as in [52]. Basically, there are some key properties to produce these numerical and phenomenological waveforms (more in [53]). They are the total emitted GW energy E_{GW} , the angle-averaged *root-sum-squared* GW strain $\langle h_{\text{rss}} \rangle$, the peak frequency of the wave f_{peak} (the frequency where dE_{GW}/df peaks). The energy of GWs can be written as,

$$E_{\text{GW}} = \int_0^\infty \frac{dE_{\text{GW}}}{df} df, \quad (2.19)$$

with,

$$\frac{dE_{\text{GW}}}{df} = \frac{2}{5} \frac{G}{c^5} (2\pi f)^2 \left| \tilde{I}_{ij}^{\text{TT}} \right|^2, \quad (2.20)$$

where the last part of that equation is defined as,

$$\tilde{I}_{ij}^{\text{TT}}(f) = \int_{-\infty}^\infty dt \ddot{I}_{ij}^{\text{TT}}(t) e^{-2\pi i f t}, \quad (2.21)$$

being the Fourier transform of $\ddot{I}_{ij}^{\text{TT}}(t)$. The polarization amplitudes h_+ & h_\times can be written in spherical harmonics.

Meanwhile, the root-sum-squared strain h_{rss} is defined as,

$$\begin{aligned} h_{\text{rss}} &= \left[\int_{-\infty}^\infty dt [h_+^2(t; \iota, \varphi) + h_\times^2(t; \iota, \varphi)] \right]^{1/2} \\ &= \left[\int_{-\infty}^\infty dt \overline{(h_+ - ih_\times)} (h_+ - ih_\times) \right], \end{aligned} \quad (2.22)$$

and from here, we can get the angle-averaged root-sum-squared GW strain $\langle h_{\text{rss}} \rangle$ by integrating it over all source angles,

$$\langle h_{\text{rss}} \rangle = \iint d\Omega h_{\text{rss}}. \quad (2.23)$$

More detailed derivation of these properties, indeed, can be seen in [53].

Those properties above are the basic inputs to produce numerical and phenomenological waveform simulations of GWs from CCSNe in 2D and 3D. In [53], it has been used several numerical and phenomenological waveforms with various values of $\langle h_{\text{rss}} \rangle$, f_{peak} , and E_{GW} depending on the mechanisms

producing GWs in CCSNe. They do that in order to study the possible GW detections from CCSNe in the advanced detectors (more of the detectors will be discussed in chapter 3). There are very diverse mechanisms to produce GWs from CCSNe such as magnetorotational hydrodynamics mechanism, neutrino mechanism, acoustic mechanism, and so on, and we will discuss those mechanisms in the next several passages.

Magnetorotational Hydrodynamics

During core collapse, the stellar core will be spun up of a factor of 1000 comparing to the progenitor core, thanks to the conservation of angular momentum. In other words, if the pre-collapse core has a spin period of ~ 1 second, then the proto neutron star, after the collapse, will have a spin period of the order of milliseconds. This rapidly milisecond-spinning compact remnant has a rotational energy of about 10^{52} erg. If there is a way to tap a fraction of this humongous energy source, a strong explosion will be produced. In the following paragraphs, we will discuss the possible GW signal production from CCSNe due to magnetorotational hydrodynamics based on [17, 53].

The gravitational wave signal produced by this mechanism is dominated by bounce and subsequent ringdown of the proto neutron star [17, 53]. Strong centrifugal deformation of inner core, which is related to oblateness, due to rapidly rotating precollapse core, gives a large time-varying quadruple mass moment. This means the strong GW burst will emerge, and indeed the strength does depend on the inner core mass, angular momentum distribution, and EoS [53].

The angular velocity distribution of the precollapse core is somehow uniform in the inner subsonic collapsing core, due to the homologous collapse. Nevertheless, in the supersonic collapsing outer core ($r \gtrsim 40$ km in figure 1.4 c.f. in reference [2]), the homologous collapse gives rise to strong rotation gradients¹¹. Therefore, unlike the non-rotating CCSNe, the convection plays an

¹¹The outer core and the region between proto neutron star & shock be strongly differentially rotating.

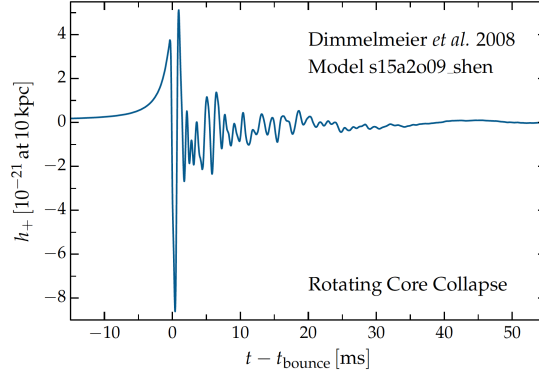


FIGURE 2.9: A plot of h_+ evolution from a simulated GWs from a rapidly rotating CCSN based on magnetorotational mechanism, at a distance of 10 kpc. Figure is taken from [17] based on [54].

insignificant role and thus GW signature due to turbulent convection is not present. However, for slowly rotating CCSNe (~ 10 ms instead of ~ 1 ms period), the prompt convection may produce some GW signal.

The characteristic of GW signal for this rapidly rotating CCSNe will have the peak of the detected strain amplitude (h_+ & h_\times) of the order of $\sim 10^{-21} - 10^{-20}$ at a distance $D \sim 10$ kpc. The energy produced in GW, ε_{GW} will be of the order of $10^{-10} - 10^{-8} M_\odot c^2$. Moreover, the frequency will be narrowband with most emitted power lies on 500 – 800 Hz. The timescale for this GW burst will be around ~ 10 ms. An example h_+ evolution of a simulated GW signal based on magnetorotational mechanism from a rotating CCSN can be seen in figure 2.9.

Meanwhile, for slower initial precollapse spin of the the core ($\lesssim 0.5 - 1$ s), core bounce occurs slowly at subnuclear density with the dynamics are dominated by centrifugal effects and most of its GW energy lies on ~ 200 Hz.

Neutrino Mechanism: Convection and SASI

GW signal from ν -driven CCSNe mostly is from turbulent convection and SASI [15]. In a CCSN, postbounce core is unstable to convection. Immediately, negative entropy gradient behind the stalled shock is formed and the *prompt convection* carries on, giving rise to a GW burst. Moreover, when the

Chapter 2. CCSN Detectability

postbounce evolution proceeds, ν -heating sets up negative entropy gradient in the gain layer behind the shock, leading to the ν -driven convection. Simultaneously, the ν -diffusion establishes negative lepton gradient in the mantle of proto neutron star, giving rise to *proto neutron star convection*. In brief, there are three different convections happening with different characteristic frequencies:

- prompt convection, immediately after the bounce, GWs lie on $\sim 100 - 300$ Hz,
- ν -driven convection at later times, produces GWs with significant power on $\sim 300 - 1000$ Hz (frequency increases in time), and
- proto neutron star convection causes the time-varying quadruple mass moment happens in the highest frequency $\gtrsim 1000 - 1100$ Hz.

GWs die down when the entropy gradient smooths out. Nevertheless, there will be gain in GWs at later times as the shock front becomes unstable to SASI (in addition to convection, depending on the progenitor structure and possibly even depending on the dimension of simulation 2D vs 3D) and being nonlinear on timescale ~ 100 ms. Accretion plumes are rapidly decelerated as they enter the region behind the shock, leading to the time-variations of quadruple moment and those are in numerous spikes in GW spectrum.

The frequency content in the neutrino mechanism is robust, but the phase is stochastic (due to turbulence). The signal is long lasting of about $\sim 0.3 - 2$ seconds. The GW strain amplitude is about 1 order of magnitude weaker than the GWs from magnetorotational processes (the previous subsection), h_+ (and h_\times) $\approx 10^{-22}$ at the distance $D = 10$ kpc. The energy in gravitational waves E_{GW} is of the order of $\sim 10^{-11} - 10^{-9} M_\odot c^2$. An example of the h_+ evolution from a simulated GW signal due to ν -mechanism (convection and SASI) from a CCSN at 10 kpc can be seen in figure 2.10. This model shows us that the GW signal can last up to 1 second with strong spikes early on and around 600 milliseconds after the bounce.

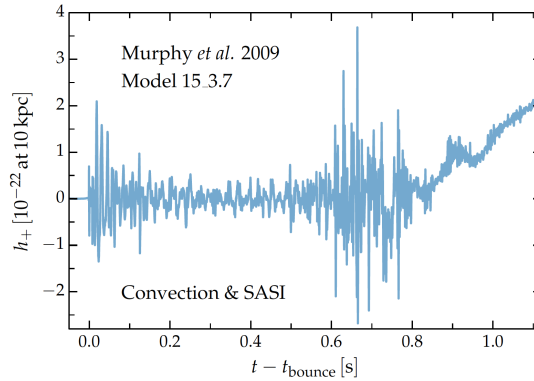


FIGURE 2.10: A plot of h_+ evolution from a simulated GW signal from a CCSN due to convection and SASI as seen by an equatorial observer at 10 kpc. This figure is taken from [17] based on the work of [13].

We have discussed the magnetorotational hydrodynamics and neutrino mechanism. In the next passage, we will discuss other mechanisms that could also generate GWs though less common.

Acoustic Mechanism and Others

Besides the two common models (magnetorotational hydrodynamics and ν -mechanism), there is also another model based on proto neutron star g -mode oscillation [55], that can produce gravitational waves from acoustic power generated in the inner core as the driver. This mechanism generates an oscillation mode with a period of 3 ms that grows at late times and be prominent at around ~ 500 ms after bounce. This acoustic power comes from the gravitational energy during the infall phase. This core oscillation can be considered as a transducer to convert the accretion energy into sound, thus, it is called acoustic mechanism. However, there is no confirmation from other groups regarding this simulation.

Some simulations and analyses of GWs from CCSNe include other mechanisms such as the works in [14, 56, 57]. The result of [56, 57] tells us these modes: “A mode” is due to the g -mode oscillation mechanism, happening at the PNS surface and “B mode” is due to the mass accretion by SASI, shown in figure 2.11. Moreover, they also show us that there appears some other modes,

besides the principal modes. One mode may be related to the convection excitation of the proto neutron star, denoted as “C mode” in figure 2.11, which is likely to arise from one of the p -mode oscillations from its frequency range, evolution, and spatial origin (p -mode is explained in [58]). Meanwhile, “D mode” could be actually interpreted as the overtone of SASI since $f_D \approx 2f_B$, though not exactly (~ 5 Hz difference). This ~ 5 -Hz frequency difference could be the relative phase change of h_+ and h_\times , as the change in circular polarization of Stokes V parameter (2.12). In addition, in [56, 57] studies, they also find f -mode oscillation of the proto neutron star [59] (besides g -mode and SASI). In addition, this GW strength produced by CCSNe depends on the star’s mass, EoS, and transport properties in warm nuclear matter.

All in all, we can basically summarize the different mechanisms that play a role in generating GWs from CCSNe in the table 2.2 borrowing from [52]. Magnetohydrodynamics mechanism and acoustic mechanism may give a strong GW signal depending on the emission processes. This diverse mechanisms could make it difficult to recognise signals from CCSNe in GW data, nevertheless, the future GW detections from CCSNe may let us understand which models correctly describing the CCSNe.

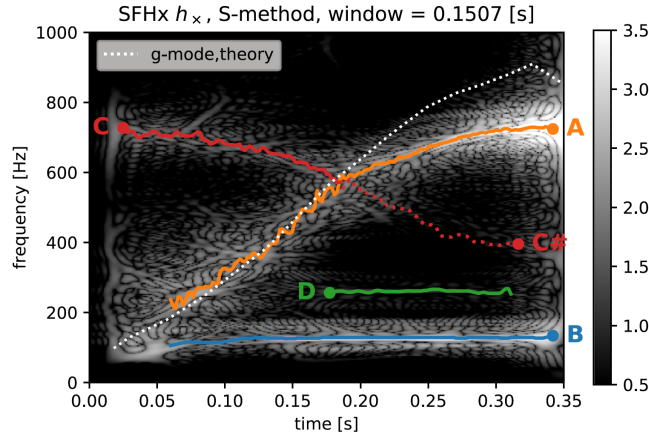


FIGURE 2.11: A time-frequency map of a GW simulated signal analysis from [14] model with EoS from [60]. It is also plotted the different modes from this signal: A due to acoustic mechanism, B due to SASI, C (and C#) due to p -mode, and D due to the overtone of B-mode.

Chapter 2. CCSN Detectability

TABLE 2.2: GW emission processes in CCSNe and the possible emission strength for different possible mechanisms. For a galactic SN, “strong” means a high probability of detection by initial and advanced LIGO, “weak” is referred to marginal probability to be detected by advanced LIGO, and “none” means probability of non detection by advanced LIGO. These three explosion mechanisms likely produce exclusive GW signatures and the detection or non-detection of a GW signal may give a hint of the mechanism. MHD stands for Magnetohydrodynamics and PNS is the abbreviation of proto neutron star. Table is taken from [52].

GW emission processes	Potential explosion mechanisms		
	MHD (rapid rotation)	Neutrino (slow/no rotation)	Acoustic (slow/no rotation)
Rotating collapse and bounce	Strong	None/weak	None/weak
3D rotational instabilities	Strong	None	None
Convection & SASI	None/weak	Weak	Weak
PNS g -modes	None/weak	None/weak	Strong

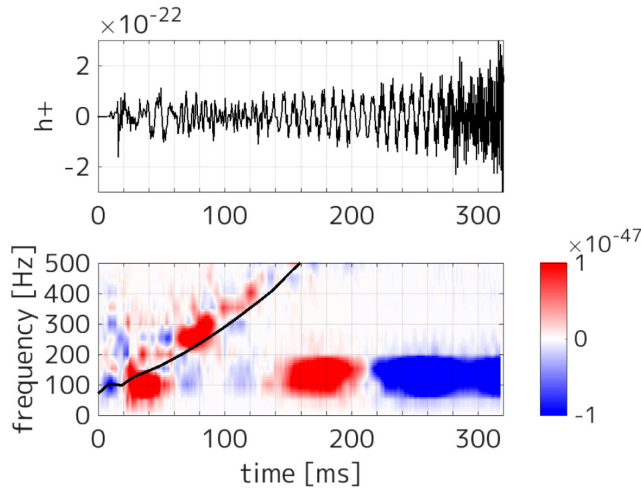


FIGURE 2.12: A gravitational waveforms h_{\times} (top) and the spectrogram (bottom) for the Stokes V parameter of SFHx EoS ([60]) taken from [56]. The black line in the spectrogram corresponds to g -mode. In the frequency of 100-200 Hz, there is a phase change in the Stokes V parameter (red to blue) which could explain the frequency difference of the D overtone mode (see text).

Chapter 3

Detectors, Analyses, and Detections

We have studied the astrophysical processes (chapter 1) as well as the emitted signals (chapter 2) of CCSNe. In this chapter, we will move on our discussion on the reviews of the involved detectors, analyses, and strategies aiming to reach successful CCSN detections in both neutrino (section 3.1) and gravitational wave (section 3.2) channel. We will also mention some successful GW observations from non-CCSN astrophysical sources till now.

3.1 The Neutrino Channel

As we have already discussed in the previous two chapters, CCSNe produce a lot of low energy neutrinos that can be studied primarily via inverse beta decay process. There are several types of neutrino detectors sensitive to CCSNe. Here we will briefly mention some classes of detectors based on [61, 62]. Practically, most of these neutrino detectors are built in order to observe other purposes like proton decay searches, solar/atmospheric neutrinos, as well as accelerator neutrino oscillation studies. The summary of different detectors can be seen in table 3.1.

Scintillator and water Cherenkov are sensitive primarily to $\bar{\nu}_e$; while those with neutral current (NC) capability such as heavy water and high Z /neutron are sensitive to all flavors. Water Cherenkov and heavy water have pointing capabilities. All but radio-chemical detector can see neutrinos in real time. In addition, all classes except long-string water Cherenkov and radio-chemical

Chapter 3. Detectors, Analyses, and Detections

have energy resolution. Moreover, table 3.2 lists the present status of some specific supernova neutrino detectors as well as the proposed projects.

In our analysis later on, especially in chapter 6 and 7, we will use detector models of Super Kamiokande, LVD, and KamLAND due to the fact that the way they collect data are in some sense analogous, which is counting the number of neutrino events in a given time bin. Meanwhile, to search for CCSNe in IceCube experiment, the collaboration treats the data in a different way, by observing a collective rise of the event rates in all photomultipliers, on top of the dark noise when there is a possible astrophysical low-energy neutrinos [63]. Thus for the moment, we will not include IceCube in our work.

TABLE 3.1: Summary of different neutrino detectors (taken from [61, 62]).

Detector type	Material	Energy	Time	Pointing	Flavor
Scintillator	C, H	y	y	n	$\bar{\nu}_e$
Water Cherenkov	H ₂ O	y	y	y	$\bar{\nu}_e$
Heavy water	D ₂ O	NC: n CC: y	y y	n y	All $\nu_e, \bar{\nu}_e$
Long string water Cherenkov	H ₂ O	n	y	n	$\bar{\nu}_e$
Liquid argon	Ar	y	y	y	ν_e
High Z /neutron	Pb, Fe	y	y	n	All
Radio-chemical	³⁷ Cl, ¹²⁷ I, ⁷¹ Ga	n	n	n	ν_e

TABLE 3.2: Specific SN neutrino detectors and some proposed projects (taken from [61, 62]).

Detector	Type	Mass (kton)	Location	# of events @8.5 kpc	Status
Super-K	H ₂ O Cher.	22.5	Japan	7,000	Running
SNO	H ₂ O D ₂ O	1.4 1	Canada	300	Running
LVD	Scint.	1	Italy	200	Running
IceCube	Long string	$M_{\text{eff}} \sim 0.4 \text{ pmt}^{-1}$ (Amanda)	Antarctica		Running
Baksan	Scint.	0.33	Russia	50	Running
KamLAND	Scint.	1	Japan	350	Running
Borexino	Scint.	0.15	Italy	130	Running
Hyper-K	H ₂ O Cher.	440	Japan	$\sim 2 \times 10^5$	Proposed
JUNO	Scint.	20	China	$\sim 7,000$	Proposed
DUNE	Liquid Ar	40	USA	$\sim 1,200$	Proposed

Analysis to hunt CCSNe by Super-Kamiokande

Super-Kamiokande (Super-K) is a 50-kton water Cherenkov detector, which is the successor of Kamiokande detector. It is 1,000-m (2,700 m.w.e.¹) deep underground with the fiducial mass of 22.5 ktons. This detector is able to collect $\sim 10,000$ events (9,000 without neutrino oscillation) when a CCSN happens in ~ 10 kpc away from earth. In this subsection, we will discuss the search of CCSNe by Super-Kamiokande in its offline analysis [64] that is basically re-analysing the old Super-K data and give overviews of the possible strategies to find CCSNe inside Super-K data, as well as the real-time online analysis strategy [65] for possible future CCSN detection.

Offline

In 2007, the Super-Kamiokande collaboration published its analysis from data collected in 1996-2001 (called SKI) and in 2002-2005 (SKII) [64]. No detection has been observed during those periods. The general flowchart analysis

¹meter water equivalent

can be described as:

1. Time-series data from SK consists of events mostly due to background and some perhaps due to astrophysical neutrinos. These events are also characterized by their energies. Then, it is possible to scan the event times in the data set by using a sliding time-window. A cluster is defined as the number of events in a certain time window. The events inside each cluster must pass a certain energy threshold: 6.5 MeV for SKI and 7 MeV for SKII [64]. The number of events in a cluster is called multiplicity, m .
2. Checking each cluster collected whether it is due to real event or background by using certain parameters/cuts that will be explained in the following.

Background events are the result of accidental coincidences of uncorrelated low energy events. There are two dominant time-correlated background: the flasher of photo multiplier tubes (PMTs) acting as the source of light and the spallation product of radioactive isotopes made via interactions between energetic cosmic ray (CR) muons and oxygen nuclei.

The collaboration argued that those background sources should produce events with a characteristic that the reconstructed event vertices tend to be **spatially concentrated** in the *physical volume of the detector*. Meanwhile, a real CCSN should generate **spatially uniform** neutrino events in the detector volume. Thus, to distinguish the astrophysical events from background events, it is introduced a new parameter to constrain the event spatial distribution (R_{mean}),

$$R_{\text{mean}} = \frac{\sum_{i=1}^{m-1} \sum_{j=i+1}^m |\vec{r}_i - \vec{r}_j|}{{}_m C_2}, \quad (3.1)$$

where $|\vec{r}_i - \vec{r}_j|$ is the spatial distance of i -event to j -event and ${}_m C_2$ is the number of unique combination. A real supernova neutrino burst will produce a cluster in the detector with a large value of R_{mean} comparing with the background cluster. Figure 3.1 is the expected R_{mean} distribution generated by Monte Carlo for several multiplicity values. Looking at the figure, the R_{mean} value from a

real astrophysical signal is expected to be around 1800 cm for every multiplicity m , while the sigma distribution depends on m . Therefore, the authors in [64] decided that,

$$\begin{aligned}
 R_{\text{mean}}(m = 2) &\geq 750 \text{ cm} \\
 &\vee \\
 R_{\text{mean}}(m > 2) &\geq 1000 \text{ cm}.
 \end{aligned}
 \tag{3.2}$$

The *raw*² efficiencies will be 94%, 96%, 99%, and 100% for that criteria.

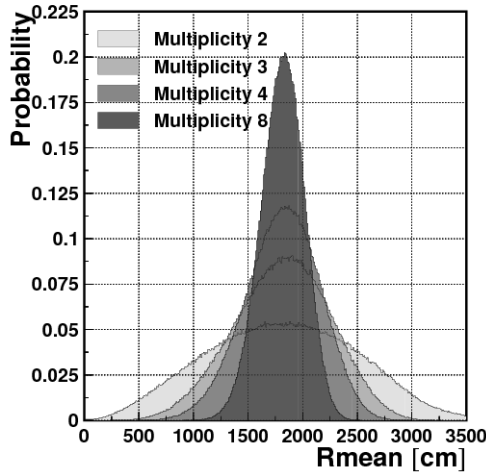


FIGURE 3.1: R_{mean} distribution generated by Monte Carlo for multiplicity=2,3,4, and 8. Figure is taken from [64].

In this offline analysis, there are 3 different searches:

1. Distant CCSN search up to the horizon edge such as to M31 galaxy,
2. Low energy threshold search,
3. Neutronization burst search of CCSNe.

These three searches use different time windows, multiplicity thresholds, as well as other additional criteria.

²We will call this efficiency as *raw* efficiency since at this point, there is no discussion of significance yet. This is different from the usual term used in gravitational wave community, where the efficiency is the total efficiency after imposing the significance threshold.

If a core-collapse supernova happens in M31 (Andromeda) galaxy, the detector expected multiplicity for SK detector $m \sim 2$ in a window of 20 seconds. Thus, the distant SN search has multiplicity threshold $m \geq 2$. However, a multiplicity threshold of $m > 2$ will give a lot of background. To tackle this problem, an energy threshold is chosen so as to maximize the value of $\frac{[\text{Detection Probability}]}{\sqrt{\text{Number of chance coincidences}}}$. The energy threshold adopted becomes higher than the previous threshold, which is now 17 MeV [64], that will give the single event rate of 0.762 events/day for SKI and 1.03 events/day of SKII.

In the low energy threshold, there are various time windows set in the data: 0.5, 2, and 10 seconds, while maintaining the low energy threshold that is set in the beginning: 6.5 MeV for SKI and 7 MeV for SKII. This takes into account that from core-collapse SN1987A (subsection 3.1), the average energy estimated by Kamiokande-II is 7.5 MeV, while by IMB it is 11.1 MeV and $\langle E_{\bar{\nu}_e} \rangle \sim 16$ MeV. This criteria still gives a lot of background. To reduce the background further, 3 additional criteria on the multiplicity values are introduced:

1. $m \geq [3 \text{ events}]/[0.5 \text{ second}]$,
2. $m \geq [4 \text{ events}]/[2 \text{ second}]$,
3. $m \geq [8 \text{ events}]/[10 \text{ second}]$.

If a cluster satisfies more than one criteria, the largest multiplicity will be taken. If a cluster also satisfies equation 3.2, all events within ± 20 seconds around the cluster are checked so as to get as many as possible the events from a possible CCSN.

Another analysis is the neutronization burst search. This is to investigate the short-lived neutronization burst of a SN: $e^- + p \rightarrow \nu_e + n$, happening in a period of < 10 ms. This neutronization burst will be observed by SK detector with multiplicity between 1 and 6 from a 10-kpc SN. Even if there is *no explosion* from this collapsing object (like for the formation of a blackhole³),

³The simulation for failed-supernovae (core-collapse forming a blackhole without explosion) can be seen in [66].

there could still be the neutronization burst. Thus, the windows are set to be 1, 10, and 100 milliseconds with a common multiplicity threshold equal to 2.

The collaboration decided to use the same sample as the previous SKI data for solar neutrino analysis with 5 MeV energy threshold since the recoil electrons from neutrino-electron scattering⁴ have lower energy. On the other hand, for SKII, they maintain the threshold of 7 MeV [64]. A lot of background will be present due to low multiplicity threshold, even after R_{mean} cut. Moreover, the recoil electron will have practically the same direction as the incident neutrinos. Thus, the neutrino events coming from a SN should have roughly the same reconstructed direction⁵. A new variable is introduced for this purpose, namely $Sumdir$,

$$Sumdir = \frac{|\sum_{i=1}^M \vec{dir}_i|}{M}, \quad (3.3)$$

where \vec{dir}_i is the reconstructed direction vector of events in a cluster of M multiplicity. $Sumdir$ will be towards 1 if the cluster is due to a SN. The threshold for $Sumdir$ is chosen to be ≥ 0.75 , which is the point at which the ratio between the probability of simulated Monte Carlo supernovae and the probability of simulated random direction events is equal to 1 (see figure 3.2). In this way, the *raw* efficiency is $\sim 84\%$.

Moreover, there is a relation between the number of observed clusters and the expected background,

$$N_{\text{bg}} = \sum_{i=\text{start}}^{\text{stop}} \sum_{j=M_{\text{thr}}}^{\infty} R_i T_i \frac{e^{-R_i \Delta T} [R_i \Delta T]^{j-1}}{(j-1)!}, \quad (3.4)$$

where M_{thr} is the multiplicity threshold, R_i and T_i are the single event rate and the total livetime respectively, inside the data taking period (max 24 hours data chunk) due to the fact that event rate of very low energy (<6 MeV) events depends on the detector running condition in each chunk. Moreover ΔT is

⁴ $\nu_e + e^- \rightarrow \nu_e + e^-$, the dominant reaction in this case.

⁵It is important to note that only the elastic scattering events give us the directional information, while events from IBD are quasi-isotropic.

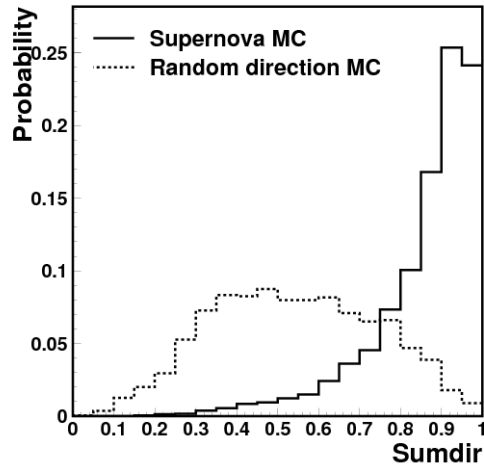


FIGURE 3.2: The distribution of *Sumdir*. Figure is taken from [64].

the time window (20 seconds). Equation 3.4, then, can be used to see whether our cumulative clusters are consistent with pure Poisson background or not. To give some idea of this offline analysis it has been plotted the *raw* detection probability as a function of distance in figure 3.3 for the distant burst search and low-energy threshold search. The probability of the distant supernova search till M31 is still 0.07, while the probability of the lower-energy threshold search declines quicker to be practically 0.0 at 780 kpc.

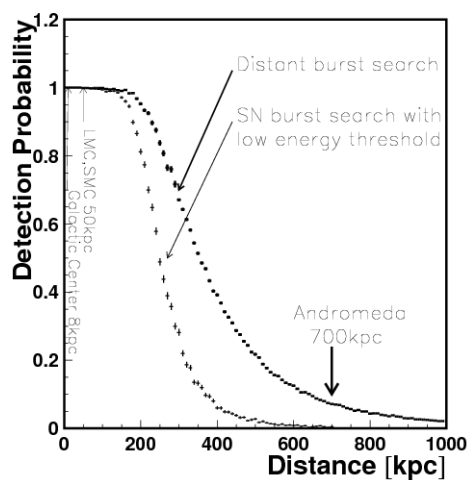


FIGURE 3.3: The detection probability as a function of distance for distant burst search and low energy threshold search. Figure is taken from [64].

Online

Besides the offline analysis, the fast alert (online/realtime) analysis has also been constructed by Super-Kamiokande collaboration [65], published in 2016, without any observed astrophysical detection. This online analysis basically has stronger cuts than the offline analysis in the previous section. For performance evaluations, the paper uses Monte Carlo simulation of 3000 ensembles of 10-kpc SNe from Geant3 software⁶ and the energy threshold for the analysis is 7 MeV.

The bin is constructed as a 20-second window opened backward from each event found and the number of events N_{cluster} is counted. In this case, N_{cluster} is slightly different from the multiplicity quantity since the bins is constructed differently: rather than making a fixed window bin in the beginning and then counting the number of events inside that bin, in this current case, the bin is open backward starting from an event is found.

Then, a variable D is computed as a parameter to explain the spatial distribution of events in a cluster; instead of R_{mean} in the offline analysis. D characterises the vertex distribution of a cluster of events and it has a value: $D \in \{0, 1, 2, 3\} \equiv \{\text{point, line, plane, volume}\}$. This is determined by comparing χ^2 values obtained from the lengths of the major and the minor axes corresponding to eigenvalues of the correlation matrix of the vertex distribution. The 3×3 correlation matrix can be written as

$$\langle (\chi_i - \langle \chi_i \rangle)(\chi_j - \langle \chi_j \rangle) \rangle = \begin{pmatrix} \langle (\chi_1 - \langle \chi_1 \rangle)(\chi_1 - \langle \chi_1 \rangle) \rangle & \langle (\chi_1 - \langle \chi_1 \rangle)(\chi_2 - \langle \chi_2 \rangle) \rangle & \cdots \\ \vdots & \ddots & \vdots \\ \vdots & \cdots & \langle (\chi_3 - \langle \chi_3 \rangle)(\chi_3 - \langle \chi_3 \rangle) \rangle \end{pmatrix} \quad (3.5)$$

⁶Geant3 software explanation can be found in more detail in [67].

where $i, j \in \{1, 2, 3\}$. Then, it is constructed,

$$\chi^2 = \sum_{n=1}^{N_{\text{cluster}}} |\vec{d}_n - \vec{d}(\vec{s})|^2, \quad (3.6)$$

where \vec{d}_n is the n -th event vertex position, $\vec{d}(\vec{s})$ is the position closest to \vec{d}_n either point, line, etc., and \vec{s} determines the geometry.

The three eigenvalues λ_i ($i \in \{1, 2, 3\}$ and $\lambda_1 \leq \lambda_2 \leq \lambda_3$) are used to construct the minimum of χ^2 that are $(\lambda_1 + \lambda_2 + \lambda_3)/3$, $(\lambda_1 + \lambda_2)/2$, and λ_1 (point-, line-, and plane-like) under a condition: $\partial\chi^2/\partial\vec{s} = 0$. In case of a real SN, the vertex distribution should be uniform in SK detector volume and thus $D = 3$. While for the background, $D = 2, 1$, or 0 . Thus, the conditions to have an on-line ‘‘golden’’ warning are when $N_{\text{cluster}} \geq 60$ and $D = 3$. A golden warning will be world-widely announced within one hour. This threshold is such that SN *raw* efficiency is 100% in LMC [~ 50 kpc] (under the models and simulations done for the paper).

Meanwhile, when $N_{\text{cluster}} < 60$, no golden warning is generated. However, there is another threshold called ‘‘normal’’ warning where the conditions are $N_{\text{cluster}} \geq 25$ & $D = 3$. This warning is for the experts only and to SNEWS (section 4.1). This has raw efficiency of 100% in SMC [~ 60 kpc].

There is also a lower threshold called a ‘‘silent’’ warning, requiring ≥ 13 events in 10 seconds. This makes a few warnings per day from spallation events. These silent warnings are used only for monitoring the system operation and detector condition, which are not used as the fast alert. The raw detection efficiency for without neutrino oscillation, normal hierarchy oscillation, and inverted hierarchy oscillation as well as the average number of background per 10-second bin can be seen in figure 3.4a, 3.4b, 3.4c, and 3.4d.

The paper also estimates the FAP of recovered injections by combining randomly the silent warnings to get a combined golden-like cluster. This will give the probability to have golden (normal) warning by chance. It is estimated the probability to have golden (normal) -like warning by accident is

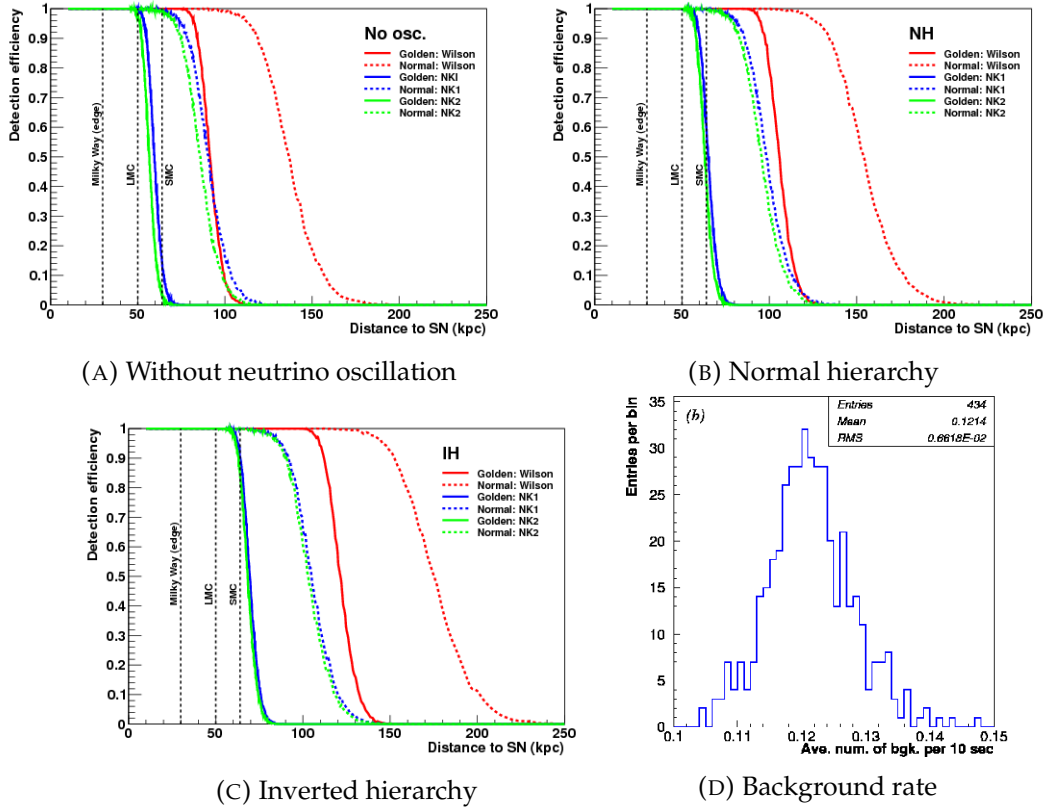


FIGURE 3.4: The raw efficiency of the method with no oscillation 3.4a, normal hierarchy 3.4b, and inverted hierarchy 3.4c as well as the background rate per 10 seconds of SK detector 3.4d. Figure is taken from [65].

1.3×10^{-11} (2.4×10^{-9}). If we calculate the significance by the normal distribution, they are actually 6.77σ and 5.97σ . Those probabilities are translated as rates to be one per 9×10^7 years for a golden warning and one per 4.7×10^5 years for a normal warning.

In addition, the paper also presents the possibility to determine SN direction by maximum-likelihood method. This determination depends on the interaction (inverse-beta decay⁷, electron elastic scattering of anti-electron neutrinos⁸, other elastic scatterings⁹, charged-current interactions on oxygen¹⁰), the measured electron energy, the number of events, i -th event electron energy, and i -th event direction.

⁷IBD, $\bar{\nu}_e p$.

⁸ES, $\bar{\nu}_e e$.

⁹ES, νe .

¹⁰ $\nu^{16}O$.

Analysis to hunt CCSNe by LVD

LVD is a scintillator-type detector with the mass of 1 kton. It has been running and taking data for several decades. In 2014, LVD collaboration released their analysis of 21-year data to search for neutrino bursts coming from CCSNe without any detection of CCSNe, and the result has been presented in [68]. The detector is sensitive to neutrino bursts from gravitational collapses with the detection horizon of up to the edge of the Galaxy. It is a counting analysis with the event energy sensitivity range of $10 \text{ MeV} \leq E_{\text{event}} \leq 100 \text{ MeV}$. The time series data consisting of events is then passed to several steps of data cuts in order to reduce the background. Then, the data is binned with time window Δt . The width of this Δt is varied up to 100 s in step of 100 ms. The number of events inside the bin is then counted and it is called multiplicity. This multiplicity is compared with the Poisson probability whether it is consistent with the background. More detail of the analysis can be found in [68].

Signals

On 24 February 1987, neutrino signals from core-collapse supernova was discovered by several detectors: Kamiokande II detector [21], IMB (Irvine-Michigan Brookhaven) water Cherenkov detector [22], as well as Baksan scintillation telescope [23]. The progenitor of this SN1987A is Sanduleak -69° 202a, considered as a blue supergiant star with a magnitude of 12 and the progenitor mass $M_p \sim 15M_{\odot}$ [69]. It is located on the neighborhood of the Tarantula Nebula in LMC with a distance $D \approx 50 \text{ kpc}$ away from us. The neutrino events of SN1987A captured by Kamiokande-II and IMB detector in terms of energy can be seen in figure 3.5.

The observation of SN1987A was guided by a preceding optical sighting of the SN. This trigger motivated the search of archived neutrino data in the constrained time scale to perform the search. This detection is the first and the only core-collapse supernova, up to now, in nearby galaxy ever detected

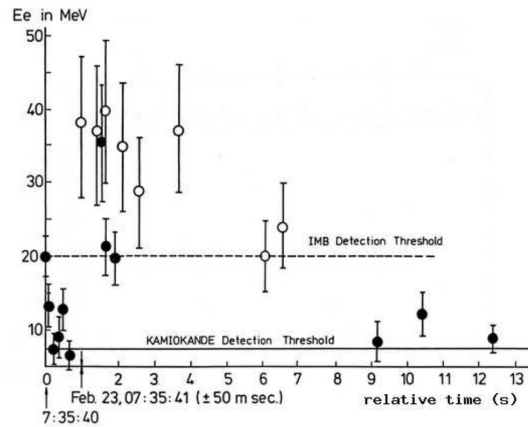


FIGURE 3.5: The neutrino energy events as a function of time captured by Kamiokande-II (closed circles) and IMB (open circles) produced by SN1987A. Figure is taken from [70].

via low energy neutrinos. While we are waiting for the next core-collapse supernovae, it is imperative to improve our capability to detect them in terms of detection efficiency and horizon.

3.2 The Gravitational Wave Channel

The first indirect detection of gravitational waves comes from the discovery of binary pulsars called PSR1913+16 [71]. This finding was awarded a Nobel prize in physics in 1993: “for the discovery of a new type of pulsar, a discovery that has opened up new possibilities for the study of gravitation” [72]. The discovery paper [71] says that the binary pulsars can be a good test for general relativity theory. Indeed, it has been proven that the orbit of the pulsars are shrinking due to the gravitational radiation, which is in agreement with general relativity. The comparison between the pulsar orbital decay versus the expected general relativity calculation can be seen in figure 3.6. This is the first indirect confirmation of gravitational waves [73]. In the following sections, we will describe the efforts of international collaborations pushing for the gravitational wave detectors starting from the bar detectors up to the Michelson-like interferometers.

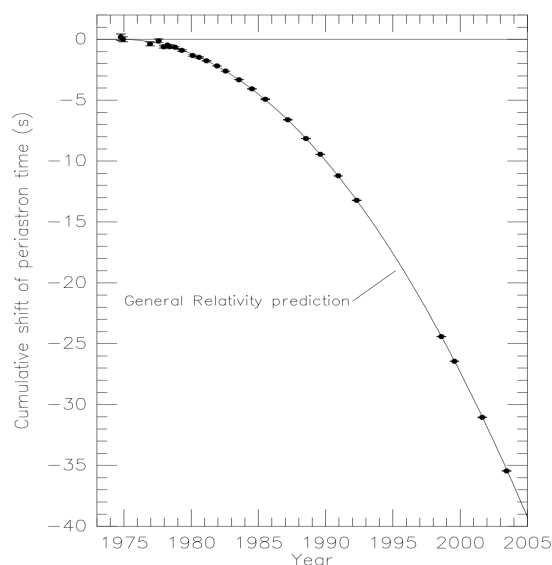


FIGURE 3.6: The orbital decay of PSR1913+16. The data points are the observed change of the epoch of periastron, while the parabola illustrates the expected change due to the emission of GWs according to general relativity. Figure is taken from [73].

GW Detectors

The bar detectors (resonant mass antennas) were the first kind of gravitational wave detectors aiming in observing high frequency¹¹ ($\sim 800 - 1000$ Hz) gravitational wave bursts. There were several detectors built around the world such as AURIGA (Padua, Italy), NAUTILUS [75] (Rome, Italy), EXPLORER (CERN, Switzerland), etc. Figure 3.7 shows the inside of Nautilus detector. In fact, in 1970s, Joseph Weber claimed to have seen a direct gravitational wave signal, though later on other test results show that it was noise. The first direct detection of gravitational waves was actually in 2015 done by two-LIGO interferometric detectors [76].

Starting in around 1994, the constructions of the new type of gravitational wave detectors began in several different places: two LIGO detectors [76] in Hanford and Livingston, USA, as well as a Virgo detector in Cascina, Italy. In the present day, those three detectors are working together in a network to hunt GWs. The aerial pictures of those detectors can be seen in figure 3.8. This type of GW detectors is basically the Michelson-like interferometer with

¹¹As an example here is the AURIGA sensitivity in 2004 [74].



FIGURE 3.7: Nautilus gravitational wave bar detector. Figure is taken from [77].

Fabry-Perot cavity. The arm length of LIGO detectors is about 4 km while the Virgo detector is about 3 km. The scheme of this detector can be seen in figure 3.9. Moreover, there is actually another interferometer in Germany which is GEO600 [78], having an arm length of 600 m, that is being used as Astrowatch project¹². This GEO600 is also working together with LIGO-Virgo. Besides, there are also ongoing projects to make the interferometers in several other places such as KAGRA in Japan [79] that will join the LIGO-Virgo detector network soon in 2020, as well as IndIGO (LIGO India) [80] which is under construction.

An interferometric ground-based detector basically follows its basic principle as a Michelson interferometer. When the gravitational wave signals pass through a detector, the test masses (mirrors) in the detector will not have fixed distances. In our case, we can assume that in figure 3.9, WI-WE and NI-NE as y-axis and x-axis. The distances of WI-WE and of NI-NE arm will oscillate, which basically follow equation B.7 and figure B.1.

A laser is used to measure the distances of both arms. The laser light is shot towards a beam splitter (BS) in figure 3.9 which divides the light into two coherent beams and each beam goes to each Fabry-Perot arm cavity (WI-WE and NI-NE). A Fabry-Perot cavity consists of two parallel mirrors trapping the beam and in figure 3.9, they are at the end of both cavities (WE and NE). There are two beams from two arms and they are trapped inside these arms. The

¹²This project permits GEO600 stays online to wait for the possible astrophysical events, while LIGO-Virgo detectors undergo an upgrade.

Chapter 3. Detectors, Analyses, and Detections



(A) LIGO Livingston, Louisiana, USA. Figure is taken from [81].



(B) LIGO Hanford, Washington, USA. Figure is taken from [82].



(C) Virgo, Cascina, Italy. Figure is taken from [83].

FIGURE 3.8: Gravitational wave interferometer detectors around the world.

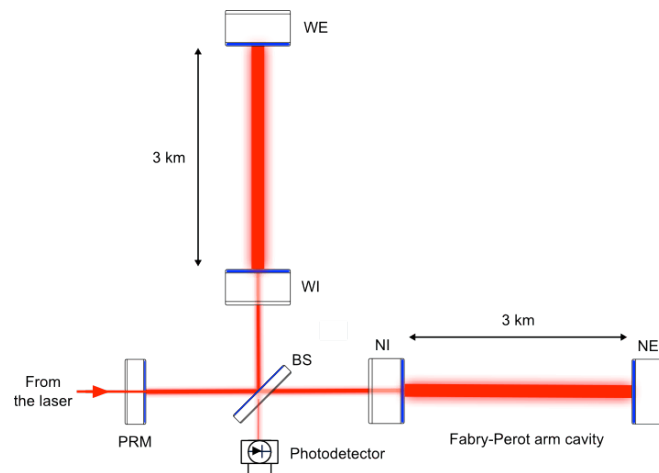


FIGURE 3.9: The scheme of a gravitational wave interferometer. Figure is taken from [84].

beams travel back and forth for multiple times until the beams from both arms escape and recombine at BS. In these two arms, there are perfectly reflecting mirrors in WE and NE, and partial reflecting mirrors in WI and NI in the

figure.

Part of the recombined beam goes toward a photodetector and another part goes back to the laser and thus the power recycling mirror PRM is used to reflect back this beam to the Fabry-Perot cavity. The photodetector will then measure the intensity of the beam. The change in distance of each cavity is translated as a phase difference. When there is a gravitational wave signal, this phase difference will change accordingly and it is recorded to be analysed further. A thorough explanation of this detector type can be seen such as in [24].

Gravitational Wave Burst Pipeline

There are many independent analysis pipelines to detect gravitational waves such as `pyCBC` [85], `X-Pipeline` [86], as well as `coherentWaveBurst` [87–91]. Here, we will discuss the generic burst pipeline called `coherentWaveBurst` (`cWB`), which was the pipeline giving the online alert for the first GW signal (GW150914 [92]). Moreover, this pipeline could also be useful to detect any burst signals since it is generic without needing any template¹³ of GWs, especially for our purpose, which is the GW signal from CCSNe.

The general idea of time-frequency transform is basically to transform time-series data to a time-frequency representation. Time-frequency representation enables us to point out “at what time” a signal happens and with which frequency. Knowing the time and frequency simultaneously is crucial for GW burst analysis. One example of these transforms is wavelet. Wavelet transform (WT) can be considered as a generalization of Fourier transform. Comparing with Windowed Fourier Transform (WFT): wavelet has a constant *relative* frequency resolution.

¹³This is in fact different from matched filtering technique that needs a bunch of GW templates.

Chapter 3. Detectors, Analyses, and Detections

In a mathematical notation, a general time-frequency transform can be written as,

$$s(x) \mapsto S(a, b) = \int_{-\infty}^{\infty} \overline{\psi_{ab}(x)} s(x) dx, \quad (3.7)$$

where, for the case of WFT (or Gabor transform), the basis function $\psi_{ab}(x) = e^{ix/a} \psi(x - b)$, while for WT, $\psi_{ab}(x) = \frac{1}{\sqrt{a}} \psi\left(\frac{x-b}{a}\right)$. The basis function ψ in this case is called mother wavelet (or window function in case of WFT). In addition, a is related to the characteristic frequency ($[\frac{1}{a}] = [\text{Hz}]$) and b is the time translation \rightarrow the “position” of time in the time-series data. Thus, a and b give us the frequency and time resolution (width) of the basis. The basis function $\psi_{ab}(x)$ can be seen more clearly in figure 3.10.

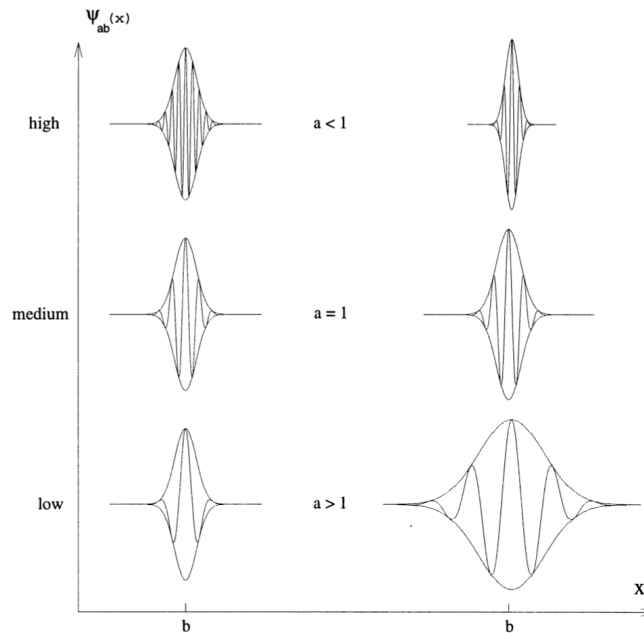


FIGURE 3.10: $\psi_{ab}(x)$ for WFT (left) and WT (right). Figure is taken from [93].

For a given a and b value, a crosscorrelation between the basis and a time-series data chunk is calculated. If the basis and the data chunk are matched, the crosscorrelation value will be high in the time-frequency map and that crosscorrelation value points to the time and frequency (range) of a possible “signal¹⁴”. The time-frequency representation (map) will have the form of

¹⁴whether this signal is due to real astrophysical signal or just a noise.

figure 3.11 and each tile will have a colorcode representing the value of the crosscorrelation.

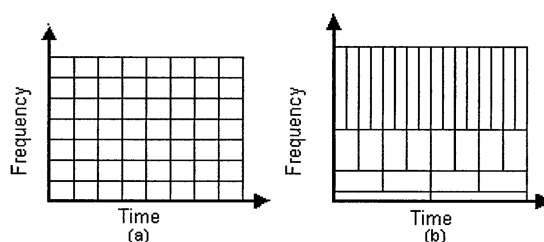


FIGURE 3.11: WFT (left) and WT (right). Figure is taken from [94].

The c_{WB} method in the beginning of its development [87–89] combines all data streams from different detectors into one coherent statistic, with wavelet transform, constructed in the framework of the constrained maximum likelihood analysis. The detection is based on the maximum likelihood ratio statistic representing the total signal-to-noise ratio of the GW signal detected in the network. Moreover, other coherent statistics can be constructed to distinguish genuine GW signals from the noise (environmental and instrumental artifacts). In addition, the source coordinates of the GW waveforms can also be determined.

In the upgraded version of c_{WB} , it used the fast Wilson-Daubechies time-frequency transform combined with the Meyer wavelet [90, 91] (Wilson-Daubechies-Meyer, WDM). There are several main advantages for this WDM transform comparing with the wavelet such as the low computational cost, spectral leakage control, flexible structure of the frequency sub-bands, and the existence of the analytic time-delay filters, which are important for localization of the gravitational-wave sources in the sky.

Efficiency of GW Analysis for CCSNe

Currently, the LIGO and Virgo detectors have been upgraded to an advanced stage. The spectral strain sensitivity $\sqrt{S_n(f)}[\text{Hz}^{-1/2}]$ (see cf. chapter 7 in [24]) of the advanced LIGO and advanced Virgo detectors can be seen in figure 3.12. This value is basically the noise level of the detectors and thus,

it means that the GW detectors are basically able to find GW signal with h_+ and h_\times amplitude (chapter 2) of the order of 10^{-23} in the most sensitive detector band from between 100 and 300 Hz. From this point, if we can build some signal waveforms with the information of h_+ , h_\times , and other parameters explained in chapter 2, it is possible to study the search efficiency of detectors by injecting those waveforms in the detector analysis and count how many injections are observed.

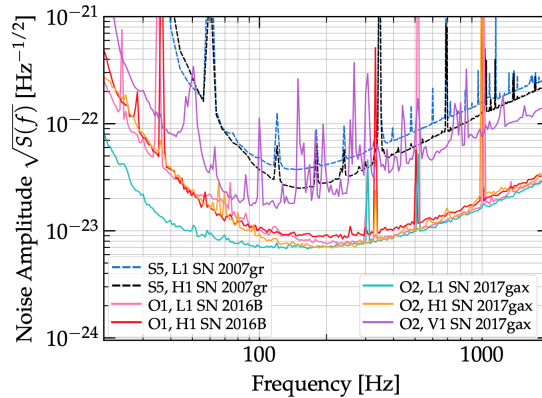


FIGURE 3.12: Noise spectral densities of the LIGO and Virgo detectors. O1 and O2 are the upgraded advanced LIGO and advanced Virgo detector sensitivities in their “observing runs” with several GW detections. Figure is taken from [95].

In fact, there have been some studies on the efficiency of *targeted* GW searches from CCSNe using several pipelines such as reference [53] (theoretical study) and [95] (real electromagnetically triggered observations) by multi-messenger techniques. They use the information of times and sky positions of observed CCSNe by other means like neutrino and electromagnetic triggers. They both are not all-sky blind search that we want to push on working. However, their results give us some insights that the efficiency that we can expect for the GW all-sky CCSN search will basically not exceed the targeted search efficiency.

The result in reference [53] uses X-Pipeline to make a study of GW search from CCSNe up to ~ 5 Mpc using the realistic noise from Advanced LIGO and Advanced Virgo sensitivity for 2015, 2017, and 2019 with hypothetical CCSNe in Milky Way, Large Magellanic Cloud, and M31, and M82 galaxy.

The paper considers two options,

1. CCSN search within 50 kpc with sky position and timing localisation information from neutrinos. At close source distances, they hope to detect GWs from CCSNe in current numerical simulation scenarios. Here, they search GW counterparts with the time window of $[-10, 50]$ seconds about the time of the theoretically neutrino triggered signal.
2. Distant CCSN search with sky position and timing localisation information from EM observations. At distances greater than (50-100) kpc, indeed, they do not expect to detect GWs from the multidimensional CCSN simulation scenarios. Instead, they consider more extreme, phenomenological models, which may be unlikely to occur, but have not yet been constrained observationally. For the time windows, they use several values for different progenitors, which could be as large as $[-50, 24]$ hours.

From those options, they manage to predict the efficiency of GW search from CCSNe. For the close distance scenario, they use different models (convection & SASI vs rotating collapse) and directions (towards galactic center vs LMC) and they can predict the efficiency curves as a function of distance. This efficiency curves can be seen in figure 3.13. Moreover, they also predict the efficiency curves for the extreme scenario in figure 3.14.

In the most recent study done by [95], instead of using X-Pipeline, they use `cWB` to find GW bursts from CCSNe. Moreover, they search the possible GW signals by using times and locations from electromagnetically triggered CCSNe from real observations within ~ 20 Mpc distance range. They selected five CCSNe, four of which are type-II CCSNe (SN 2015as, SN 2016B, SN 2016X, SN 2017eaw) and one is type-Ib/c CCSN (SN 2017gax), without finding of any GW signals associated with them. They use numerical simulations, phenomenological models, as well as *ad-hoc* sine-Gaussian waveforms on their study. Here, since they do targeted searches from the actual SN observations, for

Chapter 3. Detectors, Analyses, and Detections

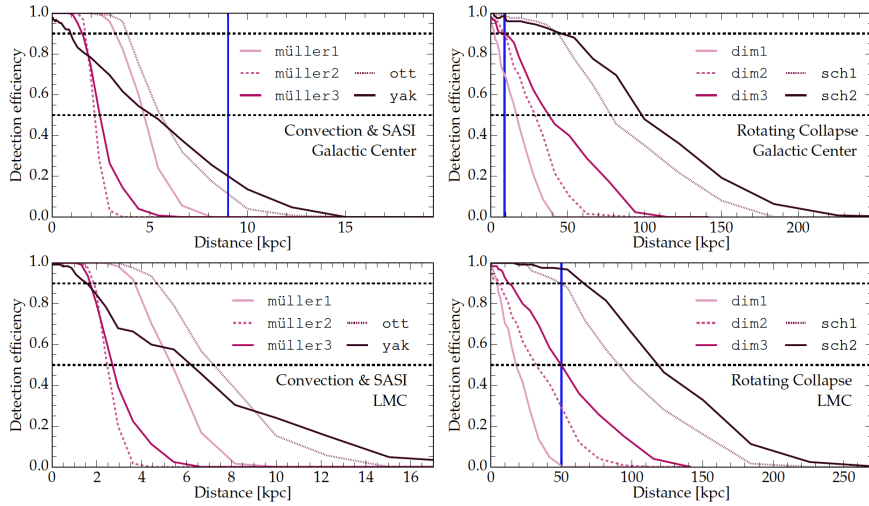


FIGURE 3.13: The detection efficiency curves as a function of distance for the numerical waveforms. Figure is taken from [53].

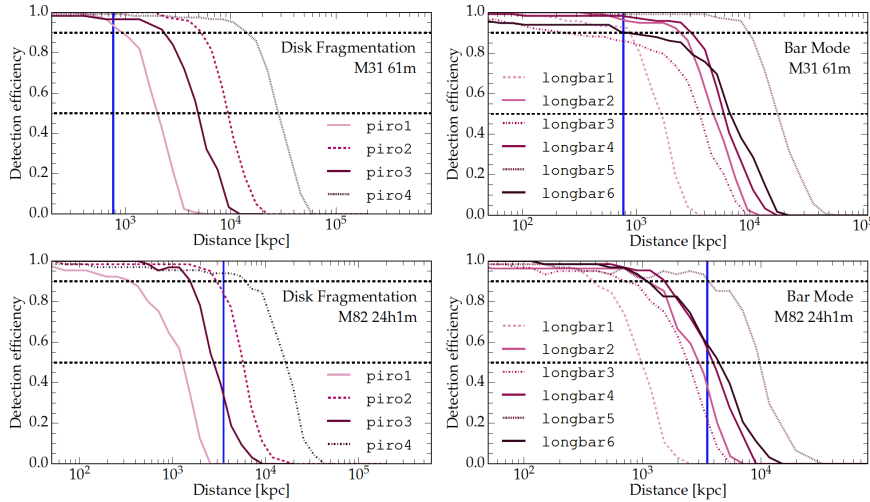


FIGURE 3.14: The detection efficiency curves as a function of distance for the extreme waveforms. Figure is taken from [53].

each SN the time window is chosen depending on the quality of the multi-band photometry, the determination of the host galaxy, and the type of CCSN. All in all, their possible GW signals are consistent with noise indeed the FAPs (false-alarm-probability¹⁵) of the possible signals are exactly in the noise curve (figure 3.15).

The efficiency curve of the study from [95] can be seen in figure 3.16. The curve is for different families of waveforms considered in their study with

¹⁵which is basically the significance value. This quantity will be discussed more in section 5.

Chapter 3. Detectors, Analyses, and Detections

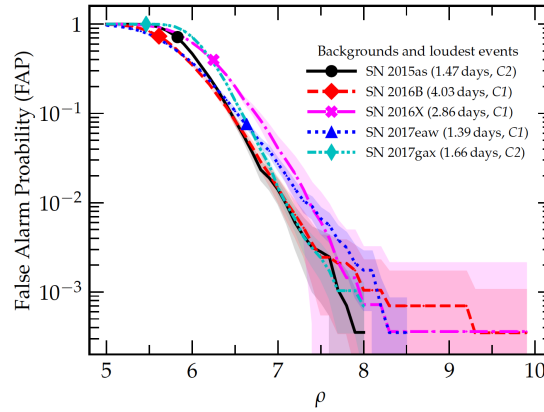


FIGURE 3.15: The FAP (false-alarm-probability) curve as a function of distance for the extreme waveforms. Figure is taken from [95].

the position and time using the information of SN 2017eaw. They also put an *ad-hoc* sine-Gaussian waveforms to study the h_{RSS} (related to the GW energy).

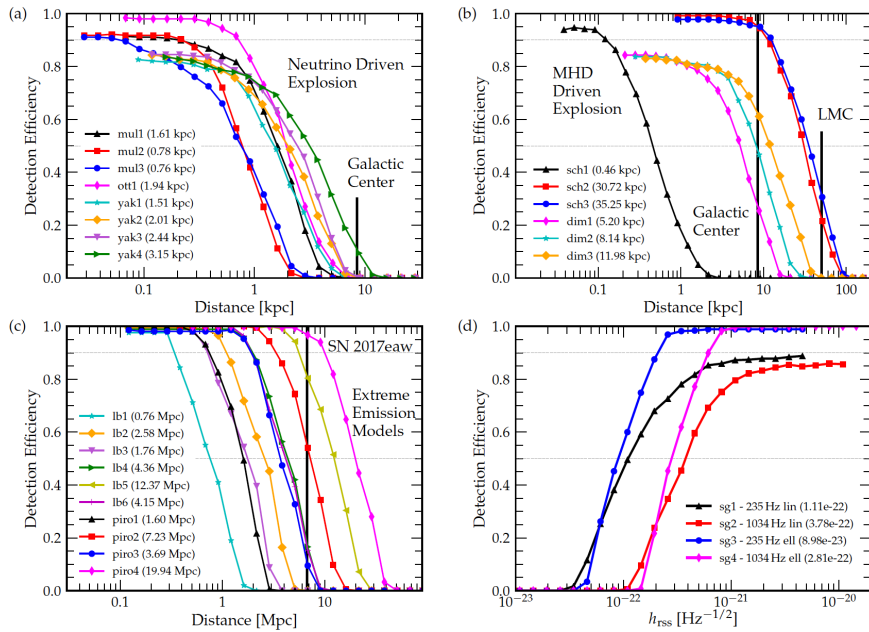


FIGURE 3.16: The efficiency curve as a function of distance for different waveforms. Panel (a), (b), and (c) show the efficiency using 3 different families of waveforms for the position and time reference of SN 2017eaw with the 50% detection efficiency distances are in parentheses. Meanwhile, panel (d) is for the *ad-hoc* sine-Gaussian waveforms as a function of h_{RSS} , instead, and with the 50% detection efficiency h_{RSS} are in parentheses. Figure is taken from [95].

3.3 GW Observations by LIGO-Virgo Collaboration

There have been several GW detections up to now with the advanced LIGO and advanced Virgo detectors in their first (O1), second (O2) and third (O3) observing periods. In this section, we will discuss several examples of these detections. We will start from the discussion of the first GW detection, GW150914 [92] from binary blackhole merger by two the advanced LIGO detectors¹⁶ [76]. Later on, we will also speak about the triple-detector gravitational wave detection [96] including the advanced Virgo detector [84] that can increase highly the sky position accuracy. In the end we will discuss the binary neutron star merger observation [97].

On September 14, 2015 at 09:50:45 UTC, the two LIGO detectors simultaneously observed a transient GW signal, named GW150914 [92], from the merger of two blackholes with the masses of $36_{-4}^{+5}M_{\odot}$ and $29_{-4}^{+4}M_{\odot}$ transforming to a single blackhole remnant of $62_{-4}^{+4}M_{\odot}$ and radiating $3.0_{-0.5}^{+0.5}M_{\odot}c^2$ of GWs. The binary was located in 410_{-180}^{+160} Mpc ($z = 0.09_{-0.04}^{+0.03}$). This is the first direct detection of GWs as well as the first direct detection of a binary blackhole merger. Moreover, this first GW detection marks a new observational window in astronomy. The signal has a frequency band increasing from 35 to 250 Hz peaking at 1.0×10^{-21} gravitational-wave strain. The waveform of this merger matched the general relativity prediction and more details can be seen in figure 3.17. The sky localization of this event under 90% credible region is 600 deg². In terms of electromagnetic observation, this sky localization is somewhat poor for the follow up electromagnetic observations. This poor localization is due to the fact that there were only two detectors observing this event since Virgo detector was upgrading the sensitivity.

There have some other GW detections during the several observing periods. An interesting example can be seen from the O2 run in which there has

¹⁶The two LIGO detectors are located in the USA: Hanford (H1), Washington and Livingston (L1), Louisiana. Moreover, there is also Virgo detector in Cascina, Italy. In the time of GW150914, the Virgo detector was not in observational mode. However, the next several GW detections, Virgo plays an important role especially in locating the signal together with the two LIGO detectors via triangulation method.

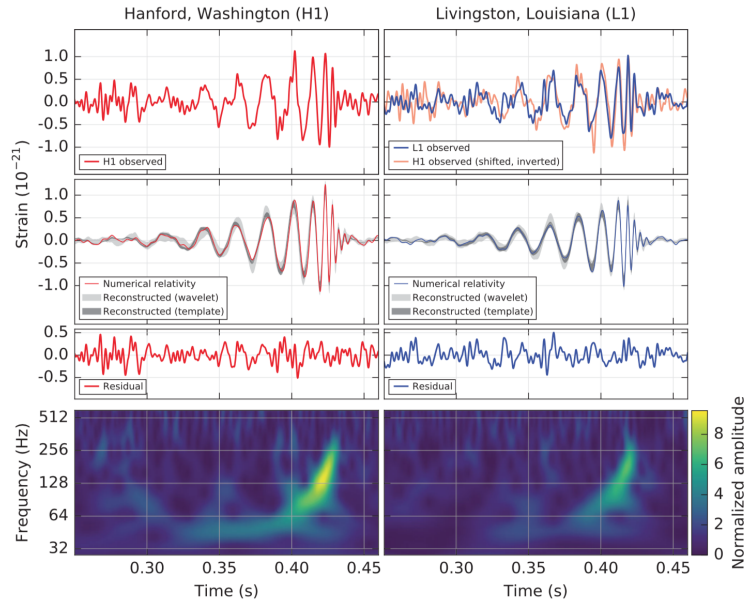


FIGURE 3.17: The details of GW150914: The top left is the H1 detector strain, the top right is the L1 and H1 detector strain together. The signal arrived first at L1 and $6.9^{+0.5}_{-0.4}$ ms later at H1. The second row is the numerical relativity waveform with the shades are the 90% credible regions of two independent waveform reconstructions. The third row is the residual. Bottom row is the time-frequency representation of the strain data. Figure is taken from [92].

been a triple-detector observation of GWs during which the French-Italian Virgo detector is also in observing mode. It was GW170814 that happens on August 14, 2017 at 10:30:43 UTC. This GW signal comes from a binary blackhole merger located in 540^{+130}_{-210} Mpc, corresponding to a redshift of $z = 0.11^{+0.03}_{-0.04}$. The progenitors have masses of $30.5^{+5.7}_{-3.0}M_{\odot}$ and $25.3^{+2.8}_{-4.2}M_{\odot}$. The most important feature in this GW signal is that, with three-detector network, the sky localization is improved to be 60 deg^2 comparing with 1160 deg^2 , thanks to the observation made by advanced Virgo detector. Moreover, we can also compare this sky localization resolution with the first GW signal (600 deg^2) involving only two detectors located in a closer distance. This triple-detector observation is promising for the follow-up observations involving multimessengers such as between electromagnetic waves and neutrinos.

Three online GW detectors give a promising multimessenger era due to the better sky-localization resolution. In fact, the first binary neutron star merger has been detected by multimessenger observations [97]: GW detection

Chapter 3. Detectors, Analyses, and Detections

by LIGO-Virgo detectors (named GW170817 [98]) and a gamma-ray detection by *Fermi* Gamma-ray Burst Monitor (named GRB 170817A [99]). There has been a ~ 1.7 second delay in these two independent channel detections from the same source. First, the GW signal arrived in GW detectors and ~ 1.7 seconds later a gamma-ray burst is detected by *Fermi* Gamma-ray Burst Monitor. Moreover, there were the subsequent follow-up observations done by electromagnetic wave observations: optical, X-ray, and radio telescopes [97]. In addition, no ultra-high-energy gamma-rays and no neutrino candidates found to be consistent with the source. This marks the start of GW multimessenger astronomy.

From this chapter, we will move on to explain the inter-collaboration multimessenger efforts as well as to discuss some multimessenger analysis reproductions in the next chapter.

Chapter 4

Multimessenger Efforts

We have reviewed our understanding of CCSNe in terms of astrophysical processes, detectability, and the detection efforts in the previous three chapters. Now, we move on to the actual core of this thesis starting from this chapter. In the following, we will begin discussing several multimessenger efforts done by inter-collaboration networks. Moreover, we will discuss also some examples of multimessenger analyses with their reproductions. We will also discuss the possibility to implement these analysis examples for our purpose.

4.1 SNEWS: Supernova Early Warning System

An effort to have a common working group with a data sharing of low energy neutrino detectors to hunt CCSNe has been pushed for several decades. This working group is called SNEWS (SuperNova Early Warning System¹) [62, 101]. Currently, there are seven neutrino experiments involving in this activity² [101]: Super-K (Japan) [37], LVD (Italy) [102], Ice Cube (South Pole) [41], KamLAND (Japan) [34], Borexino (Italy) [33], Daya Bay (China) [103], and HALO (Canada) [104]. No nearby core collapses have occurred since SNEWS started running, however, this system is ready for the next one.

¹The current stage of this working group is on the level of SNEWS2.0 where there are new things to be included such as the pre-supernova alert before the explosion as well as triangulation and pointing capability improvement. There has been a workshop [100] for this initiation.

²We can say in this case under SNEWS1.0, the first generation of the working group since 1998 and automated system since 2005.

The goal of this activity is to provide an early warning of a galactic supernova with the “three P’s”: prompt, pointing, and positive. The alert given to astronomical community must be as *prompt* as possible to catch the early stages of shock breakout, occurring typically in a matter of hours (or less) of a core collapse. It is aimed to publish within 5 minutes of an automated GOLD alert, while a SILVER alert involving human checking may be in a matter of 20 minutes. Moreover, there are two ways of *pointing* the source of burst: by information from each of detectors and by triangulation from several detectors.

In addition, the collaboration aims to give, indeed, *positive* alerts by using coincidence analysis of several data streams from different detectors. In this way, the significance can increase due to the crosscorrelation in the coincidence analysis, removing a lot of background, which is basically the same as saying to lower strongly the false alarm probability. Another additional “P” could be *privacy* in order to satisfy inter-experiment privacy needs.

4.2 $\text{GW}\nu$ Working Group: LIGO-Virgo, LVD, Borexino, IceCube, and KamLAND

An inter-collaboration working group [105] has been formed in 2013 that brought together neutrino and GW data analysts. The signatories were Borexino [33], IceCube [41], LVD [102], LIGO Scientific Collaboration [76] and Virgo Collaboration [84], as well as additionally in 2016 signed by KamLAND [34]. In fact, the result of coincidence search between LENs and GWs in Casentini’s thesis [47] is based on the data sharing under this MoU³ of the $\text{GW}\nu$ working group. Moreover, reference [106] also focuses on the multimessenger astronomy that can be performed for CCSNe, especially on the search and study from the GW channel. The basic idea for this working group is basically that neutrinos and gravitational waves are the only messengers with which the inner parts of CCSNe can be studied.

³Memorandum of Understanding.

As an exercise, the archival data of neutrino and GW detectors from 2005 to 2010 have been reanalysed with a conservative false alarm rate of 1/1000 years and with the coincidence window⁴ of 20 seconds between neutrino candidate and GW trigger. Up to now, this reanalysis has been done and presented in Casentini's thesis [47] with the data from LVD [102], Borexino [33], IceCube [41] and LIGO-Virgo collaborations [76, 84]. Unfortunately, there was no data exchange from KamLAND [34] at that time.

One of the main purposes of the working group is to initiate a close communication within the GW and neutrino communities. This is important especially for the possibility of the next nearby CCSN and the science that can be extrapolated from it. Such working group will be imperative in improving the sensitivity, live time coverage, as well as the significance of a detection by using joint data between the GW and neutrino network.

Currently, the working group is preparing on the renewal of the MoU and there is a good sign that some other experiments may join such as JUNO [35] and NO ν A [107].

4.3 Some Multimessenger Searches

In this period, we also have studied some examples of multimessenger efforts that have been discussed in the past. Particularly, we have studied the gravitational wave - gamma ray burst (GW-GRB) [108] and the gravitational wave - high energy neutrino (GW-HEN) [109, 110] multimessenger analysis in the basis of using the binomial test to jointly analyse data from different experiments.

⁴More detail will be explained in section 5.

4.3.1 Scheme of GW-GRB

GW-GRB

There were 39 GRBs in total during several LIGO science runs⁵ in the past, namely LIGO S2 (Feb-Apr 2003, 59 days), S3 (Oct 2003-Jan 2004, 70 days), and S4 (Feb-Mar 2005, 29 days). In those science run periods, the duty factor⁶ is of the order of $\sim 40.0\% - 80\%$. These 39 GRBs gave information about the times and locations that were used to search for their associated GW candidates.

The GW data, from all detectors in properly working conditions, are paired (H1-H2, H1-L, and H2-L) and chunked around the times of GRBs. Moreover, it is defined the *on-source* and *off-source* time segments (figure 4.1). The on-source time segment is used for searching a GW-GRB coincident candidate during the time of a single GRB, while the off-source time segment is used to estimate the background noise of GW data around the GRB time and give a statistical significance of the coincident candidate found in the on-source time segment (details in 4.3.1). Here, for each GRB time, a GW on-source time segment span from 120 s before and 60 s after a single GRB time. Meanwhile, an off-source time segment is ± 1.5 hours *surrounding* the on-source time segment. In addition, each of the on-source and off-source is binned in 25 ms and 100 ms bin-length.

The cross-correlation is then applied to find GW candidates associated with GRBs. The cross-correlation cc is defined as,

$$cc = \frac{\sum_{i=1}^m [s_1(i) - \mu_1][s_2(i) - \mu_2]}{\sqrt{\sum_{j=1}^m [s_1(j) - \mu_1]^2} \sqrt{\sum_{k=1}^m [s_2(k) - \mu_2]^2}} \quad (4.1)$$

where s_1 and s_2 are time series data segments to be correlated, μ_1 and μ_2 the corresponding means, m the number of samples for cross-correlation which is the bin length (either 25 ms or 100 ms) multiplied by the sampling rate of LIGO (16384 samples/s). Thus, the value of cc is in the range of $[-1, +1]$.

⁵This science run is the period when the detector(s) working in a proper condition to take data.

⁶The fraction of the data-taking time when each detector was in science mode [111].

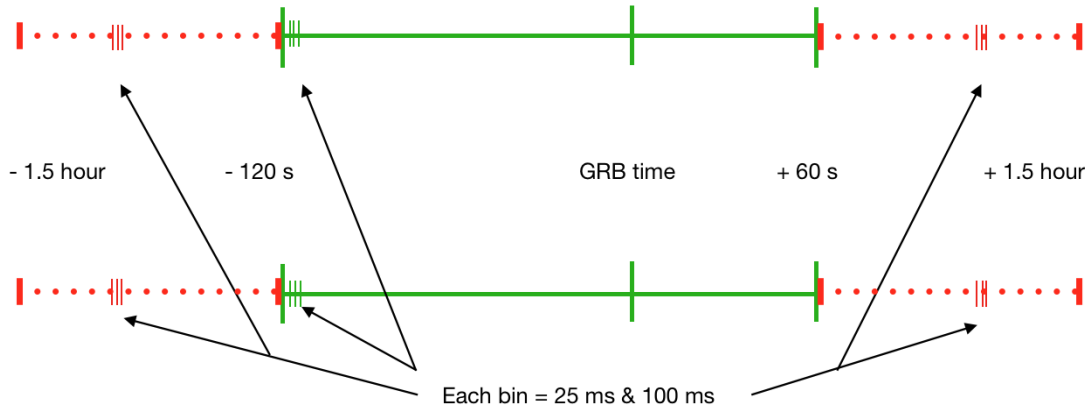


FIGURE 4.1: The on-source (green) and the off-source (red) time segment.

Each candidate which has the highest⁷ cross-correlation from each pair of on-source time segments is taken as a *candidate*. Moreover, for GRBs which have well-defined positions, the dedicated GW source is performed constraining the sky in the GRB position. Before calculating the cc , each pair of H1-L & H2-L time segments is shifted in time relative to each other by the corresponding time-of-flight delay. For those GRBs having *no well-defined positions*, *only* H1-H2 pair is analysed. The maximum time-of-flight delay is ± 10 ms for H1-L & H2-L, which is the same order as the putative signal durations, and thus, the time offset would have a significant effect on the calculation of cc [108].

Single-event Basis

To find a GW candidate associated with a GRB time, the authors of [108] apply the cc in equation 4.1 on the on-source time segments. Besides, they also assign a measure to give a statistical significance of each of the candidates for the single-event basis, which in this case is called p -value (false alarm probability). This is done by comparing the distribution of cc of the background around a candidate which is from the off-source segment (red colour in figure 4.1) with the cc of the candidate itself from the on-source segment for each

⁷For H1-L & H2-L the value of cross-correlation was taken as the absolute value to take into account the anti-correlated signal depending on GW (unknown) polarisation.

GRB time, each data pair (H1-H2, H1-L, H2-L), and for each value of bin-length (25 ms vs 100 ms). The assumption is that the off-source segment has similar characteristic and is a representative of the on-source background.

Each cc distribution in the off-source is built up by compiling the largest cc of each 180-second subsegment in an off-source segment. In addition, to get enough statistics for each cross-correlation distribution, time-shift is also done for the off-source segments of multiples of 180 seconds relative to each other and made sure that two 180-second subsegments are paired only once for each distribution.

The fraction of cc from the off-source analysis that are larger than the cc from the on-source analysis is calculated and this fraction is the false alarm probability (FAP) or simply, p -value, or can be said as the single-event-basis significance. By doing all the steps here, in the paper [108], in the end, there are in total 59 candidates⁸ for which 35 from H1-H2, 12 from H1-L, and 12 from H2-L, along with their p -values and none of the candidates is significant enough that has p -value smaller than 0.01.

Quantitative Analysis with Statistical Basis: the Binomial Test

GW signals can be very weak due to cosmological distances, thus having large p -values. Beside looking for GWs separately from each trigger⁹, it is useful to consider the detection of a GW signature associated with a sample of several triggers. In paper [108] for GW-GRB, the authors tried to find the GW signature by using binomial test and they showed there was no GW signature on their data.

In this work, we discuss the binomial test that has been used by [108–110], that is searching for the tail (the significant end) of distribution of a sample. Assuming null hypothesis, meaning that there is no interesting signal in our

⁸This number is larger than the number of GRBs (39) since for each GRB, it was possible to have up to three interferometer pairs (H1-H2, H1-L, and H2-L) passing the data quality cuts.

⁹The triggers can be GRBs and HENs as well as others.

data, the p -values that we get from data should be uniformly distributed between $[0 : 1]$. By using the binomial test to compare the p -value distribution with a simulated uniformly random distribution, we may be able to determine whether there is a GW signature in our data. The scheme for this binomial test can be seen in figure 4.2.

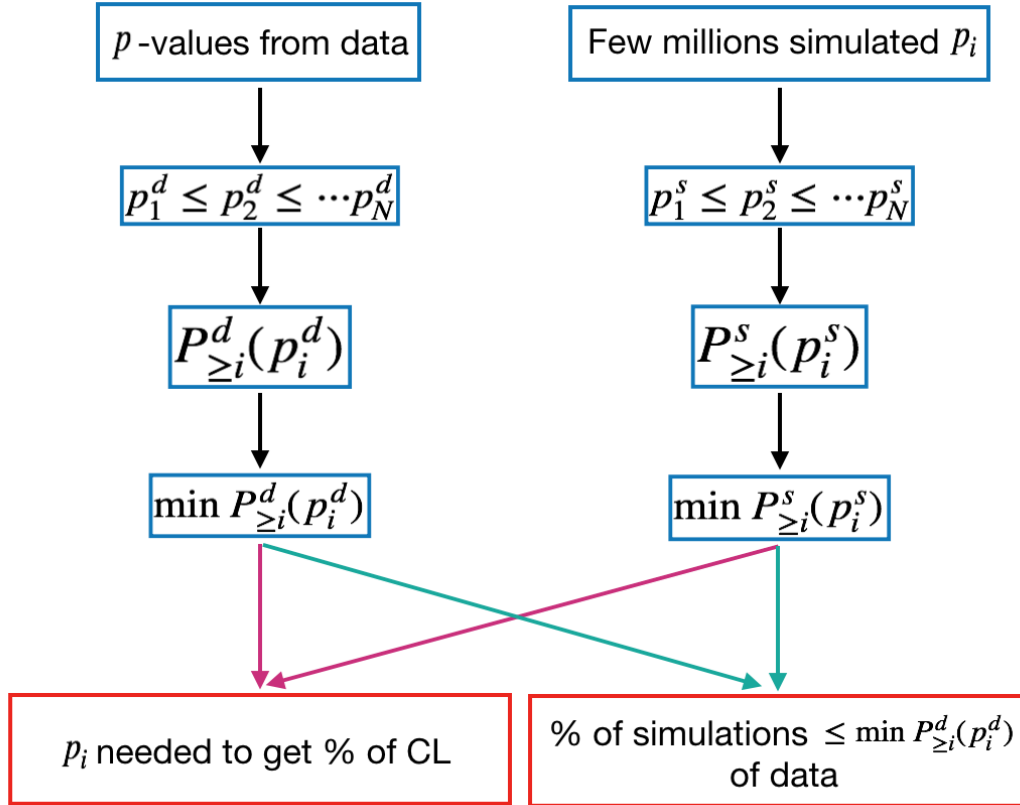


FIGURE 4.2: The scheme of binomial test in this work. The superscript d stands for data, while s stands for simulation.

First of all, to do the binomial test, the p -values of N candidates are sorted as,

$$p_1^d \leq p_2^d \leq \dots \leq p_N^d \quad (4.2)$$

and n of them¹⁰ are tested for the binomial test. For each of the p_i^d (in which the superscript d stands for 'data') with $i = 1, \dots, n$ (n being the tail to be tested), the 'upper'¹¹ cumulative binomial probability — the probability to get

¹⁰ $n \leq N$

¹¹complement

Chapter 4. Multimessenger Efforts

i or more candidates at least as significant as p_i^d — is computed as,

$$\begin{aligned}
 P_{\geq i}^d(p_i^d) &= P_i^d(p_i^d) + P_{i+1}^d(p_i^d) + P_{i+2}^d(p_i^d) + \cdots + P_N^d(p_i^d) \\
 &= 1 - [P_0^d(p_i^d) + P_1^d(p_i^d) + P_2^d(p_i^d) + \cdots + P_{i-1}^d(p_i^d)] \\
 &= \sum_{k=i}^N \frac{N!}{(N-k)!k!} (p_i^d)^k (1-p_i^d)^{(N-k)}
 \end{aligned} \tag{4.3}$$

where $P_i(p)$ is the binomial probability to get i successes in N trials,

$$P_i(p) = \frac{N!}{(N-i)!i!} p^i (1-p)^{(N-i)}, \tag{4.4}$$

where in paper [108], $N = 59$ candidates with $n = 15$ most significant candidates, which are $\sim 25\%$ of N .

After $P_{\geq i}^d(p_i^d)$ have been calculated for $i = 1, \dots, n$, the smallest $P_{\geq i}^d(p_i^d)$ is determined. This value is the most significant excess that is found in the tail of p -value distribution of the data. For paper [108], the smallest binomial probability is $P_{\geq 9}^d(p_9^d = 0.104) = 0.153$ for 25-ms binning and $P_{\geq 9}^d(p_9^d = 0.112) = 0.207$ for 100-ms binning, while in our work, the values are $P_{\geq 9}^d(p_9^d = 0.104) = 0.155$ & $P_{\geq 9}^d(p_9^d = 0.112) = 0.211$.

To determine what significance is of the smallest $P_{\geq i}^d(p_i^d)$ that is found, 1 million trials¹² of N -simulated p -values are formed under the assumption that background noise would produce p -values in a uniformly random distribution of $[0 : 1]$. After this 1 millions sets of N simulation have been made, all the steps for the binomial test are applied on each set and the minimum $P_{\geq i}^s(p_i^s)$ for each set is determined (in which $i = 1, \dots, n$). Here, the superscript s stands for “simulation”. Now, there are one million of the minimum $P_{\geq i}^s(p_i^s)$ from each set of 1 million trials and the fraction of them which are smaller than the smallest $P_{\geq i}^d(p_i^d)$ **from the observed data** is calculated. This

¹²the number of trials may depend on the significance that we want. For example 1000 trials should be more than enough for 1% significance, while ~ 1.67 million trials are the minimum to find $5\sigma (6 \times 10^{-7})$ significance ($1.67 \text{ million} \times (6 \times 10^{-7}) \approx 1 \Rightarrow$ one of the trial has a value as significant as 5σ). However, since in [108] used 1 million trials, the reproduction work uses the same number of trials.

fraction becomes the significance (confidence level, CL) of this statistical-basis analysis. In paper [108], the significance was 48% for 25-ms binning and 58% for 100-ms binning, while in the reproduction work, the values are 48.56% and 58.03%, respectively.

The statistical-basis significances in [108] for 25-ms and 100-ms of binning were very weak to be considered as GW signatures. Moreover, the exclusion region for $\sim 1\%$ CL can be estimated for $i = 1, \dots, n$ by the simulated p -values, meaning that searching for the 1% smallest $P_{\geq i}^s(p_i^s)$ of 1-million simulations and finding the associated p -value in order to get at least 1% CL. From paper [108], the distribution can be seen in figure 4.3 and the reproduction is in figure 4.4.

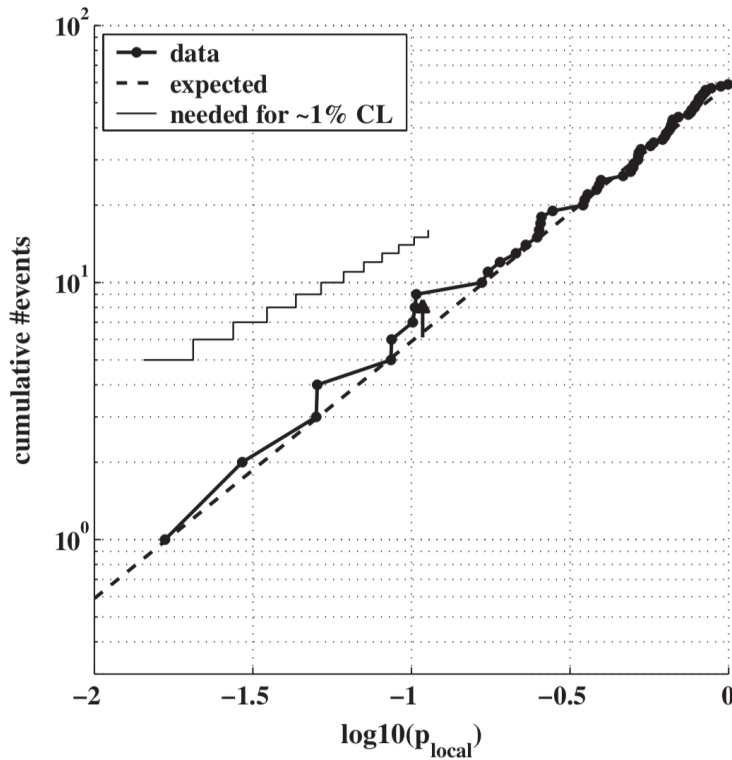


FIGURE 4.3: Cumulative events vs p_{local} . It consists of distribution of observed p -values (line-dots), the null hypothesis (dashed line) from 1 million simulations, and the $\sim 1\%$ CL (solid line) for which only $i = 5, \dots, 15$ are shown. This figure is taken from paper [108].

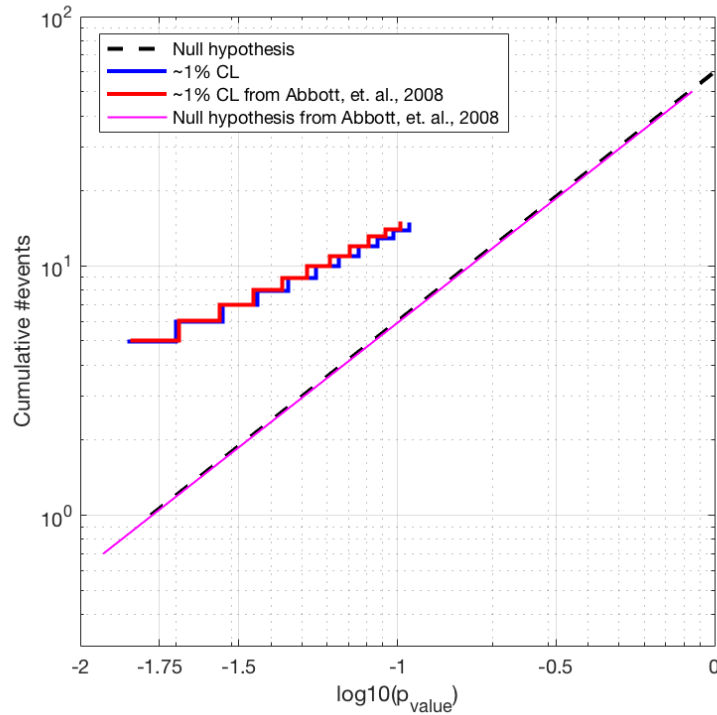


FIGURE 4.4: The reproduction of figure 4.3 with the null hypothesis (black-dashed line) from 1 million simulation, the $\sim 1\%$ CL exclusion region (blue line), and the estimation of the exclusion region (red line) & the null hypothesis (magenta line) of figure 4.3 taken by using [112].

4.3.2 GW-HEN Paper

GW-HEN

In the GW-HEN paper [109, 110], the steps of analysis by using binomial test were similar to the GW-GRB paper [108] explained in subsection 4.3.1, however, there were some technical difference in the data and the GW pipeline to produce candidates with their p -values. The data in those GW-HEN papers were from Antares¹³ high energy neutrino (HEN) data during the period January-September 2007 during which there was only 5-line configuration (see figure 4.5). That period was coincident with the fifth LIGO science run

¹³The Antares detector is aimed at detecting high-energy neutrinos. The detector is located at ~ 40 km off the coast of Toulon, France, and is operating on the sea bed at a depth of 2475 m, covering an area of about 0.1 km^2 . It consists of three-dimensional grid of photo-multiplier tubes (PMTs), used to measure the arrival time and position of Cherenkov photons induced by the passage of relativistic charged particles through the sea water. The illustration of the detector can be seen in figure 4.5. More detail about Antares can be seen in [113].

S5 and the first Virgo science run V1. There were 158 HEN while at least two GW detectors were in operation: 144 2-line¹⁴ events and 14 3-line events. In addition, the authors used X-Pipeline algorithm from [86] instead of cross-correlation of equation 4.1 to do the single-event basis-analysis (subsection 4.3.1) for acquiring the candidates and their corresponding p -values.

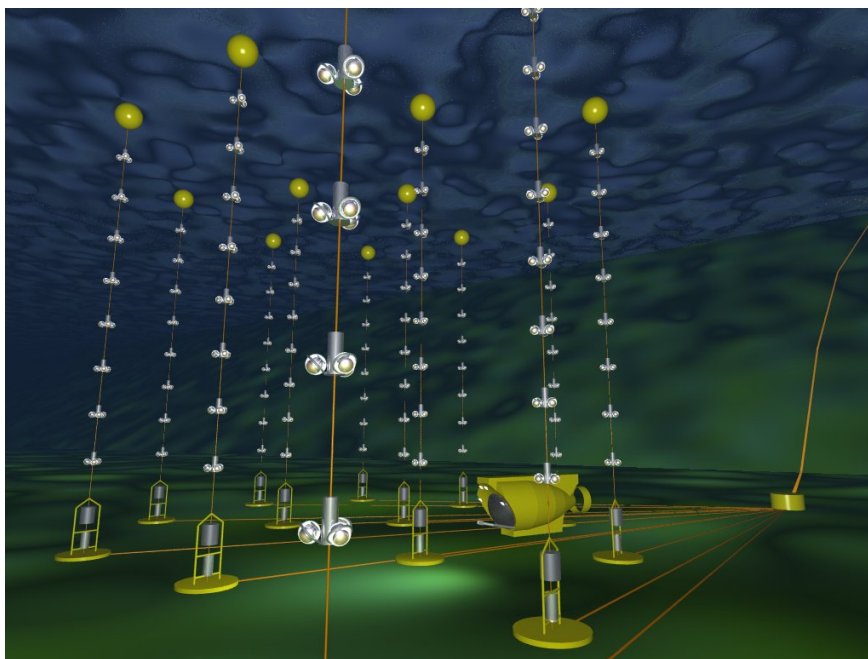


FIGURE 4.5: Cartoon of full run configuration of Antares. There are 12 lines and each consists of photodetectors to detect Cherenkov light from muons due to high-energy astrophysical neutrinos. During January-September 2007, only 5 lines were running. This figure is taken from [114].

The X-Pipeline algorithm processes GW data and yields GW candidates in time-frequency map¹⁵, moreover, the higher the frequency, the more computing power is needed. Besides, the possible GW sources discussed in cf. section 2 of [109] shows that the most likely detectable extragalactic signals are in the low-frequency band ($\lesssim 500$ Hz). Thus, with this consideration, the authors in [109, 110] processed GW data associated with all 158 HEN to search for low frequency (LF, 60-500 Hz) GW candidates and only 14 3-line events to search for high frequency (HF, 500-2000 Hz) GW candidates. Meanwhile, they

¹⁴Line here refers to the thread consisting of photodetectors like in figure 4.5.

¹⁵Each GW candidate is assigned with its characteristic time and frequency

defined on-source and off-source time segment like in subsection 4.3.1 as the input for *X-Pipeline* in which for a single HEN time, the on-source spanned from -496 s to $+496$ s, while the off-source spanned from -1.5 hours to $+1.5$ hours surrounding the on-source (see figure 4.6). This was to consider the models of GW and HEN emission from astrophysical sources.

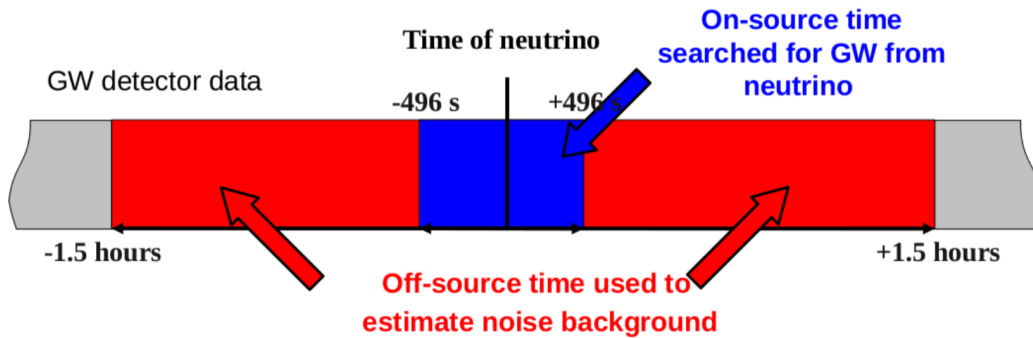


FIGURE 4.6: The on-source (blue) and the off-source (red) time segment. Figure is taken from [110].

With the steps from section 4.3.1 but with *X-Pipeline*, they got LF and HF candidates with their corresponding p -values. Only one of the candidates (only in LF) had p -value smaller than 0.01 to become a candidate event. However, that event occurred during a glitching period in V1 data. Thus, they concluded there was no GW burst signal associated with HEN during that period.

Beside the single-event basis, a quantitative analysis by binomial test to search for the GW signature from a sample of HENs had been done in those papers. Again, no GW signature was present in this quantitative analysis. The binomial test that they used was the same as in the discussion in subsection 4.3.1 but with $N = 158$ and $n = 15$ for LF and $N = 14$ and $n = 1$ for HF. The reproduction of their work can be done in more detail than GW-GRB, due to the more information¹⁶ we can acquire, and can be seen in figure 4.8 & 4.10.

¹⁶The authors of [109] provided some data in detail in a web [115] to construct c.f. figure 5 and 6 of their paper (figure 4.7 and 4.9 in this report).

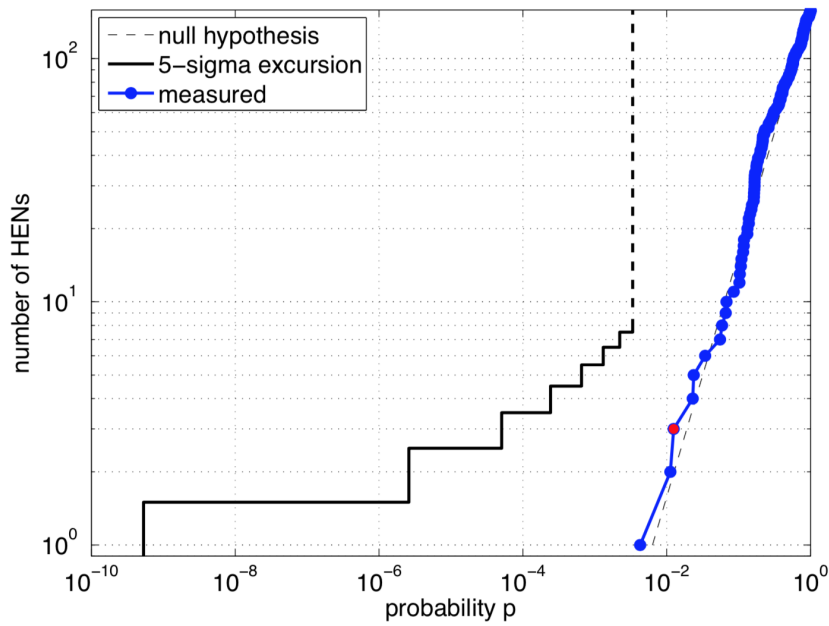


FIGURE 4.7: The distribution of observed p -values (blue-line-dots) for LF with most significant excess (red dot), null hypothesis (dashed line), and 5σ exclusion region (solid line). This is taken from paper [109].

The last important discussion is due to the fact that we made the simulation of uniformly distributed random number to get the simulated p -values, every time we run the simulation, the simulated p -values that we get are slightly different from the previous run, but the statistics are still the same. This is why we have slightly different points on figure 4.10 between the 5σ CL region from [109] and from our work. This applies also for all the exclusion region on figure 4.4 and 4.8.

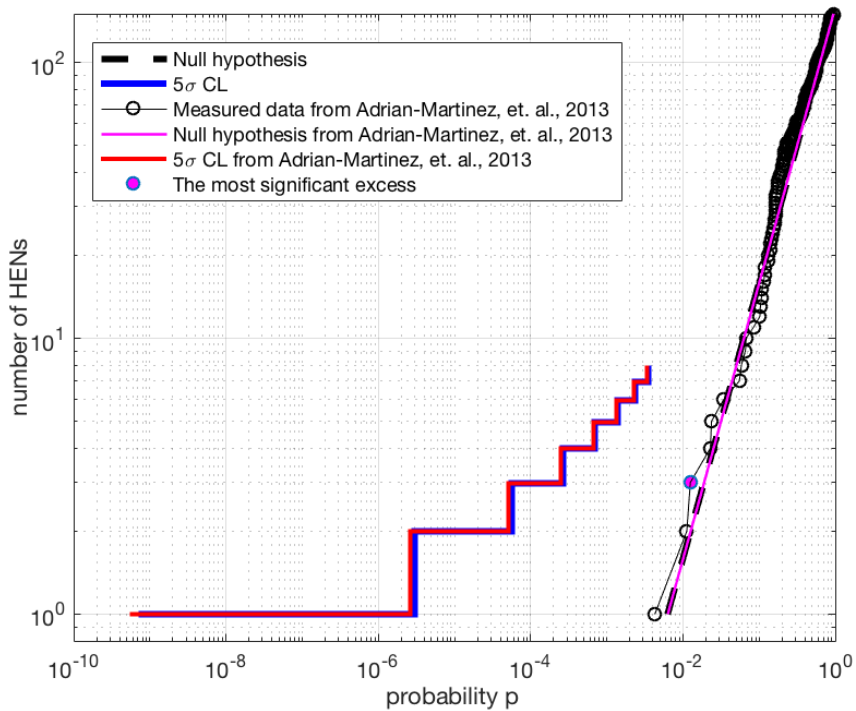


FIGURE 4.8: The reproduction of figure 4.7. This consists of null hypothesis (black-dashed line), 5σ exclusion region (blue line), and the data of figure 4.7 from [115]: observed p -values (black-line-circles), most significant excess (magenta dot), 5σ exclusion region (red line) & null hypothesis (magenta line).

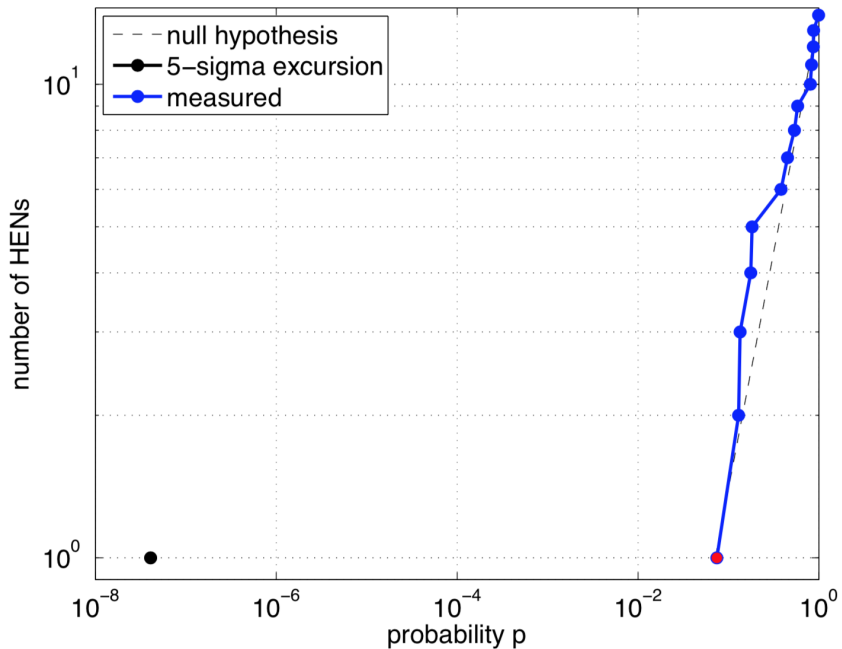


FIGURE 4.9: The distribution of observed p -values (blue-line-dots) for HF with most significant excess (red dot), null hypothesis (dashed line), and 5σ exclusion region (black dot). This is taken from paper [109].

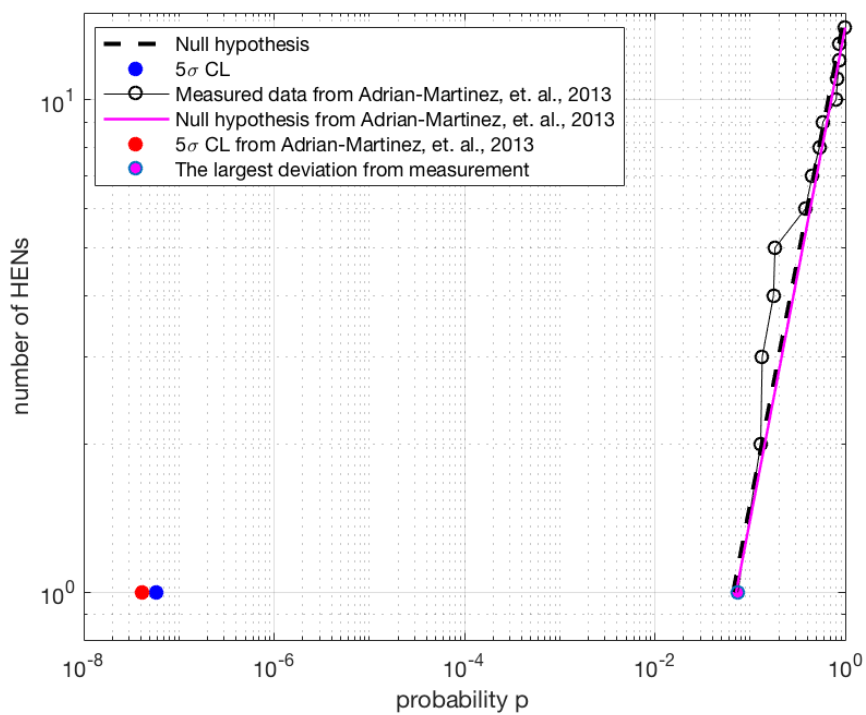


FIGURE 4.10: The reproduction of figure 4.9. This consists of null hypothesis (black-dashed line), 5 σ exclusion region (blue dot), and the data of figure 4.9 from [115]: observed p -values (black-line-circles), most significant excess (magenta dot), 5 σ exclusion region (red dot) & null hypothesis (magenta line).

4.4 The Prospect of Quantitative Analysis Application on GW-LEN Joint-analysis

The analysis that has been explained and reproduced in previous sections may be applied for our case, which is the GW-LEN joint-analysis. We need to mention that from each GRB or HEN previously, we do not assign any significance value. Meanwhile, the joint-analysis of GW-LEN that we aim will use both data coherently and determine whether there is (are) interesting candidate(s). The combination of data will increase the significance of a possible signal [116].

Thus, we do not go further from the previous example of multimessenger analysis because in our case, each LEN consists of its significance value (which is basically in the form of *false-alarm-rate*, see the next chapter), while in the binomial test, they do not precisely give each significance of the GRBs or HENs. Moreover, in LEN analysis, we will use a lot of triggers to combine and this may be not in a correct place to use the binomial test. Thus, in chapter 5, we will discuss the coincidence analysis method that we use for our LEN-GW analysis purposes.

Chapter 5

Coincidence Analysis

We have studied the inter-collaboration networks to hunt CCSNe as well as some multimessenger analysis examples. In this chapter, we will discuss how to combine data from several detectors to be as a network. This basically can be done by coincidence analysis. There are two ways of doing coincidence analysis which we will discuss.

5.1 Coincidence Analysis between Two Datasets

Coincidence analysis is used in several analysis pipelines, particularly in GW analysis, such as in the burst pipeline like `cWB` [87–91] discussed in subsection 3.2, `pyCBC` [117], `GstLAL` [118], etc. The aim of coincidence analysis is basically to suppress the background by cross-correlating n time-series data sets from n different detectors. Here we consider the case of calculating the coincidence between detectors which use the same statistics: like LIGO and Virgo for GW or LVD and KamLAND for low-energy neutrinos. In particular, we focus in the case of only two-detector data sets, but the extension to three or more will be basically analogous to the two-detector case. We use a notion called *cluster*¹ to mark a trigger in a time-series data set gathered by a detector/experiment.

¹The terminology of “cluster” for a trigger comes from the neutrino analysis that we will discuss in chapter 6.

Chapter 5. Coincidence Analysis

Two time-series data sets are correlated in time to find time coincidences of clusters from the two sets. A cluster in one data set is considered in coincidence with another cluster from the other data set if the time difference between them is less than a coincidence window w_c . Two coincident clusters from two different data sets are defined as a coincidence. We check all the coincidences in this case and we will say that they are the *0-lag coincidences*. These 0-lag coincidences are basically the *candidates of the real astrophysical bursts*.

For the analysis, we also need another quantity: the common observing time between two data sets in this coincidence analysis and we call this as *lifetime*. Each detector has its time period when the data are in the *good* state, depending on each experiment procedure, and then the common time in coincidence between these two periods is calculated and we define it as the *lifetime*.

It is possible that the candidates we find are due to some fluctuation in the detectors, therefore, we need to assign a significance value for each candidate. To estimate this value, there are two possible ways,

1. The time-shifting method: finding the accidental background coincidences by time-shifting a data set towards the other and comparing the statistics of the candidates with the statistics of the accidental coincidences. This is the standard method that is used in the GW analysis.
2. The product method: finding only the 0-lag coincidences and determining the significance of each candidate from the information of f^{im} (imitation frequency²/false-alarm-rate, FAR) of each cluster in a single detector.

A candidate then will have some parameters: joint-statistic (only for the time-shifting method), jointFAR, and a significance which is basically a *false-alarm-probability* (FAP) that will be described in the next subsections.

²The imitation frequency is basically the value of how often background coincidences mimic a candidate with the same or better statistic than the candidate. This will be discussed better in 6.

5.2 The Time-shifting Method

To do the time-shifting method and finally find the significance of each candidate, we need to have a common statistic among detectors. This could be done such as in neutrino-only network as well as GW-only network, but not GW- ν network. In other words, if we want to have GW- ν network analysis in this first-method way, we need to search for a common statistic between GW and neutrino data, which may be complicated to find.

For the network already having a common statistic, the joint-statistic of a candidate can be defined as follow,

$$\rho_{\text{joint}} \equiv \sqrt[n]{\prod_{i=1}^n \rho_i}, \quad (5.1)$$

where ρ_i is the statistic of each cluster in the i -th data set.

Then, the candidate's FAR can be estimated by time-shifting of one data set towards the other by a value (which we call it as "delay") much bigger than that of the coincident window w_c ; therefore, each coincidence found in this time-shifting is purely due to accidentally unphysical correlation (background). To populate better the background distribution, the time-shifting is done for N lags (time-shifts) in each direction, for which we set N to be as many as possible. However, as we will see later, there is a maximum number of shifts we can perform.

Each shift of this time-shifting method will be the multiple of some delay value plus some random number in order to avoid any correlation between different time shifts. So as to maintain the livetime for each time shift, we also do the "cyclic" coincidence when there is one part of data set that is out of common observing time due to this time-shifting. This part of outbound data set will be taken and shifted to the other end of the other data set. We do this for both time-shifting directions. Therefore, by doing this, the coincidence livetime is not reduced. To understand better this method, we can make a scheme of this *cyclic* time-shift which can be seen in figure 5.1a and 5.1b.

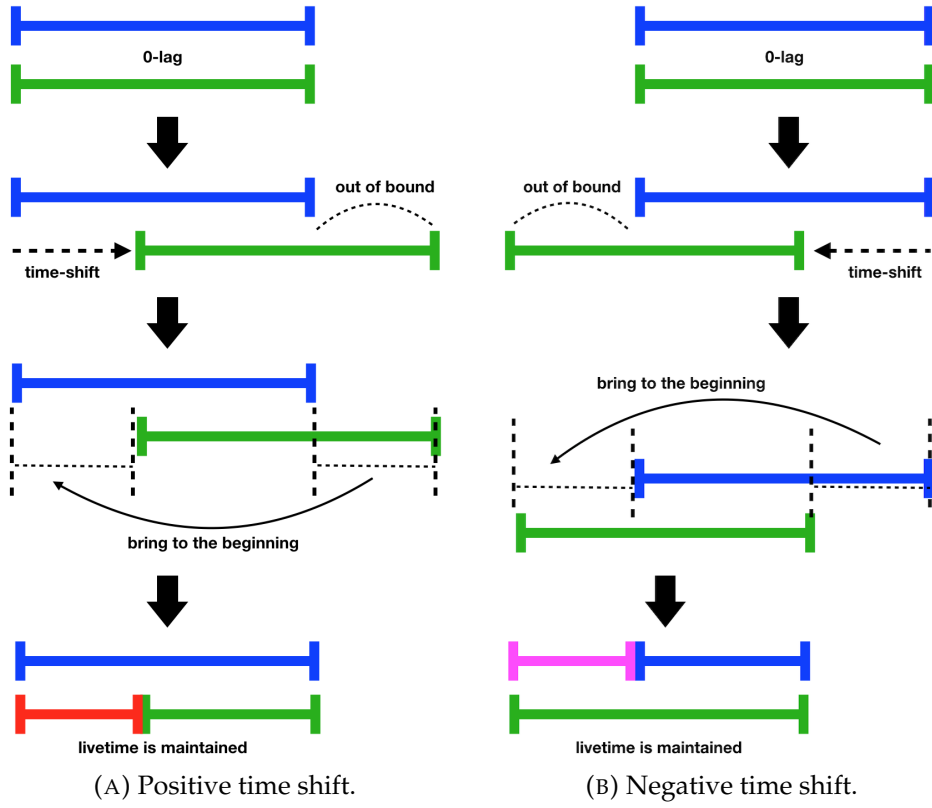


FIGURE 5.1: The scheme for cyclic coincidence analysis. The blue and green color represents the time-series data sets. When the green data set is out of bound like in the second row in Panel (A) due to time-shifting, that part of the green data set is taken and put to the beginning of the blue data set (red chunk), thus the livetime of both data sets will be constant for each shift. This works also for the other time-shift direction like in Panel (B).

After calculating the number of accidental coincidences (and their ρ_{joint}) from N time-shifts, we find the FAR by calculating the ratio between the cumulative accidental coincidences whose ρ_{joint} are larger or equal than the $\rho_{[\text{joint},0],i}$ of a 0-lag candidate,

$$\text{FAR}_i = \frac{[\text{number of candidates with } \rho_{\text{joint}} > \rho_{[\text{joint},0],i}]}{[\text{cumulative livetime of } N \text{ lags}]} \quad (5.2)$$

where i stands for the i -th 0-lag candidate that we are scrutinising. Then, the significance (FAP) can be defined as,

$$\text{FAP}_i = 1 - \exp(-\text{FAR}_i \times \text{livetime}_{0\text{lag}}), \quad (5.3)$$

Chapter 5. Coincidence Analysis

with the livetime of the 0-lag.

If we want a 5σ -level candidate, this means that we need to have $\text{FAP}_i \lesssim 5.7 \times 10^{-7}$, for which the i -th index here points to the 5σ candidate, and it means,

$$\text{FAR}_m \times \text{lifetime}_{0\text{lag}} \lesssim 5.7 \times 10^{-7}. \quad (5.4)$$

Moreover, given that for cyclic time-shift, the livetime of each shift is the same as the $\text{lifetime}_{0\text{lag}}$, moreover, the cumulative livetime after N shifts is simply $N \times \text{lifetime}_{0\text{lag}}$. The lowest FAR, therefore, that we can get is simply,

$$\text{FAR} = 1/[\text{cumulative livetime}] = \frac{1}{N \times \text{lifetime}_{0\text{lag}}}. \quad (5.5)$$

Combining equation 5.5 above together with equation 5.4 and 5.5, thus, we can understand the minimum shift N that we need to do is actually $N \gtrsim 1.75 \times 10^6$.

In this way, we should avoid that the time delay value in this applied time-shift method is equal to the total $\text{lifetime}_{0\text{lag}}$ after N -shifts, otherwise we are repeating shifts we already explored. This means, it is imperative that $\text{lifetime} \gtrsim \text{delay} \times N$.

For the neutrino network analysis, this livetime value may not be reasonable since we need to have the two neutrino detectors working in a quite long period of time in order for us to state a 5σ detection claim. However, this may not be the case for GW analysis since w_c between LIGO and Virgo is about 30 ms and thus the livetime needed is of the order of days³. Why is the w_c very different between the GW and neutrino analysis? This is because in GW analysis, the peak of signal can basically be traced and cross-correlated and the coincidence window is basically the time-of-fly of the GW detectors, with the maximum value is of the order of 30 ms (LIGO to Virgo detector). Meanwhile in neutrino analysis, a burst LEN signal from a CCSN may last up to around 20 seconds, thus, we cannot make the coincidence window less than of the order of 10 seconds. Let's suppose we choose our delay = 50 seconds to be

³The first GW event uses 16 days of livetime [92].

long enough comparing to w_c . This is translated to be that the livetime $\gtrsim 2.77$ years.

5.2.1 Comments on Estimating the Livetime and Expected (Poisson) Number of Coincidences

Poisson assumption of a distribution requires a constant rate. The rate of background from each data set is somewhat constant in a quite long period of time; moreover, each cluster from background should be uncorrelated with the other clusters. Therefore, when we do time-shifting, the accidental coincidences between the two set should simply follow Poisson distribution. Is this assumption satisfied?

Let's start for now with the case of 2 data sets: A and B , whose number of triggers are N_A and N_B and rates of background are r_A and r_B in [Hz]. Applying a coincidence window w_c , we find the rate of accidental background coincidences between A and B is equal to R , in the common livetime T_{ob} . Then, the expected accidental number of coincidences is $N_{acc} = R \times T_{ob}$. We want to find the expression of this R (or N_{acc}) in terms of all information that we have. If suppose we have 1 trigger, we understand that the probability of finding this trigger in time-coincident with at least 1 cluster in data set A within w_c , by taking the Poisson probability, can be written as,

$$P_{0;A}(w_c) = 1 - \exp(-\mu_A) \quad (5.6)$$

where $\mu_i = r_A \times w_c$. If the rate is small enough $r_A \ll 1/w_c$, equation 5.6 can therefore be written as,

$$P_{0;A}(w_c) \approx \mu_A = r_A \times w_c. \quad (5.7)$$

Chapter 5. Coincidence Analysis

Analogously, the probability of finding one trigger in time-coincident with at least 1 cluster in B within w_c is,

$$P_{0;B}(w_c) = r_B \times w_c. \quad (5.8)$$

We do the coincidence analysis between A and B with the joint rate R . Let us suppose that we have an infinitesimal chunk of common observation time (lifetime) as dt . The probability of 1 cluster in A inside this dt ,

$$dp_A = r_A \times dt, \quad (5.9)$$

analogously for B ,

$$dp_B = r_B \times dt, \quad (5.10)$$

From equation 5.7-5.10, we want to find the number of expected coincidences in an infinitesimal time dt . Thus, in this dt , the expected number of accidental coincidences dN_{acc} is expressed as,

$$\begin{aligned} dN_{\text{acc}} &= R \cdot dt = (dp_A) \times (P_{0;B}(w_c)) + (dp_B) \times (P_{0;A}(w_c)) \\ &= r_A dt \times r_B \times w_c + r_B dt \times r_A \times w_c \\ &= 2 \cdot r_A \cdot r_B \cdot w_c \cdot dt. \end{aligned} \quad (5.11)$$

Thus,

$$\begin{aligned} N_{\text{acc}} &= \int_0^{T_{\text{ob}}} R dt \\ &= 2 \cdot r_A \cdot r_B \cdot w_c \cdot T_{\text{ob}} \\ &= 2 \frac{N_A \cdot N_B \cdot w_c}{T_{\text{ob}}}. \end{aligned} \quad (5.12)$$

Chapter 5. Coincidence Analysis

Moreover, if we have 3 detector data sets (set C with its N_C and r_C), analogously, equation 5.11 becomes,

$$\begin{aligned}
 dN_{\text{acc}} &= R \cdot dt = (dp_A) \times (P_{0;B}(w_c)) \times (P_{0;C}(w_c)) \\
 &\quad + (dp_B) \times (P_{0;A}(w_c)) \times (P_{0;C}(w_c)) \\
 &\quad + (dp_C) \times (P_{0;A}(w_c)) \times (P_{0;B}(w_c)) \\
 &= r_A dt \times r_B \times r_C \times w_c^2 + r_B dt \times r_A \times r_C \times w_c^2 \\
 &\quad + r_C dt \times r_A \times r_B \times w_c^2 \\
 &= 3 \cdot r_A \cdot r_B \cdot r_C \cdot w_c^2 \cdot dt,
 \end{aligned} \tag{5.13}$$

and equation 5.12,

$$\begin{aligned}
 N_{\text{acc}} &= \int_0^{T_{\text{ob}}} R dt \\
 &= 3 \cdot r_A \cdot r_B \cdot r_C \cdot w_c^2 \cdot T_{\text{ob}} \\
 &= 3 \frac{N_A \cdot N_B \cdot N_C \cdot w_c^2}{T_{\text{ob}}^2}.
 \end{aligned} \tag{5.14}$$

In general,

$$N_{\text{acc}} = N_{\text{det}} \left[\prod_{i=1}^{N_{\text{det}}} N_i \right] \frac{w_c^{N_{\text{det}}-1}}{T_{\text{ob}}^{N_{\text{det}}-1}}. \tag{5.15}$$

To get the rate of accidental coincidences, we can simply divide equation 5.15 with T_{ob} to get the same expression as in cf. equation 1 in SNEWS paper [62],

$$R_{\text{acc}} = N_{\text{det}} \times w_c^{N_{\text{det}}-1} \left[\prod_{i=1}^{N_{\text{det}}} r_i \right], \tag{5.16}$$

where $r_i = N_i/T_{\text{ob}}$.

Since in this case we discuss only the two data set case, our N_{acc} becomes,

$$N_{\text{acc}} = 2 \times \frac{N_A \cdot N_B \cdot w_c}{T_{\text{ob}}}, \tag{5.17}$$

Chapter 5. Coincidence Analysis

and if our coincidence result is consistent with the background noise, our actual number of coincidences N_{real} should be in the range of,

$$\left(N_{\text{acc}} - \sqrt{N_{\text{acc}}}\right) \leq N_{\text{real}} \leq \left(N_{\text{acc}} + \sqrt{N_{\text{acc}}}\right), \quad (5.18)$$

in 1σ confidence interval⁴. This is for the test whether our number of 0-lag coincidences follows the Poisson distribution, meaning that whether it is due to background.

We assume the livetime for each shift is the same as $\text{livetime}_{0\text{lag}}$, for the 0-lag. Thus, for the total number of shifts N , the Poisson number of actual accidental coincidences can be averaged and its standard deviation can be calculated. Since it is commonly known, we can simply calculate the average as,

$$N_{\text{shift,acc}} = \frac{\sum_{i=1}^N N_{\text{shift},i}}{N}, \quad (5.19)$$

and the standard deviation as,

$$\text{std}(N_{\text{shift,acc}}) = \sqrt{\frac{1}{N-1} \sum_{i=1}^N |N_{\text{shift},i} - N_{\text{shift,acc}}|^2}. \quad (5.20)$$

Thus, we can also check whether the number of actual accidental coincidences $N_{\text{shift,real}}$ is inside 1σ interval,

$$\left(N_{\text{shift,acc}} - \sqrt{N_{\text{shift,acc}}}\right) \leq N_{\text{shift,real}} \leq \left(N_{\text{shift,acc}} + \sqrt{N_{\text{shift,acc}}}\right), \quad (5.21)$$

to confirm that our time-shift number of coincidences agrees with Poisson distribution as it should be when our assumption in the beginning says that the accidental coincidences should follow the Poisson distribution. Moreover, we can also compare the 0-lag (the N_{real} and N_{acc}) with the time-shift ($N_{\text{shift,real}}$ and $N_{\text{shift,acc}}$) whether they are consistent with the Poisson distribution.

⁴ 1σ interval for Poisson distribution is $N \pm \sqrt{N}$.

5.3 The Product Method

As we have argued before that the first method requires a common statistic in both data sets, the first method will not work for GW-neutrino coincidence analysis unless there is a possibility to find the common statistic. However, we need to notice that the analysis of GWs⁵ and the analysis of neutrinos⁶ are quite different and therefore, the common statistic may be quite tricky to find. Moreover, we need to remember as well that the coincidence window for neutrino analysis w_c is 10 seconds and this implies that to get 5σ candidate, two neutrino detectors must be working coherently in the order of 3 years and this could possibly be a problem. There is actually another possible way of finding a significance without using the time-shift. Let us call this as the second method and we simply need to use the f^{im} (or FAR) information from each detector when there is a coincidence [119].

The second method simply benefits from the information of f^{im} for each cluster from each data set and we don't need to have the common statistic. As long as two detectors can give its own FAR (or f^{im} in terms of neutrino analysis) and as long as the two data sets have a common observing time called livetime, then, we can calculate the joint FAR analogous to equation 5.14 and 5.15. Basically, we change r_A in equation 5.14 to be f_A^{im} and $N_{\text{acc}}/T_{\text{ob}}$ in this case is equivalent to the jointFAR. Let us suppose there are 3 data sets: a, b, c . When we have 1 trigger, we understand that the probability of finding this trigger in time-coincident with at least 1 trigger in data set a , data set b , and data set c respectively within w_c , by taking the Poisson probability, can be written as,

$$\begin{aligned}
 P_{0;a}(w_c) &= 1 - \exp(-\mu_a) \approx f_a^{\text{im}} \\
 P_{0;b}(w_c) &= 1 - \exp(-\mu_b) \approx f_b^{\text{im}}, \\
 P_{0;c}(w_c) &= 1 - \exp(-\mu_c) \approx f_c^{\text{im}},
 \end{aligned}
 \tag{5.22}$$

⁵for example of the GW analysis pipeline, see section 3.2.

⁶see chapter 6.

Chapter 5. Coincidence Analysis

where $\mu_X = f_X^{\text{im}}$ for $X \in \{a, b, c\}$. Let us again suppose that we have an infinitesimal chunk of common observation time (lifetime) as dt . The probability of having 1 trigger in a , in b , and in c inside this dt ,

$$\begin{aligned} dp_a &= f_a^{\text{im}} dt \\ dp_b &= f_b^{\text{im}} dt \\ dp_c &= f_c^{\text{im}} dt. \end{aligned} \tag{5.23}$$

Therefore, the number of coincidences

$$\begin{aligned} dN &= \text{jointFAR} \cdot dt = (dp_a) \times (P_{0;b}(w_c)) \times (P_{0;c}(w_c)) \\ &\quad + (dp_b) \times (P_{0;a}(w_c)) \times (P_{0;c}(w_c)) \\ &\quad + (dp_c) \times (P_{0;a}(w_c)) \times (P_{0;b}(w_c)) \\ &= f_a^{\text{im}} dt \times f_b^{\text{im}} \times f_c^{\text{im}} \times w_c^2 \\ &\quad + f_b^{\text{im}} dt \times f_a^{\text{im}} \times f_c^{\text{im}} \times w_c^2 \\ &\quad + f_c^{\text{im}} dt \times f_a^{\text{im}} \times f_b^{\text{im}} \times w_c^2 \\ &= 3 \cdot f_a^{\text{im}} \cdot f_b^{\text{im}} \cdot f_c^{\text{im}} \cdot w_c^2 \cdot dt, \end{aligned} \tag{5.24}$$

and thus, to generalise the calculation for Net-detectors, the joint FAR will be,

$$\text{jointFAR} = \text{Net} \times w_c^{\text{Net}-1} \prod_{X=1}^{\text{Net}} f_X^{\text{im}}, \tag{5.25}$$

where Net is the number of considered detectors, w_c is the coincidence window and f_X^{im} is the imitation frequency of detector- X . Moreover, the joint FAP can be calculated as follows,

$$\text{jointFAP} = 1 - e^{-\text{jointFAR} \times \text{lifetime}}, \tag{5.26}$$

by taking into account the Poisson statistics.

Chapter 6

Distinguishing Astrophysical Bursts of Low-energy Neutrinos from the Noise

From all previous chapters, it is evident that the detection of GWs from CCSNe could be a milestone for our understanding of the explosion mechanism. However, we also realized that the detection of such GW bursts from CCSNe is really challenging due to the weakness of the amplitude of GWs. In order to help the GW detection, combined multimessenger informations provided by other probes are fundamental. Neutrinos are the most efficient counterpart in this astrophysical event. Their detection could be a fundamental trigger for the GW search. For this reason, the work to increase the detection efficiency and the statistical significance of neutrino signals will reflect on the increase of the detection probability to catch the GW signals. In this chapter and the next one, we will discuss our results in the relation to that.

6.1 A Simple Double Exponential Model of the CCSN Events in Detector Data Streams

To improve the CCSN search in neutrino detectors, we proposed to use the temporal structure of the expected astrophysical signal and its differences

from background. In particular, based on reference [119], we are going to introduce a new parameter describing the signal shape. Despite the fact that this parameter is very basic and poorly sensitive to the details of the neutrino luminosity from CCSNe, we are going to test its power by using Monte Carlo simulations of expected signals for different distances buried in background distribution of about 10 years data chunk for each simulated detector data set (see table 6.3 for the details of the involved detectors). In order to perform such simulations, we made the following assumptions on the neutrino emission,

1. The expected energy from a CCSN in terms of low-energy neutrinos $\varepsilon_\nu \approx 3 \times 10^{53}$ erg.
2. This energy ε_ν satisfies the equipartition of the 6 flavours of neutrinos. This is valid within a factor of 2 [120].
3. The temporal evolution of a signal injection satisfies the double-exponential model,

$$f(t) = \left[1 - \exp\left(\frac{-t}{\tau_1}\right) \right] \exp\left(\frac{-t}{\tau_2}\right), \quad (6.1)$$

where $\tau_1 = 10 - 100$ ms and $\tau_2 \geq 1$ second.

4. The neutrino spectra are assumed to be quasi-thermal spectra. The neutrino fluence (satisfying the equipartition) differential in neutrino energy E can be written as,

$$\Phi_i^0 = \frac{\varepsilon_i}{4\pi D^2} \times \frac{E^\alpha e^{-E/T_i}}{T_i^{\alpha+2} \Gamma(\alpha+2)}; \quad i = \nu_e, \nu_\mu, \nu_\tau, \bar{\nu}_e, \bar{\nu}_\mu, \bar{\nu}_\tau, \quad (6.2)$$

where $\varepsilon_i = \varepsilon_\nu/6$ and “temperature” $T_i = \langle E_i \rangle / (\alpha + 1)$ with $\langle E_i \rangle$ is the average energy per flavour and $\alpha = 3$. $\langle E_{\nu_e} \rangle = 9$ MeV, $\langle E_{\bar{\nu}_e} \rangle = 12$ MeV, $\langle E_{\bar{\nu}_x} \rangle = \langle E_{\nu_x} \rangle = 15.6$ MeV (where x is $\{\mu, \tau\}$), and non-electronic temperature is 30% higher than the one of $\bar{\nu}_e$.

5. The main channel is considered here, which is the inverse-beta decay (IBD),

$$\bar{\nu}_e + p \rightarrow n + e^+. \quad (6.3)$$

The percentage contribution of additional channels with respect to the total is of 35% for Borexino, 22% for Kamland, 21% for Super-K and 12% for LVD, indeed, with fairly large uncertainties on these numbers.

6. Moreover, there is an admixture of the unoscillated flavor fluences detected due to standard matter effect Mikheyev-Smirnov-Wolfenstein (MSW) neutrino oscillations and depending on whether the normal or inverted hierarchy, this can also give an effect on the number of events detected. It has been chosen the normal hierarchy to be conservative since it gives us a lower number of neutrino events for the same source distance.

6.2 More Details of the Assumption

6.2.1 Background and Injection Behavior

To describe the assumption better, especially for the temporal evolution of a signal injection as well as background, we can plot the temporal evolution of equation 6.1 in figure 6.1 as the blue area, with $\tau_1 = 10$ ms and $\tau_2 = 1$ s. Meanwhile, it is also shown the expected (constant) background evolution in time as the orange color. This general model basically fits with CCSNe, failed-SNe¹, as well as quark novae². Moreover, SN1987A also satisfies this general model [46]. This model, in fact, can be different from the more complex numerical simulations such as in [121]. However, the difference will not be significant when the focus is (and it is) on low statistics signals (far or weak supernovae).

The fluence Φ_i^0 following equation 6.2 as a function of neutrino energy E for each species can be seen in figure 6.2. Here, we assume a CCSN in 10 kpc is

¹This is when the core collapse failed to explode and instead forming a central blackhole.

²Quark novae are predicted to exist from the conversion of the normal neutron stars to quark stars.

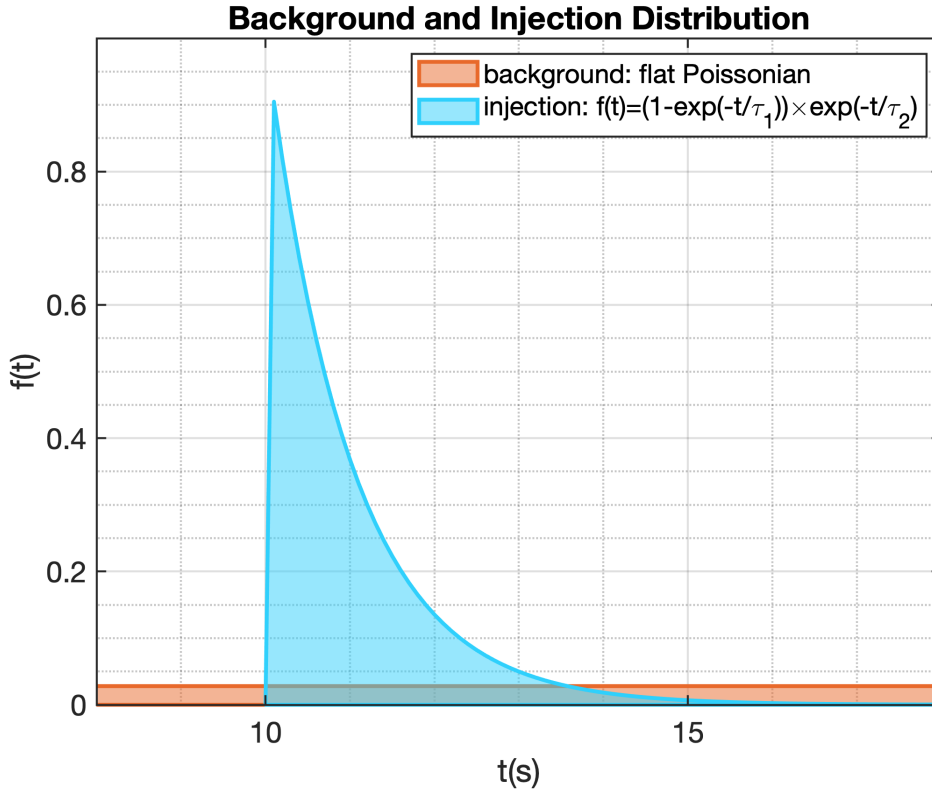


FIGURE 6.1: The time evolution of injections, following the double-exponential of equation 6.1, is show as blue area. Here, we use $\tau_1 = 10$ ms and $\tau_2 = 1$ s. It is also shown the expected (constant) time evolution of background as orange area.

detected by Super-K with the detector energy threshold of 7 MeV. The average neutrino energies are 12, 9, and 15.6 MeV for $\bar{\nu}_e$, ν_e , and ν_x respectively. We use the IBD cross-section from reference [48, 122] with a naive approximation following [48],

$$\sigma_{\text{IBD}} \approx 10^{-43} \left(\frac{E}{[\text{MeV}]} \right)^2 [\text{cm}^2]. \quad (6.4)$$

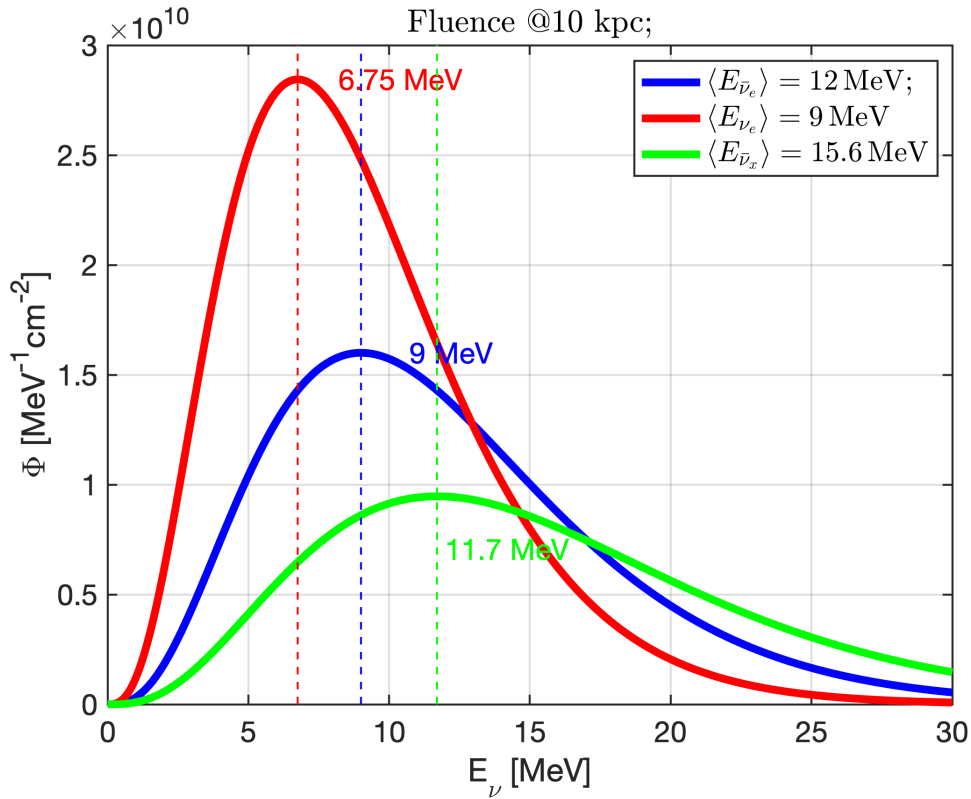


FIGURE 6.2: The fluence Φ_i^0 as a function of neutrino energy E . Blue, red, and green curve are respectively for $\bar{\nu}_e$, ν_e , and ν_x , where x stands for all other flavors of neutrinos and anti-neutrinos. The peak energy is also written above each curve.

6.2.2 Matter Effect

The standard MSW neutrino oscillation (see review such as in [123]) may also give us a different solution of the expected number of events. In our case, we can notice that actually fluence in equation 6.2 is proportional to flux in equation 6.5. Let us discuss the fluxes of neutrinos with oscillation from reference [46, 124]. For the normal hierarchy, we can write the survival probability and the observed $\bar{\nu}_e$ flux as,

$$\begin{aligned} \bar{P} &= U_{e1}^2 \\ F_{\bar{\nu}_e, \text{NH}} &= \bar{P} F_{\bar{\nu}_e}^0 + (1 - \bar{P}) F_{\bar{\nu}_\mu}, \end{aligned} \quad (6.5)$$

Chapter 6. Distinguishing Astrophysical Bursts of Low-energy Neutrinos
from the Noise

where F^0 is the flux without oscillation, $U_{e3} = \sin \theta_{13}$, $U_{e1} = \cos \theta_{12} \cos \theta_{13}$, with,

$$\begin{aligned}\sin^2 \theta_{12} &= 0.307 \pm 0.013, \\ \Rightarrow \theta_{12} &\simeq 33.6^\circ,\end{aligned}\tag{6.6}$$

and

$$\begin{aligned}\sin^2 \theta_{13} &= (2.18 \pm 0.07) \times 10^{-2}, \\ \Rightarrow \theta_{13} &\simeq 8.5^\circ,\end{aligned}\tag{6.7}$$

taken from Particle Data Group (PDG) 2018/2019 [125].

We also assume that the flux of $\bar{\nu}_\mu$ is equal to the flux of $\bar{\nu}_\tau$. Here, \bar{P} for the normal hierarchy is about 0.7, where it depends mainly on θ_{12} . Meanwhile, for the inverted hierarchy [124],

$$F_{\bar{\nu}_e, \text{IH}} = \bar{P}_{\text{inv}} F_{\bar{\nu}_e}^0 + (1 - \bar{P}_{\text{inv}}) F_{\bar{\nu}_\mu},\tag{6.8}$$

with,

$$\bar{P}_{\text{inv}} = U_{e1}^2 P_H + U_{e3}^2 (1 - P_H),\tag{6.9}$$

where the flip probability P_H (the loss of adiabaticity at the “resonance” related to the atmospheric Δm^2) can be written as³,

$$P_H(E_\nu, \theta_{13}) = \exp \left[- \left(\frac{E_{na}}{E_\nu} \right)^{2/3} \right],\tag{6.10}$$

where,

$$E_{na} \simeq 1.08 \cdot 10^7 \text{ MeV} \left(\frac{|\Delta m_{32}|^2}{10^{-3} \text{ eV}^2} \right) C^{1/2} \sin^3 \theta_{13},\tag{6.11}$$

³see cf. equation 13 in [124] for the detailed calculation.

Chapter 6. Distinguishing Astrophysical Bursts of Low-energy Neutrinos from the Noise

where $|\Delta m_{32}|^2 \simeq O(10^{-3} \text{ eV}^2)$ and $C \simeq O(1 - 15)$ [124], therefore equation 6.10 can be approximated as,

$$P_H(E_\nu, \theta_{13}) \simeq \exp \left[-\frac{U_{e3}^2}{3.5 \times 10^{-5}} \left(\frac{20 \text{ MeV}}{E_\nu} \right)^{2/3} \right], \quad (6.12)$$

where we assume the smooth density profile inside the stellar core as in cf. equation 7 in [124]. This P_H gives us the value of \bar{P}_{inv} , depending highly on the determination of θ_{13} value. In fact, the determination of θ_{13} was quite problematic and it is solved only by recent experiments such as the result of T2K experiment [126] giving us $\sin^2 2\theta_{13} \simeq 0.140 \rightarrow \theta_{13} \simeq 11^\circ$, with 7.3σ against null hypothesis of $\sin^2 2\theta_{13} = 0$.

We can compare our model with the models used in [127]. The model comparison can be seen in table 6.1. Wilson model [11] uses SN1987A as its basis with $M_{\text{progenitor}} = 20M_\odot$. NK1 [128] has $M_{\text{progenitor}} = 20M_\odot$, revival time is 200 milliseconds after the bounce, and metallicity $Z = 0.02$. Meanwhile, NK2 has $M_{\text{progenitor}} = 13M_\odot$, revival time = 100 milliseconds, and $Z = 0.004$. The expected number of IBD events in Super-K can be compared with the result of reference [127]. The comparison can be seen in table 6.2.

TABLE 6.1: The model comparison used in [127] versus our work. *estimated from figure 1.4.

Models	$E_{\bar{\nu}_e, \text{tot}}$ [erg]	$E_{\bar{\nu}_x, \text{tot}}$ [erg]	$\langle E_{\bar{\nu}_e} \rangle$ [MeV]	$\langle E_{\bar{\nu}_x} \rangle$ [MeV]
This work	5×10^{52}	5×10^{52}	12	15.6
Wilson	4.7×10^{52}	$4.7 \times 10^{52*}$	15.3	19*
NK1	2.82×10^{52}	3.27×10^{52}	11.1	11.9
NK2	2.68×10^{52}	3.18×10^{52}	10.8	11.9

However, we need to remember that our P_H is for the smooth density profile. Furthermore, this P_H determination is still under discussion due to the fact that it may be possible to have a shock inside this stellar core that gives us different P_H . In fact, reference [123] uses the numerical P_H as a function of neutrino energy (see figure 6.3), which practically can give different \bar{P}_{inv} from

Chapter 6. Distinguishing Astrophysical Bursts of Low-energy Neutrinos from the Noise

TABLE 6.2: Expected number of events in Super-K from a CCSN at 10 kpc. Here, we compare our simple result with the result of [127] with different models such as Wilson [11] as well as NK1 and NK2 [128] and $E_{\text{thr}} = 7$ MeV.

Models	No oscillation	Normal H.	Inverted H.
Our work; $E_{\text{thr}} = 5$ MeV	5737	6277	7377
Our work; $E_{\text{thr}} = 7$ MeV	5595	6161	7314
Our work; $E_{\text{thr}} = 10$ MeV	5078	5723	7036
Wilson	4923	5667	7587
NK1	2076	2399	2745
NK2	1878	2252	2652

our case since we use analytical approach taken from [2, 46, 124]. As a rule of thumb, when $P_H \rightarrow 1$, the number of events in normal and inverted hierarchy are indistinguishable, meanwhile for $P_H \rightarrow 0$ (as in our case, which is basically called “adiabatic” condition), the inverted hierarchy will produce the number of events way higher than the normal hierarchy due to the fact that the $\bar{\nu}_e$'s arriving in the Earth are basically 100% ($\bar{P}_{\text{inv}} = 0$) from the $\bar{\nu}_\mu$'s in the source and the $\langle E \rangle_{\bar{\nu}_\mu}$ has higher average energy than $\langle E \rangle_{\bar{\nu}_e}$.

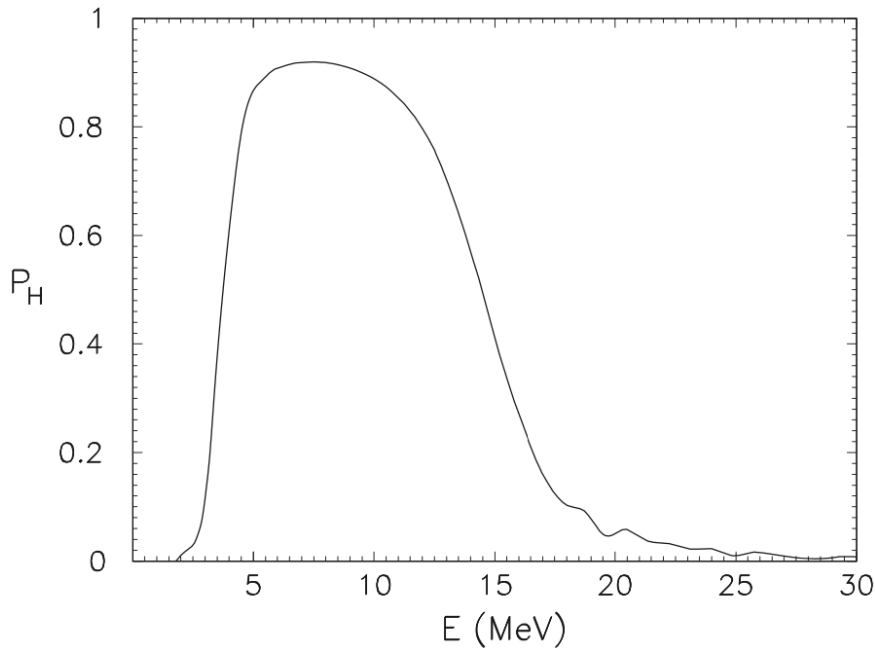


FIGURE 6.3: The P_H as a function of neutrino energy. Figure is taken from [123].

We basically follow the total energy in $\bar{\nu}_e$ and $\bar{\nu}_x$ used by Wilson [11] model in [127] but with our own fluence and other details like the average energy $\langle E_{\bar{\nu}_e} \rangle$ and $\langle E_{\bar{\nu}_x} \rangle$. This fluence and expected number of events highly depend on the average neutrino energy $\langle E_\nu \rangle$ and the total energy $E_{\bar{\nu},\text{tot}}$ that are used. Moreover, we need to keep in mind that in our discussion here, we do not take into account the intrinsic efficiency function of the detector as well as the smearing function like in [122]. In addition, we will not discuss the differences among models since it is outside of our study scope.

The MSW neutrino oscillation can give us more events due to the fact that the $\langle E_{\bar{\nu}_\mu} \rangle > \langle E_{\bar{\nu}_e} \rangle$ and thus more neutrinos with higher energy arriving on earth when there is neutrino oscillation. In addition, if we use a different energy threshold, we expect a different number of events indeed, as we can see in table 6.2 in row 1 to 3 of our model. We also plot the expected number of events as a function of neutrino energy in figure 6.4 for $E_{\text{thr}} = 7$ MeV.

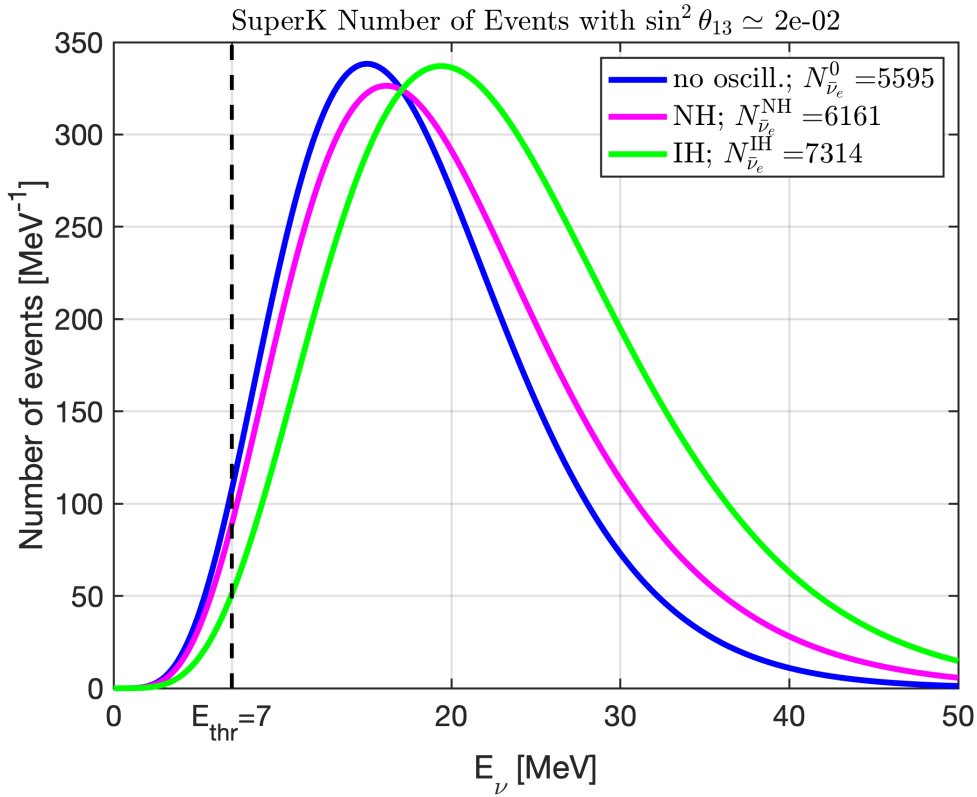


FIGURE 6.4: The number of events in Super-K for normal and inverted hierarchy, with $\theta_{13} \simeq 8.5^\circ$ (see text for the explanation).

6.3 Counting Analysis

In neutrino analysis to search for CCSNe like in chapter 3, a temporal data set consisting of all the collected events is binned with a temporal window $w = 20$ seconds, with a requirement that their visible energies are above some specific thresholds depending on the involved detectors (see table 6.3 column 3). A group of events passing the threshold inside this window is called a *cluster*. Each cluster is characterised by multiplicity, m_i , i.e. the number of events inside the cluster and duration, Δt_i , defined as the time difference between the last and the first event inside the cluster. Indeed, our cluster is defined only when a multiplicity $m_i \geq 2$. Moreover, to increase the detection probability and to tackle the boundary problem due to this binning, we also repeat the procedure by shifting the binning in 10 seconds.

In order to understand better the clustering of events and the problem we face when we rely on counting statistics, we put the cartoon of the counting steps in figure 6.5, assuming our data set consists of injection of neutrino burst from a CCSN in 10 kpc detected by LVD, which is considered as high statistic signal and the analysis will clearly be able to understand that this cluster is due to signal. Meanwhile, if we see figure 6.6 with the injection in 65 kpc, we may confuse it with background cluster.

To see the performance of the method, we focus on the detection efficiency η and the misidentification probability ζ , i.e. the probability of wrongly confusing a background cluster from an injected signal cluster. The statistical significance for each cluster that we find is based solely on the statistics of the cluster. In this case, it is introduced an *imitation frequency* f_i^{im} defined as,

$$f_i^{\text{im}} = N \times \sum_{k=m_i}^{\infty} \frac{(f_{\text{bkg}} w)^k e^{-f_{\text{bkg}} w}}{k!} [\text{day}]^{-1}, \quad (6.13)$$

where $N = 8640$ is the number of bins in a day and f_{bkg} is the background frequency of the experiment. This f_i^{im} can be understood basically as how often the background clusters can mimic the i -th cluster with the multiplicity

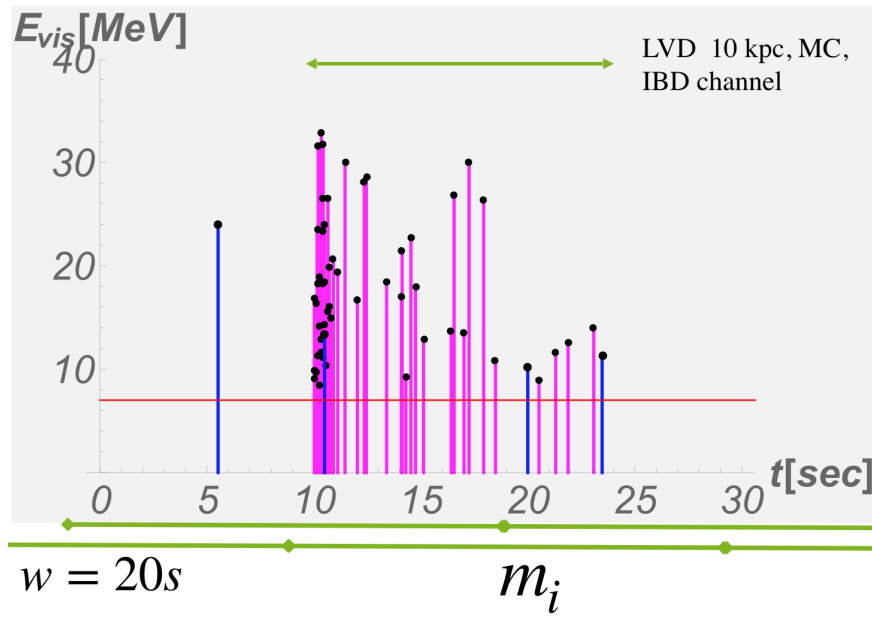


FIGURE 6.5: A cartoon of a time-series data consisting of injection in 10 kpc (high-statistic signal) seen by LVD.

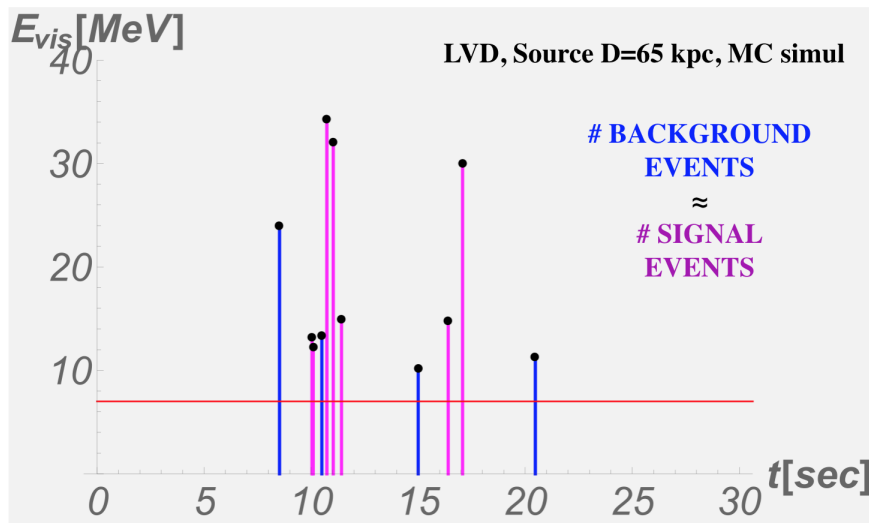


FIGURE 6.6: A cartoon of a time-series data consisting of injection in 65 kpc (low-statistic signal) seen by LVD.

equal or bigger than that of the i -th cluster. The lower the value of f^{im} , the higher is the probability of the i -th cluster to be due to signal, and of course, the higher the f^{im} the lower is the probability that it is due to real signal. In SNEWS⁴, the imitation frequency of $f^{\text{im}} \leq 1/100$ years is required in order to select signals.

⁴Subsection 4.1.

6.4 A New Cut to Improve the Analysis of Neutrino Data to Hunt CCSNe

The standard method is purely statistical and no other physical characteristics of the signal are used to disentangle signals from background. In order to improve this approach, we introduce a new parameter called ξ_i for each cluster defined as,

$$\xi_i = \frac{m_i}{\Delta t_i}, \quad (6.14)$$

where m_i is the multiplicity and Δt_i is the duration of the i -th cluster.

The background data for each detector is simulated by Monte Carlo method with the assumption that the background satisfies the Poisson distribution with *fluctuation*. The simulated background is in the chunk of 10 years for each detector. Meanwhile, the simulated signals are made following the equation 6.1 with $\tau_1 = 10$ ms and $\tau_2 = 1$ s for several distances in the range of 8.5 – 500 kpc with the expected number of events follows the fluence in equation 6.2 with fluctuation.

Then, we can study the ξ distribution of pure background clusters and of background + injection clusters in terms of probability density function (PDF). The background PDF is well described by 4-parameter gamma distribution (figure 6.7) in the case of Super-K, moreover, the ξ values for pure background clusters tend to be in the region $\xi \lesssim 1$. Meanwhile, the background + injection distribution tend to have higher ξ values. The stronger (closer) the injections, the bigger the ξ value distribution of the related, as we can see in figure 6.7. When the distance of CCSN injections is 65 kpc, the expectation of ξ value is around 30, while when the distance is 400 kpc, the ξ distribution becomes similar to the background.

In order to find the best ξ value to separate the injections from background, we can maximize the equation below,

$$\Xi[\xi]_X = \int_0^{\bar{\xi}_X} \text{PDF}_X^{\text{bkg}} d\xi + \int_{\bar{\xi}_X}^{\infty} \text{PDF}_X^{\text{sig+bkg}}(D) d\xi, \quad (6.15)$$

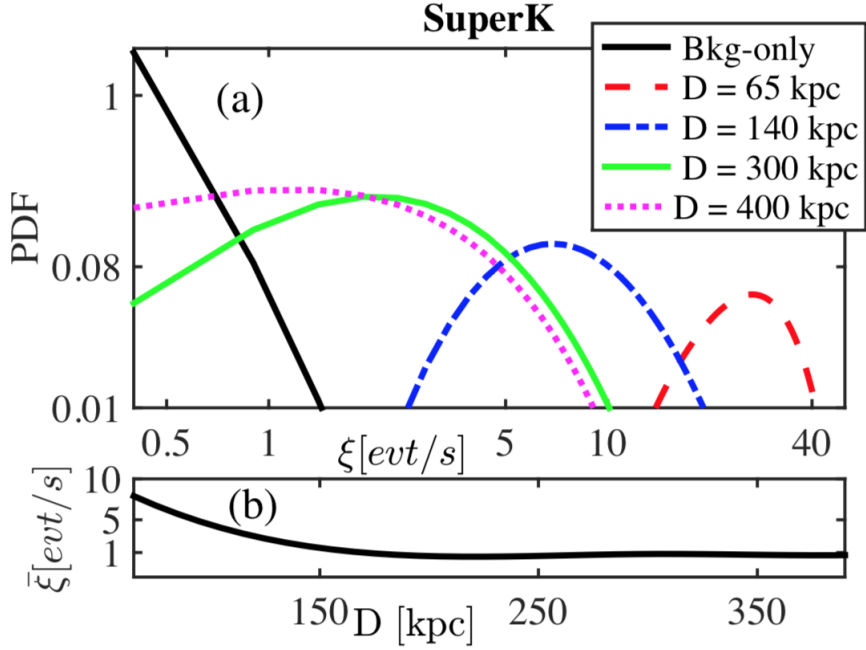


FIGURE 6.7: Panel (a): PDF for background (+ injections of several distances) clusters as a function of ξ parameter in the case of Super-K detector. Panel (b): the optimal cut value for the ξ parameter, $\bar{\xi}(D)$, as a function of the source distance D for Super-K detector. Figure is taken from [119].

with respect to the optimal value called $\bar{\xi}$. However, this can be done only if the source distance is known. Thus, in general the $\bar{\xi}(D)$ is a function of the CCSN distance as reported in figure 6.7 panel (b). However, standard search for CCSNe may actually be a blind search with no information on the distance so that we can take the $\bar{\xi}$ to optimize the search of the distant sources⁵. This implies that we will consider the smaller value of $\bar{\xi}_X$.

All the $\bar{\xi}$ cut value for each detector can be seen in table 6.3 in column 5. Thus, the $\bar{\xi}_X$ is used as an additional cut; all clusters found in data from the X -th detector must satisfy $\xi_i \geq \bar{\xi}_X$. With this additional cut on the data, we can test the performance of the method by investigating the detection probability η as well as the misidentification probability ζ before and after the ξ -cut. The η is simply the ratio between the number of clusters due to injections⁶ and the number of total injections. On the other hand, the ζ is basically the

⁵Indeed, we may also have the distance information.

⁶or simply called *recovered* injections.

fraction of clusters due to background over the total clusters. We need to notice that here, for each cluster passing all the analysis steps⁷ whether due to background or injection, we do not require a significance value higher than a specific threshold; we only consider that the cluster is recovered or not.

TABLE 6.3: The details of involved detectors

Detector	M [kton]	E_{thr} [MeV]	f_{bkg} [Hz]	$\bar{\xi}$ [Hz]	\bar{D} [kpc]	G
Borexino	0.3	1	0.048	0.65	20	6.9
Super-K	22.5	7	0.012	0.72	200	8.9
KamLAND	1	1	0.015	0.77	50	13.4
LVD	1	10	0.028	0.72	40	14

Results of the Implementation on Single Detectors

We implement this cut method to Super-K data and compare the η and ζ for the ξ -cut versus the standard procedure without any cut. In Super-K model, the $f^{\text{im}} \leq 1/\text{day}$ is translated as the expectation of $m_i \geq 4$, meaning that a CCSN can be detected on average till the distance $D_{\text{SK}} \approx 400$ kpc. Panel (a) in figure 6.8 shows the η in red and ζ in blue, where the solid line belongs to our ξ -cut method, on the other hand, the dashed line describes the standard procedure. From this figure, it is evident that the efficiency η for both the ξ and standard method is practically 100% till a distance of ~ 200 kpc. On the other hand, the misidentification drops from 23% by using the standard way to a value as small as around 3% by applying our method.

We can also describe the findings as the gain factor G where it is basically the ratio between the standard-procedure misidentification probability ζ' and our ξ -cut misidentification probability ζ ,

$$G = \frac{\zeta'}{\zeta}. \quad (6.16)$$

⁷including the implementation of $\bar{\xi}_X$ cut, indeed.

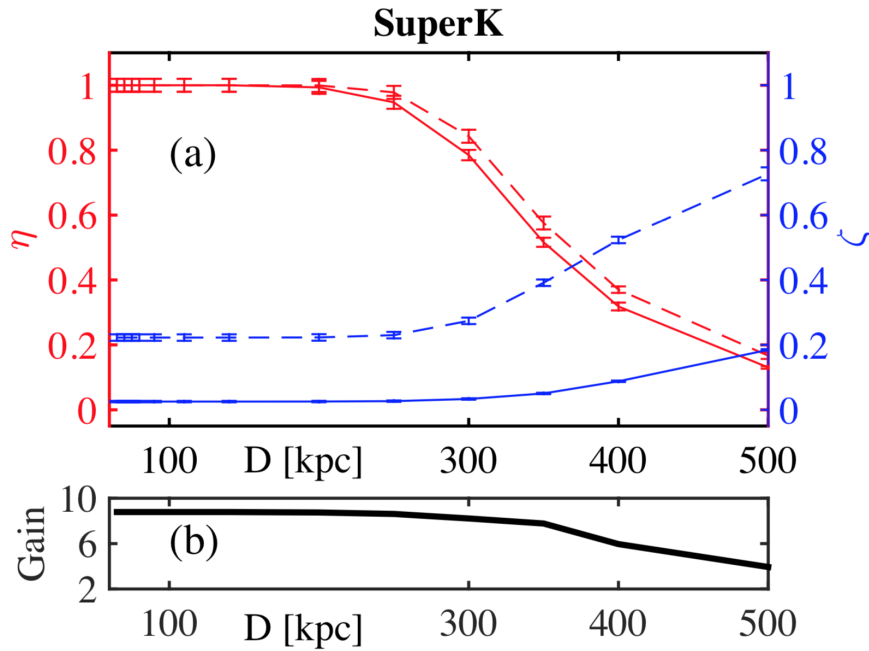


FIGURE 6.8: Panel (a): The efficiency η (red) and the misidentification probability ζ (blue) for Super-K modelled-detector data. Panel (b): The gain factor G in Super-K modelled-detector data. Figure is taken from [119].

The G as a function of distance D for the Super-K modelled data can be seen in Panel (b) in figure 6.8. As we can see from the figure, our method produces lower misidentification probability ζ comparing with the standard procedure, with the gain factor of about 9 times. This gain value is kept up to the distance of 200 kpc. Later on, the gain is gradually decreasing to about 3 in 500-kpc distance. To give a better idea, for each individual detector we put the reference of the furthest distance without efficiency loss after the cut and its corresponding gain value in column 6 and 7 of table 6.3.

This G can also be converted in terms of the increased horizon. A gain factor of 10 in Super-K means that the detector can work (by imposing the ξ -cut) at a threshold on f^{im} 10 times higher than the standard f^{im} threshold since the background level will be the same in those two cases. In the on-line search for CCSNe by Super-K [127], the normal warning⁸ threshold is $m_i \geq 25$ corresponding to $f^{\text{im}} \leq 3.5 \times 10^{-10}$ per year and **the corresponding maximum distance of 147 kpc**. With the ξ -cut method, this threshold

⁸This normal warning will be sent to SNEWS [62, 101]. See chapter 4.

can be theoretically lowered, but still with the same background level, to $m_i \geq 11 \Leftrightarrow f^{\text{im}} \leq 3.5 \times 10^{-9}$ per year, which implies the expansion of the search horizon up to $D = 221$ kpc.

6.5 The Implementation of the Cut Method on the Network of Detectors

The ξ -cut method can be also implemented in a network of neutrino detectors. We can search for clusters that are correlated in time from two data streams by doing coincidence analysis, explained in detail in chapter 5. A coincidence happen if two clusters from two different-detector data sets are separated in a window $w_c \leq 10$ seconds [62]. This coincidence analysis indeed has effects in our analysis: increasing the efficiency η and decreasing the misidentification probability ζ .

The joint- f^{im} (or joint-FAR) that we adopt uses the SNEWS-like method (see chapter 5) and in our study here, we uses 2-data-set coincidence analysis, and following equation 5.25 therefore,

$$\begin{aligned} \text{jointFAR} &= \text{Net} \times w_c^{\text{Net}-1} \prod_{X=1}^{\text{Net}} f_X^{\text{im}}, \\ \Rightarrow \text{jointFAR}_{\text{double}} &= 2 \times w_c \times f_1^{\text{im}} \times f_2^{\text{im}}, \end{aligned} \quad (6.17)$$

where $\text{Net} = 2$ for 2 detector network. To get the jointFAR of the level of ≤ 1 per day, if there are two detectors in the network, each should have $f^{\text{im}} \leq 66$ per day and if there are three, each needs to be ≤ 265 per day and so on.

In a network of detectors, we also define the joint cut value, named $\bar{\xi}^*$. We have studied several possible cuts such as:

1. Single-cut: each data set is considered as a single analysis and the cut is based on individual detector, which is $\xi_{i,X} \geq \bar{\xi}_X$ of X -th detector.

2. Product-cut: this cut depends on the $\bar{\xi}_X$, which is the cut value for X -th detector, however, in this cut, we use the squared product of each detector cut,

$$\begin{aligned}\bar{\xi}^* &= \sqrt[\text{Net}]{\prod_{X=1}^{\text{Net}} \bar{\xi}_X}, \\ \Rightarrow \bar{\xi}_{\text{double}}^* &= \sqrt{\bar{\xi}_1 \times \bar{\xi}_2},\end{aligned}\tag{6.18}$$

where we use $\text{Net} = 2$ for 2 detector network. So, for each coincidence found, it must also pass the cut of $\sqrt[\text{Net}]{\prod_{X=1}^{\text{Net}} \bar{\xi}_X} > \bar{\xi}^*$.

3. Diagonal-cut: here, we write the cut as a function of a straight line,

$$y = -\frac{\bar{\xi}_2}{\bar{\xi}_1} \times x + \bar{\xi}_2,\tag{6.19}$$

for a network of 2 detectors, where $x \in \{\xi_{i,1}\}$ and $y \in \{\xi_{i,2}\}$ for i is the index of the observed coincidences. For 3 or more detectors, this will be analogous, in which the cut will have an $(\text{Net} - 1)$ -dimension plane.

From these several possible options, we can construct them as in figure 6.9. The green area is for the single-cut, the red area is for the product-cut, while the blue area is for the diagonal-cut. Indeed, there are many more possible ways of constructing the network cut. However in this case, we give some basic examples of them. Here, we notice that from the options we introduced before, the hardest cut is from single-cut where the analysis in a network is the same as the single-data-set analysis. Meanwhile, the diagonal-cut can give us more passed coincidences, which also means more coincidences due to background. Thus, in this analysis, we use product-cut to be conservative.

In addition, working in the network of detectors also slightly modifies the definition of the efficiency and misidentification probability, where now we use the symbol η^* and ζ^* for the network efficiency and the network-misidentification probability, respectively. They are calculated for the coincident clusters as follow: the η^* is the ratio between the recovered injections

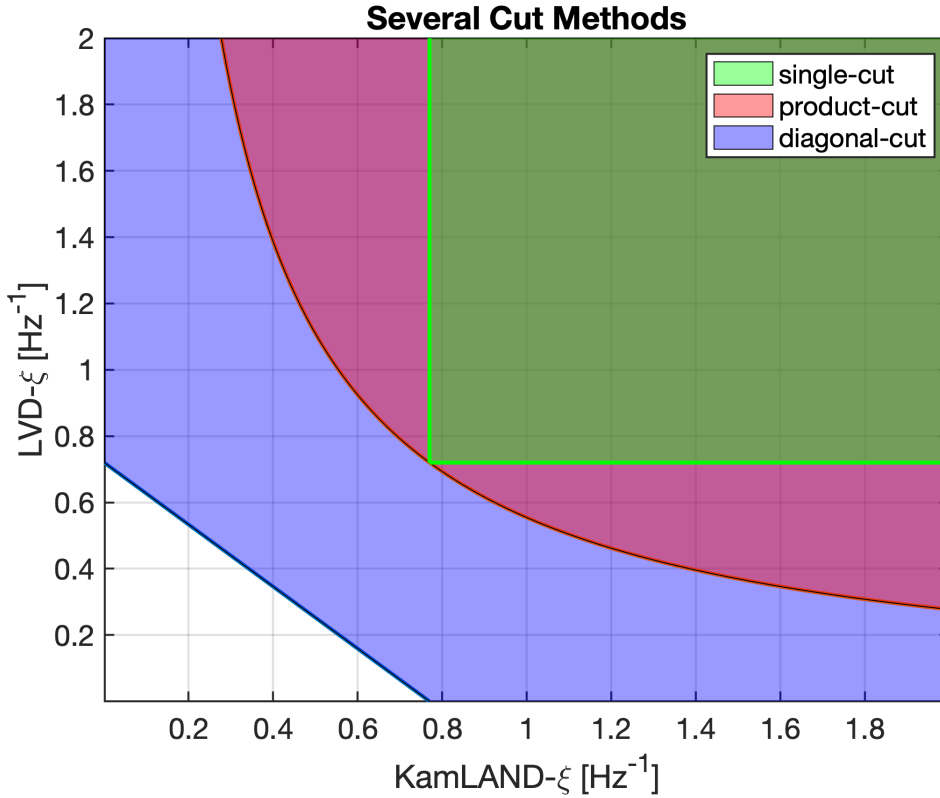


FIGURE 6.9: Several possible cuts for a network of detectors. The green area is where the coincidences pass the single-cut, the red area is for the product-cut, while the blue area is for the diagonal-cut. See text for the explanation.

from coincident clusters and the number of total injections, meanwhile the ζ^* is the fraction of the number of background coincident clusters over the total number of coincidences. Indeed, the gain now becomes,

$$G^* = \frac{\zeta^{*'}}{\zeta^*}. \quad (6.20)$$

Results of the Implementation on Network of Detectors

We keep using $\text{Net} = 2$ as in equation 6.17 and 6.18 due to the fact that as a case study, we use the network of two detector data. In particular, here we will discuss the result of the network of LVD and KamLAND⁹. We apply the coincidence analysis for both data sets as a network with the requirement of

⁹Other possible network configurations are also taken into account, yielding an analogous result.

jointFAR ≤ 1 per day. The result can be seen in figure 6.10 for which Panel (a) shows η^* as the red color with the scale on the left and ζ^* as the blue color with the scale on the right. Our cut method here is represented as the solid line, meanwhile the standard methods is translated as the dashed line. Additionally, the gain is described in Panel (b).

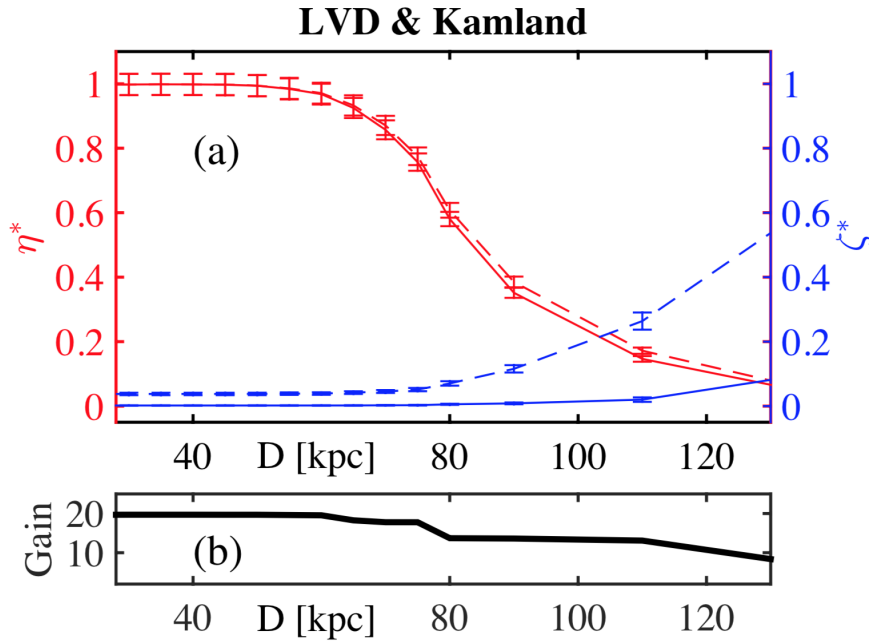


FIGURE 6.10: Panel (a): The efficiency η^* (red) and the misidentification probability ζ^* (blue) for LVD-KamLAND modelled-detector data where the ξ -cut is represented in the solid line and the standard is in the dashed line. Panel (b): The gain factor G in LVD-KamLAND modelled-detector data. Figure is taken from [119].

The misidentification probability is somewhat constant until 75 kpc with a value of 4% with the standard procedure and decreases to $\sim 0.2\%$ by applying our cut. Thus, the gain factor obtained in 75-kpc distance is around ~ 20 while it gradually decreases to about 10 as the distance goes further. As we can expect that the coincidence analysis itself already decreases highly the background, while the ξ -cut decreases the background even further. To give a better idea, this network example working at a FAR of 0.001/day (0.365/year) with the ξ -cut can reach the same background level of the same network with the threshold of 1/1000 years by the standard statistical selection method.

We have also tested this method to the other possible network among LVD, Borexino, KamLAND, and Super-K. The improvement is somewhat in

Chapter 6. Distinguishing Astrophysical Bursts of Low-energy Neutrinos from the Noise

the same degree as our previous case study. For LVD - Borexino or KamLAND - Borexino the gain factor is ~ 19 , with a reduced distance $\bar{D} \sim 50$ kpc due to the lower sensitivity of Borexino.

We have seen that by introducing a new parameter ξ , we can improve further the analysis for CCSN search. This can be a promising method to be applied to real detector data. Moreover, we also understand that the method that we explain here could be improved. Thus, this result motivates us to study further the power of this ξ parameter. In chapter 7, we will discuss further this new method by exploiting deeper this ξ parameter.

Chapter 7

The Modified Imitation Frequency to Expand CCSN Search Horizon of Neutrino Detectors

In this chapter, we will exploit further the new ξ parameter that we have introduced and discussed in the previous chapter. As we have previously discussed in chapter 6, for low energy neutrino analysis to search for CCSNe, a temporal data set is binned with a time window and inside each window we count the number of events passing an energy threshold, and therefore we can define a cluster of events. Then, we calculate imitation frequency for each cluster in order to understand the probability of the cluster to be due to an astrophysical source (significance or false-alarm-probability). Moreover, we have also introduced a new parameter called ξ in which it can be used to define a cut in order to suppress the number of clusters due to background in chapter 6 and in [119]. Nevertheless, we have not discussed yet how this new parameter affects the imitation frequency of each cluster that we can find. This is an important issue to complete the discussion of ξ parameter for low-energy neutrino analysis. We will focus on this issue for the rest of the chapter, which is also the result in [129].

The expected number of events inside a cluster due to background supposedly follows Poisson distribution. Therefore, the significance (false-alarm-probability) of these clusters is calculated based on Poisson statistics, and it

is correlated with the imitation frequency f^{im} defined in equation 6.13. The quantity after the summation symbol in equation 6.13 is basically the probability to observe a cluster of k events¹ in the temporal window w , and let us call it as $P(k)$,

$$P(k) = \frac{(f_{\text{bkg}}w)^k e^{-f_{\text{bkg}}w}}{k!}. \quad (7.1)$$

Thus, we can rewrite the f^{im} from equation 6.13 as,

$$\begin{aligned} f_i^{\text{im}} &= N \times \sum_{k=m_i}^{\infty} \frac{(f_{\text{bkg}}w)^k e^{-f_{\text{bkg}}w}}{k!} [\text{day}]^{-1}, \\ &= N \times \sum_{k=m_i}^{\infty} P(k). \end{aligned} \quad (7.2)$$

In addition to multiplicity m_i , we have known that a cluster is actually also characterised by its duration Δt_i and the maximum duration is the bin width itself: 20 seconds. This duration of a cluster, thus, can vary from *theoretically* 0 to 20 seconds.

Moreover, we also have known the definition of ξ parameter from equation 6.14. Here, differently from chapter 6, we will not use ξ as a parameter cut. Instead, we will combine this ξ parameter with the previously known parameter m_i from the standard analysis. Thus, we will have two parameters (m_i and ξ_i) for each cluster. From these two parameters, we will see how the imitation frequency can be modified. We expect that an astrophysical neutrino burst should have a smaller value of f^{im} while a background cluster will have practically the same f^{im} value as the standard method.

¹Indeed, it actually is a PDF of Poisson distribution.

7.1 The Modified Imitation Frequency with Two Parameters

Supposing that we have a certain PDF for ξ background distribution, our new imitation frequency F^{im} (capital letter) should be in the form of,

$$\begin{aligned}
 F_i^{\text{im}} &= 8640 \times \sum_{k=m_i}^{\infty} P(k \cap \xi) \\
 &= 8640 \times \sum_{k=m_i}^{\infty} P(k, \xi) \\
 &= 8640 \times \sum_{k=m_i}^{\infty} P(\xi|k)P(k) \\
 &= 8640 \times \sum_{k=m_i}^{\infty} P(k) \int_{\xi=\xi_i}^{\infty} PDF(\xi \geq \xi_i|k)d\xi,
 \end{aligned} \tag{7.3}$$

thanks to the chain rule in probability. Moreover, $P(k)$ is basically the Poisson PDF written before in equation 7.1 and 7.2.

Now, we need to understand the $PDF(\xi \geq \xi_i|k)$ in equation 7.3. This term represents the probability that a cluster with multiplicity k is characterized by a value ξ greater than or equal to ξ_i . First of all, we know for sure that the cluster multiplicity is never 0 inside this 20-second bin and ξ_{min} has a value of $k/\Delta t_{\text{max}} \rightarrow k/w \equiv k/20$, where $k \geq 2$. Thus, if we have a *background* cluster with multiplicity² k , we expect its ξ value to be close to $\xi_{\text{min}} \equiv k/w$, while a signal cluster should have $\xi \gg k/w$. Then, the PDF for pure background given a multiplicity k is basically $PDF(\xi \geq \xi_{\text{min}}|k)$, which is described as the black line in figure 6.7 Panel (a) for the distribution of ξ background-only. The normalised probability under this background curve for all possible ξ values is one, indeed. Therefore, for pure background-only, the integral in equation

²We need to remember that our multiplicity is running under summation from $k = m_i$ to $k = \infty$ (see equation 7.3).

Chapter 7. The Modified Imitation Frequency to Expand CCSN Search
Horizon of Neutrino Detectors

7.3 becomes $\int_{\xi=\xi_{\min}}^{\infty} PDF(\xi \geq \xi_{\min}|k)$ and the integration can be stated as,

$$\begin{aligned}
 1 &\equiv \int_{\xi=\xi_{\min}}^{\infty} PDF(\xi \geq \xi_{\min}|k) d\xi \\
 &= \int_{\xi_{\min}}^{\infty} N_k f(\xi) d\xi \\
 &= \int_{k/w}^{\infty} N_k f(\xi) d\xi \\
 &= N_k \int_{k/w}^{\infty} f(\xi) d\xi.
 \end{aligned} \tag{7.4}$$

Then, from equation 7.4, the normalization factor N_k can be written as,

$$N_k = \frac{1}{\int_{k/w}^{\infty} f(\xi) d\xi}. \tag{7.5}$$

Then, for the conditional probability (integral) in equation 7.3, we can write it as,

$$\begin{aligned}
 P(\xi|k) &= \int_{\xi \geq k/w}^{\infty} N_k f(\xi) d\xi \\
 &= 1 - \int_{k/w}^{\xi \geq k/w} N_k f(\xi) d\xi \\
 &= 1 - N_k \int_{k/w}^{\xi \geq k/w} f(\xi) d\xi \\
 &= 1 - \frac{\int_{k/w}^{\xi \geq k/w} f(\xi) d\xi}{\int_{k/w}^{\infty} f(\xi) d\xi},
 \end{aligned} \tag{7.6}$$

where the integration in the numerator always has this relation $\xi \geq k/w$, with w is the maximum duration, which is the window or bin width itself.

All in all, after considering equation 7.3 to 7.6, the new imitation frequency becomes,

Chapter 7. The Modified Imitation Frequency to Expand CCSN Search
Horizon of Neutrino Detectors

$$\begin{aligned}
F_i^{\text{im}}(w, m_i, \xi_i) &= 8640 \times \sum_{k=m_i}^{\infty} P(k) \left[1 - N_k \int_{k/w}^{\xi_i} f(\xi) d\xi \right] \\
&= f_i^{\text{im}}(w, m_i) - 8640 \times \sum_{k=m_i}^{\infty} P(k) N_k \int_{k/w}^{\xi_i} f(\xi) d\xi \\
&= f_i^{\text{im}}(w, m_i) - 8640 \times \sum_{k=m_i}^{m_i+n; n \leq (w \cdot \xi_i - m_i)} P(k) N_k \int_{k/w}^{\xi_i} f(\xi) d\xi,
\end{aligned} \tag{7.7}$$

Let us test this formula. Intuitively, we can say that when we have a pure background cluster with multiplicity m_{bkg} and $\xi_{\text{bkg}} = m_{\text{bkg}}/w$, the new imitation frequency should be very similar as the old one, namely,

$$F_{\text{bkg}}^{\text{im}}(w, m_{\text{bkg}}, \xi_{\text{bkg}}) \simeq f_{\text{bkg}}^{\text{im}}(w, m_{\text{bkg}}), \tag{7.8}$$

and when we have a very strong signal, with m_{strong} and ξ_{strong} ,

$$F_{\text{strong}}^{\text{im}}(w, m_{\text{strong}}, \xi_{\text{strong}}) \ll f_{\text{strong}}^{\text{im}}(w, m_{\text{strong}}). \tag{7.9}$$

We can prove those relations above. First, suppose that we found a cluster whose $\xi_i = \xi_{\text{min}} = m_i/w$, meaning that $n = 0$ for equation 7.7, and thus, our new imitation frequency becomes the old one,

$$\begin{aligned}
F_i^{\text{im}}(w, m_i, \xi_{\text{min}} = m_i/w) &= \left[f_i^{\text{im}} - 8640 \times \sum_{k=m_i}^{m_i+0} P(k) N_k \int_{k/w}^{m_i/w} f(\xi) d\xi \right] \\
&= \left[f_i^{\text{im}} - 8640 \times P(m_i) N_{m_i} \int_{m_i/w}^{m_i/w} f(\xi) d\xi \right] \\
&= f_i^{\text{im}}
\end{aligned} \tag{7.10}$$

meanwhile, even when ξ large, this condition that $N_k \int_{k/w}^{m_i/w} f(\xi) d\xi \leq 1$ is true, and,

Chapter 7. The Modified Imitation Frequency to Expand CCSN Search
Horizon of Neutrino Detectors

$$\begin{aligned}
F_i^{\text{im}}(w, m_i, \xi_{\text{large}}) &= f_i^{\text{im}}(w, m_i) - 8640 \times \sum_{k=m_i}^{m_i+n} P(k) N_k \int_{k/w}^{\xi_{\text{large}}} f(\xi) d\xi \\
&< f_i^{\text{im}}(w, m_i) - 8640 \times \sum_{k=m_i}^{m_i+n} P(k) \\
&< 8640 \times \sum_{k=m_i}^{\infty} P(k) - 8640 \times \sum_{k=m_i}^{m_i+n} P(k) \\
&< 8640 \times \left[\left(1 - \sum_{k=0}^{m_i-1} P(k) \right) - \sum_{k=m_i}^{m_i+n} P(k) \right] \\
&< 8640 \times \left(1 - \sum_{k=0}^{m_i+n} P(k) \right) \\
&< 8640 \times \left(\sum_{k=m_i+n+1}^{\infty} P(k) \right) = f_i^{\text{im}}(w, m_i + n + 1),
\end{aligned} \tag{7.11}$$

and when $n \gg$, this relation holds $f_i^{\text{im}}(w, m_i + n + 1) \ll f_i^{\text{im}}(w, m_i)$, and therefore,

$$\begin{aligned}
F_i^{\text{im}}(w, m_i, \xi_{\text{large}}) &< f_i^{\text{im}}(w, m_i + n + 1) \\
&\ll f_i^{\text{im}}(w, m_i)
\end{aligned} \tag{7.12}$$

Thus, we have proven the relations 7.8 and 7.9. ■

In brief, we have demonstrated a new way to estimate the significance of clusters in a neutrino data set to be,

$$F_i^{\text{im}}(w, m_i, \xi_i) = \left[f_i^{\text{im}}(w, m_i) - 8640 \times \sum_{k=m_i}^{m_i+n; n \leq (w \cdot \xi_i - m_i)} P(k) N_k \int_{k/w}^{\xi_i} f(\xi) d\xi \right] [\text{day}^{-1}]. \tag{7.13}$$

This new imitation frequency will work as long as we have a background distribution of $f(\xi)$ for each detector. The result of the thorough study of this ξ parameter has been presented with the title ‘‘Expanding Core-Collapse Supernova Search Horizon of Neutrino Detectors’’ in a TAUP2019 conference in Toyama, Japan [130], with the accepted proceeding can be seen in [129].

All in all, we have known previously that the ξ background follows a 4-parameter Gamma distribution from chapter 6 and reference [119]. However, with our new imitation frequency in equation 7.13, we do not actually need any distribution fit. Moreover, we will also discuss later that 4-parameter Gamma distribution may not be the best choice.

7.2 Comments on the ξ -background Distribution

In reference [119] as well as chapter 6, it has been observed that a simulated data set consisting of only background noise has a probability density function (PDF) of 4-parameter Gamma distribution for each single detector. We scrutinise the fit again and it turns out that Gamma distribution may not be precise to explain the ξ distribution (see figure 7.1). Basically, there are 3 distributions that we study:

1. Gamma distribution [131]: here, the gamma distribution involves Gamma function, with the PDF,

$$y = f(x|a, b) = \frac{1}{b^a \Gamma(a)} x^{(a-1)} e^{-\frac{x}{b}}, \quad (7.14)$$

where a is a shape parameter, b is a scale parameter, and $\Gamma(a)$ is the Gamma function.

2. Generalized extreme value distribution [132] with location parameter μ , scale parameter σ , and shape parameter $k \neq 0$, and the PDF,

$$y = f(x|k, \mu, \sigma) = \left(\frac{1}{\sigma}\right) \exp\left(-\left(1 + k\frac{(x-\mu)}{\sigma}\right)^{-\frac{1}{k}}\right) \left(1 + k\frac{(x-\mu)}{\sigma}\right)^{-1-\frac{1}{k}}, \quad (7.15)$$

for $1 + k\frac{(x-\mu)}{\sigma} > 0$. $k > 0$ corresponds to the Type II case, while $k < 0$ corresponds to the Type III case. For $k = 0$, corresponding to the Type I

case, the PDF is,

$$y = f(x|0, \mu, \sigma) = \left(\frac{1}{\sigma}\right) \exp\left(-\exp\left(-\frac{(x-\mu)}{\sigma}\right) - \frac{(x-\mu)}{\sigma}\right). \quad (7.16)$$

3. Burr type XII distribution [133], instead, has a PDF,

$$y = f(x|\alpha, c, k) = \frac{\frac{kc}{\alpha} \left(\frac{x}{\alpha}\right)^{c-1}}{\left(1 + \left(\frac{x}{\alpha}\right)^c\right)^{k+1}}, \quad (7.17)$$

where $x > 0$, $\alpha > 0$, $c > 0$, and $k > 0$. Moreover, its cumulative distribution function,

$$F(x|\alpha, c, k) = 1 - \frac{1}{\left(1 + \left(\frac{x}{\alpha}\right)^c\right)^k}. \quad (7.18)$$

We fit the ξ -background distribution with those distributions above in figure 7.1 and we can see from the figure that instead, generalized extreme value distribution (GEV [132]) or Burr type XII distribution [133] could fit better than gamma distribution, at least when we compare their residuals. When we check the *goodness-of-fits* (GoF³) as well as its p -values of the distribution fits, it also shows that Burr type XII distribution gives the best fit with p -value of 3×10^{-26} . However, we cannot explain any physical meaning of the relation between this Burr (or GEV) distribution and our data.

From here, we realize that this ξ background distribution could be somewhat complex due to the fact that the distribution of the number of background events in a cluster follows Poisson distribution, while the distribution of duration from a background cluster is somewhat unclear. In any case, basically the background ξ distribution follows a certain distribution that may be 4-parameter Gamma, generalized extreme value [132], Burr type XII [133], or any other distributions. Therefore, rather than doing *trial-and-error* to fit a bunch of possible distributions to our simulated data, in order to be generic, we will not use any distribution, instead we rely on the **interpolation** of the ξ

³GoF=1 as well as lower p -value mean the distribution is fitted well. As an example, if p -value = $5.7 \cdot 10^{-7} = 5\sigma$ means that the fit is compatible in 5σ level.

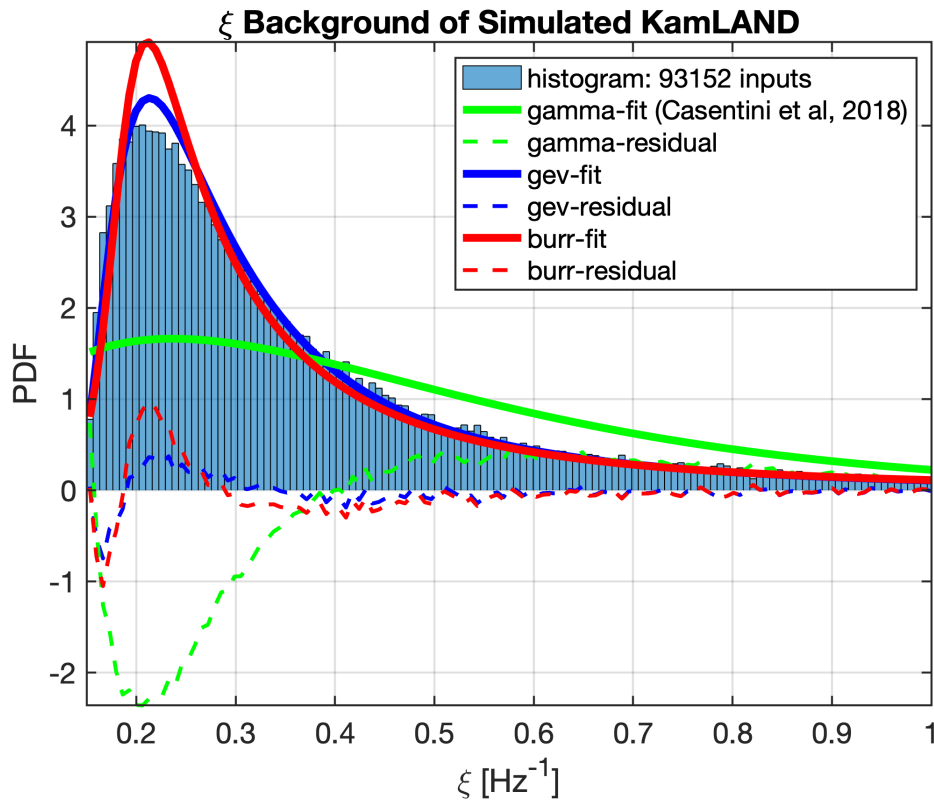


FIGURE 7.1: PDF histogram of simulated KamLAND data. The histogram has been fitted with several possible distributions such as 4-parameter Gamma distribution (like in chapter 6 and reference [119]), generalized extreme value distribution [132], as well as Burr distribution [133]. It has been also shown the residuals.

background. Another advantage of this interpolation is that it is adaptive. The background distribution can be estimated using the real data of the detectors, including background fluctuations that can happen in some given periods of data taking. We can look at figure 7.2, where the histogram is interpolated (with the residual), unlike figure 7.1 using fitting.

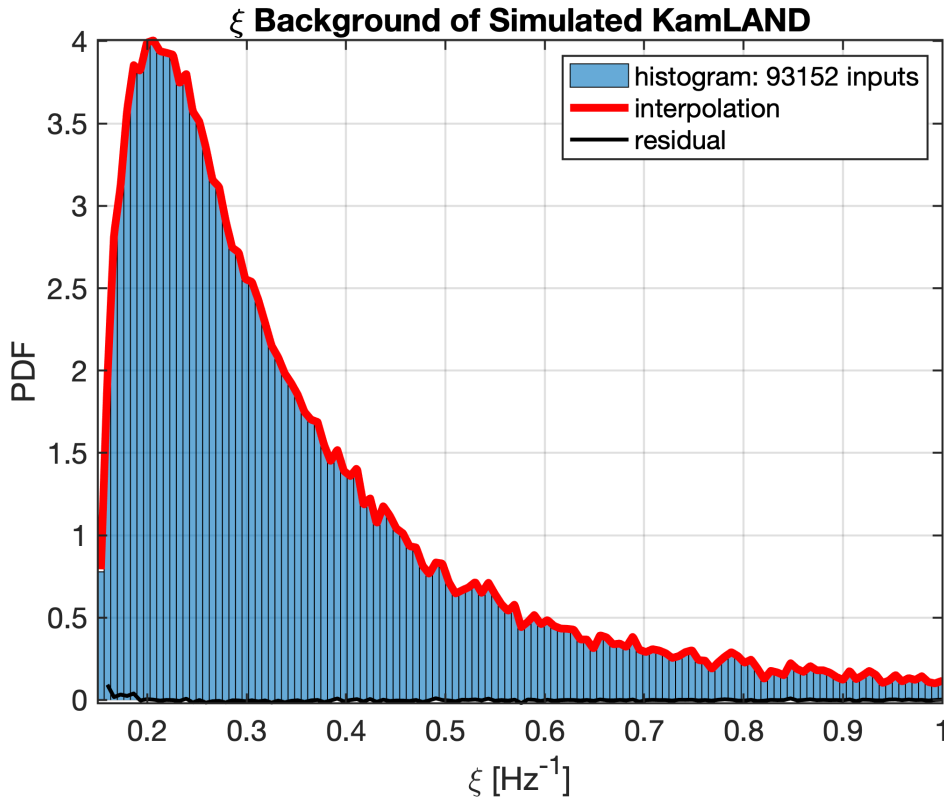


FIGURE 7.2: PDF histogram of simulated KamLAND data with the interpolation and its residual of the histogram. The histogram is the same as in figure 7.1, on the other hand here we use the interpolation method, unlike figure 7.1, which is by fitting. The area under curve is basically: $\int_{\xi=\xi_{\min}}^{\infty} PDF(\xi \geq \xi_{\min}|k) d\xi = 1$. In the tail of the interpolation for high ξ , there is some "wiggle" that is due to the lower number of counts in the histogram bin, which is related with Poisson uncertainty.

7.3 Application of the Modified Imitation Frequency to Simulated Data

Based on the recipe in the previous section, here, we apply the method to the simulated data used in [119]. We basically use the models for simulated background and injections used in chapter 6 and reference [119]. We reanalyse some of the data sets such as LVD, KamLAND, and Super-K data sets. We also add a new future detector, namely Hyper-Kamiokande (Hyper-K) [38]. The detail of the involved detector models can be seen in table 7.1. In the table, we give details on the detector types (liquid scintillator and water Cherenkov, see further in chapter 3 as well as reference [61, 62]), the main

interaction (IBD, see chapter 6), detector masses, background frequency, and energy thresholds. Moreover, the expected average multiplicity as a function of distance for the involved detectors can be seen in figure 7.3. Super-K detector could still be able to gather about 2 low-energy neutrino events from a CCSN in Andromeda (M31), while KamLAND and LVD can gather 8 events from a CCSN in Small Magellanic Cloud, and indeed all detectors are able in principle to see CCSNe in the Milky Way.

TABLE 7.1: Simulation details of some detector models. Here, there are two types: liquid scintillator and water Cherenkov. The main detection channels is the $\bar{\nu}_e$ from IBD. It is also provided the mass, background frequency f_{bkg} , as well as energy threshold E_{thr} .

	Detectors			
	LVD	KamLAND	Super-K	Hyper-K
Type	Liq. Scintill.	Liq. Scintill.	H ₂ O Cher.	H ₂ O Cher.
Main Channel	IBD, $\bar{\nu}_e$	IBD, $\bar{\nu}_e$	IBD, $\bar{\nu}_e$	IBD, $\bar{\nu}_e$
Mass	1 kton	1 kton	22 kton	187 kton (per module)
f_{bkg}	0.028 Hz	0.015 Hz	0.012 Hz	≈ 0.012 Hz (assumed)
E_{thr}	10 MeV	1 MeV	7 MeV	4.5 MeV

Moreover, in our data we decide a threshold as low as possible to see the possible outcome of this new method. The idea is to use multiplicity threshold of 2. This is due to the fact that when there is a neutrino burst from Andromeda galaxy, the expected multiplicity gathered by Super-K is of the order of 2 (see chapter 3 and reference [64]). We will not push to have multiplicity lower than 2 since the number of background clusters will explode.

First, we do the single detector analysis for KamLAND data set with injections for 65 kpc. We study this distance because we expect that the efficiency is not 100% with the standard method, based on the details of the detector in table 7.1. Then, we compare the performance in terms of efficiency

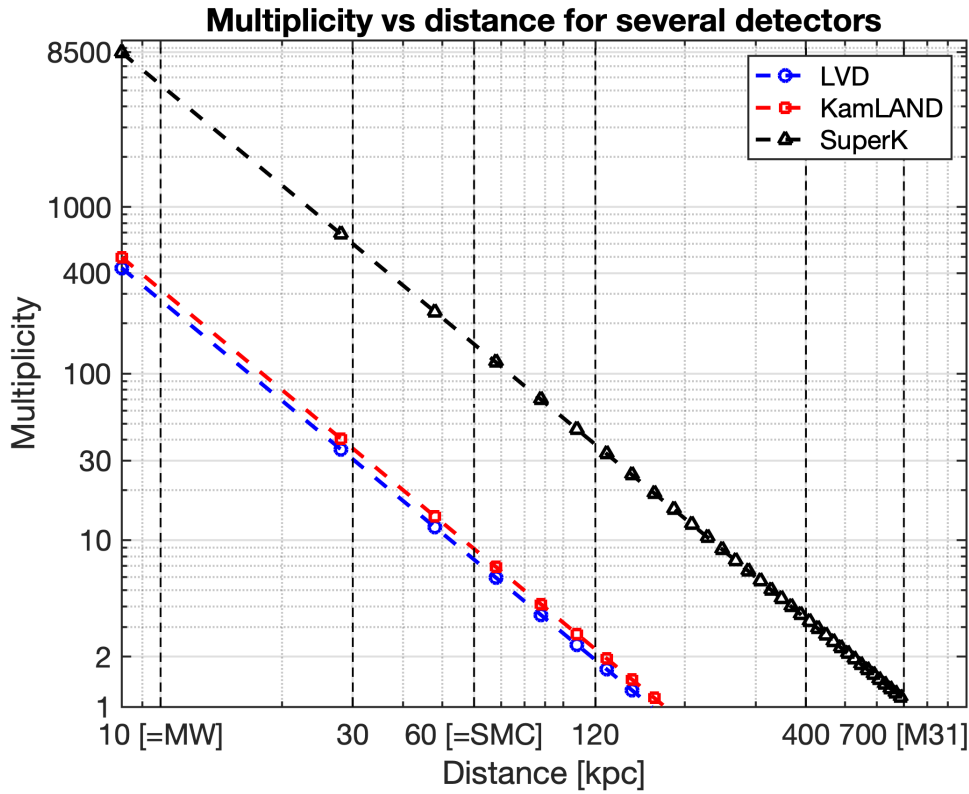


FIGURE 7.3: The expected multiplicity as a function of distance for the involved detectors. Here, we can see that Super-K could detect $\lesssim 2$ low-energy neutrino events from a CCSN in Andromeda, while KamLAND and LVD can gather about 8 events from a CCSN happening in Small Magellanic Cloud. Moreover, all detectors are able to see CCSNe in the Milky Way.

and misidentification probability of our 2-parameter method with the standard 1-parameter method. The calculation of the imitation frequency with the 2-parameter method follows equation 7.13, while the 1-parameter standard method follows equation 6.13. Then, we check the clusters which are due to background and injections.

We also do a network analysis by combining our simulated data of LVD and KamLAND with injections for 65 kpc. Indeed the time-coincidence analysis, explained in chapter 5, is used for this network. We use the coincidence window $w = 10$ seconds in this case. When we find several coincident clusters that are basically due to the same source (all of them separated⁴ < 20 seconds), either due to background or injection, we make a ranking in multiplicity for

⁴This 20 second is actually due to the size of the bin, which is 20 seconds.

each detector data and take the pair of clusters from 2 different detectors with highest multiplicity m_i , and if still there are several coincidences, we make another ranking with ξ and take the highest ξ . Then, we check the coincident clusters whether they are due to injections or background. The coincident clusters that are due to injections are called the **observed injections**. Next, we calculate the old (and new) jointFAR based on individual f_i^{im} (and F_i^{im}) for each 0-lag coincidence following equation 5.25 and 5.26, respectively, to get the jointFAP, which is basically the significance value.

In our next discussions, we will show our findings for the single detector analysis. Then, we will move on to the result of the network of two data sets. Last but not least, we will also consider a possible future detector study, namely Hyper-K, and we will discuss its detection capability with our 2-parameter method.

7.4 KamLAND Single Detector Analysis Result

Here we will discuss our findings on the 1-detector analysis of simulated KamLAND data. In this case, we use KamLAND as our model with a background frequency of 0.015 Hz (table 7.1). As the first step to give the idea of the improvement of this new method, we plot the ξ - m map in figure 7.4. In the figure, the green-shaded area is the region of the plane including the (ξ_i, m_i) clusters with standard imitation frequencies f_i^{im} 's (equation 6.13) above the SNEWS (chapter 4) threshold of 1/100 years. On the other hand, the red-shaded area is the region selecting the clusters passing the SNEWS threshold with our 2-parameter F_i^{im} (equation 7.13), but not passing the threshold with standard f_i^{im} . We can also say that this red-shaded area is the improvement by using our method.

If using the standard 1-parameter method, the minimum multiplicity is 8 to pass SNEWS threshold, which is **equivalent to the average expected number of events for a distance of 65 kpc (Small Magellanic Cloud)**. Meanwhile,

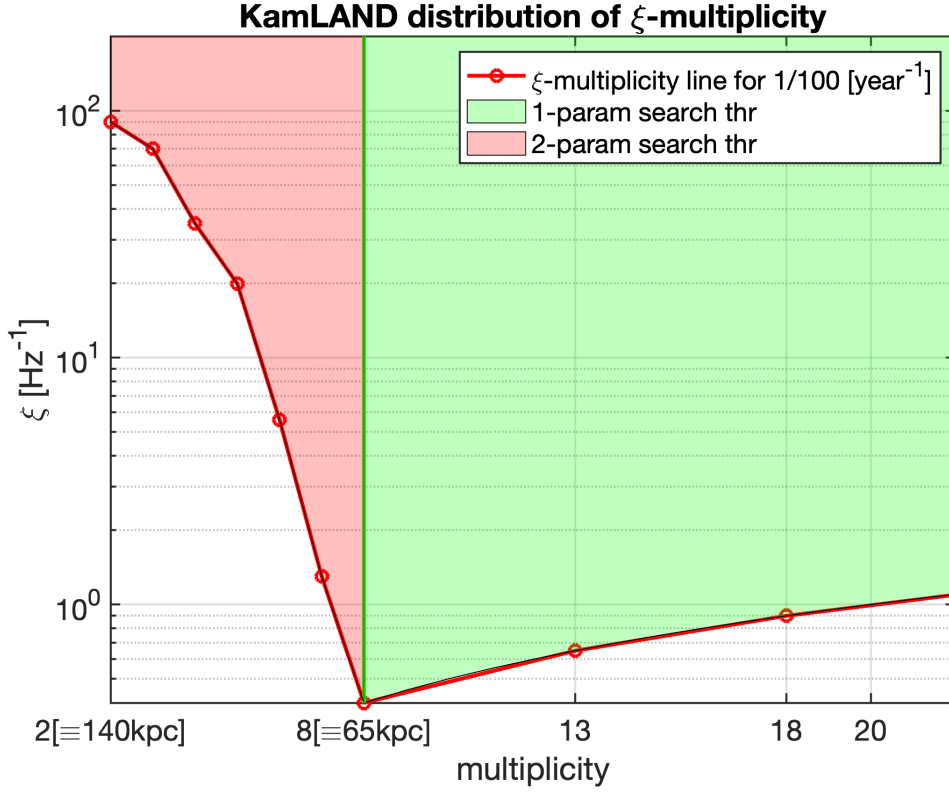


FIGURE 7.4: KamLAND ξ -multiplicity map. The green-shaded area passes 1/100-year threshold for standard f^{im} , while the red-shaded area is the improvement by using 2-parameter method (this work). The total (red + green) area passes the threshold with the 2-parameter F^{im} .

if we include 2 parameters (ξ and multiplicity) in our analysis, we can basically take clusters having multiplicity less than 8 as long as the combination of $\xi_i - m_i$ value gives us F^{im} less than equal to 1/100-year threshold.

Next, we add the background clusters in $\xi_i - m_i$ map to see if the misidentification probability is increased with the new method. We can see this in figure 7.5 where the yellow-reversed triangles are denoted as background clusters. As we can see, the background clusters are all below the SNEWS threshold whether for the 1-parameter and 2-parameter method. This means that the 2-parameter calculation does not add noise.

Moreover, we also include the 65-kpc injections inside this $\xi_i - m_i$ plane in figure 7.6 with the blue stars as the recovered injections. The distribution of recovered injections in terms of multiplicity is quite broad, spanning from $m_i = 3$ up to $m_i \gtrsim 20$, so does their ξ values, which are from $\xi_i < 1$ to

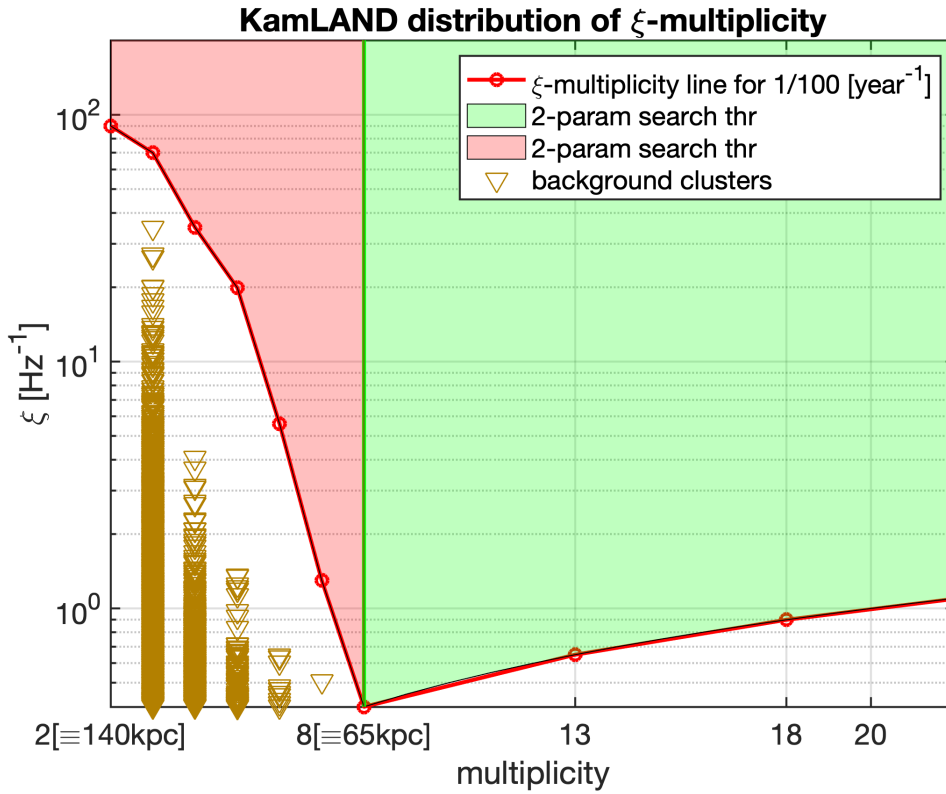


FIGURE 7.5: KamLAND ξ -multiplicity map, the same as figure 7.4 but with the addition of 10-year simulated background.

$\xi_i \sim O(100)$. The important insight here is that there are some injections lying on the red-shaded area. This means that they are recovered by our two-parameter method, but missed in the standard one-parameter method. To have a better quantitative idea, we provide the detail of this finding in table 7.2, where the first column is the total number of background clusters in 10-year data chunk, the second column is the background clusters passing SNEWS threshold, the third column is the clusters passing the 1-parameter method per total injections, while the last column is the recovered injections per total injections passing our proposed method. The efficiency improves in the order of 10% with our new method from 59% to 71% without adding any noise.

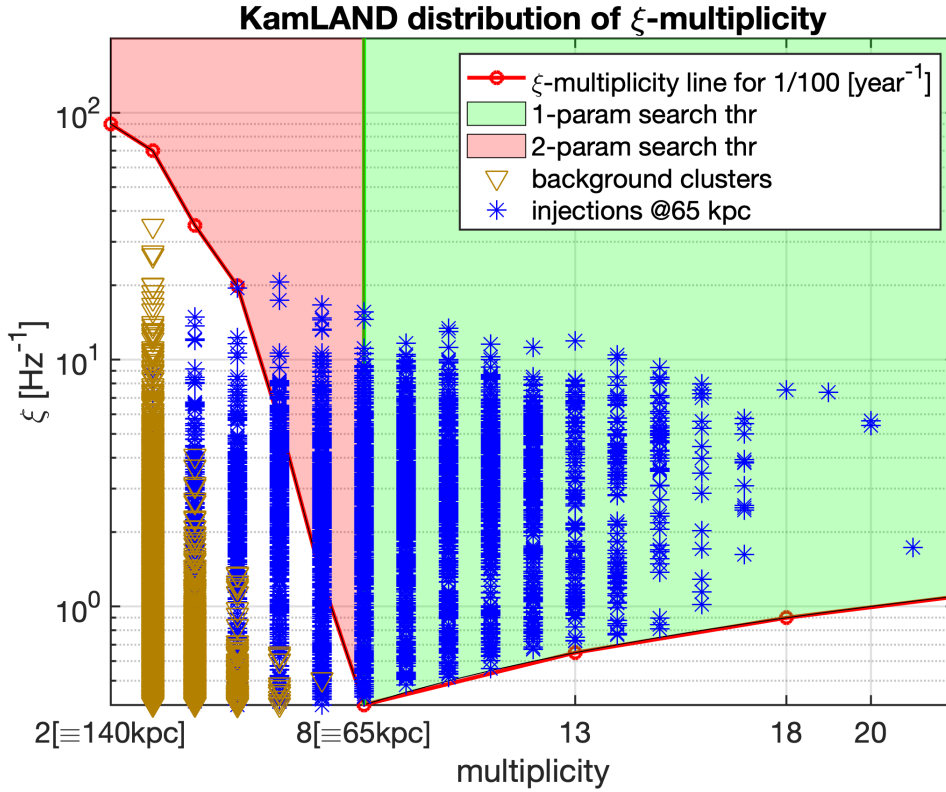


FIGURE 7.6: KamLAND ξ -multiplicity map, the same as figure 7.5 with the addition of 65-kpc injections. This figure is presented in [129].

TABLE 7.2: Single detector KamLAND analysis with 65-kpc injections. The data set is 10-year long. See text for the explanation.

Total	Background	1-parameter	2-parameter (this work)
Background	[< 1/100 years]	[< 1/100 years]	[< 1/100 years]
75198	0% = 0/75198	59.0% = 2155/3654	70.6% = 2581/3654

7.5 Super-K Single Detector Analysis Result

Besides KamLAND single detector analysis, we will also discuss the result of Super-K single analysis. The plot can be seen in 7.7. Analogously to the KamLAND single detector result, the Super-K result also shows that there are some more recovered injections (the quantitative result can be seen in table 7.3). However in Super-K, the threshold of 1/100 years with the 1-parameter f^{im} (equation 6.13) lies on the multiplicity = 8, that corresponds to the average expected number of events for a CCSN located at a distance of 260 kpc. Clearly

this distance is in between Small Magellanic Cloud and Andromeda, which is lack of interesting galaxies and we do not expect CCSNe happening here, however we include this case in order to demonstrate the method.

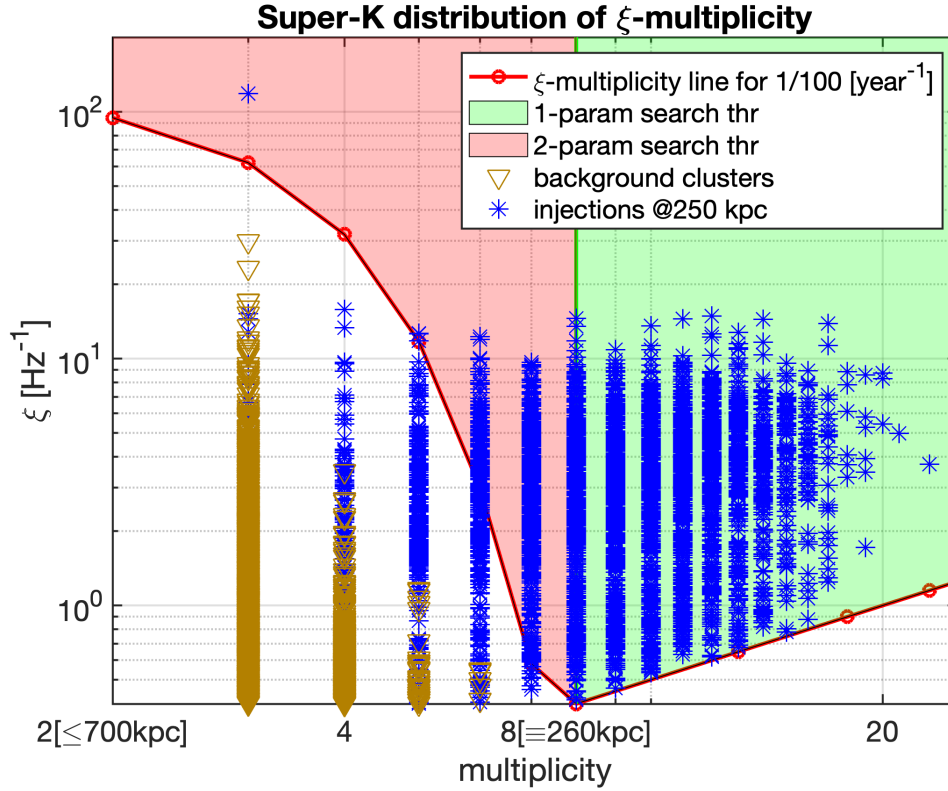


FIGURE 7.7: Super-K ξ -multiplicity map with the 250-kpc injections.

TABLE 7.3: Single detector Super-K analysis with 250-kpc injections. The data set is 10-year long. See text for the explanation.

Total	Background	1-parameter	2-parameter (this work)
Background	[< 1/100 years]	[< 1/100 years]	[< 1/100 years]
49200	0% = 0/49200	70.6% = 2575/3645	85.5% = 3117/3645

With our 2-parameter F^{im} (equation 7.13) we cannot gain the search by Super-K since the horizon is well beyond Small Magellanic Cloud, but well too near to reach Andromeda. The efficiency search for Super-K to find CCSNe in the distance up to Small Magellanic Cloud already reaches 100% (see figure 7.8), while the efficiency search in Andromeda (~ 700 kpc) is practically 0%

(see figure 7.9). However, we may still be able to benefit from this 2-parameter method to search for failed-supernovae up to Small Magellanic Cloud (~ 60 kpc), assuming that the expected multiplicity from those objects may be lower than the normal CCSNe. Nevertheless, we need to study deeper this point and this will be beyond the scope of our work for the moment.

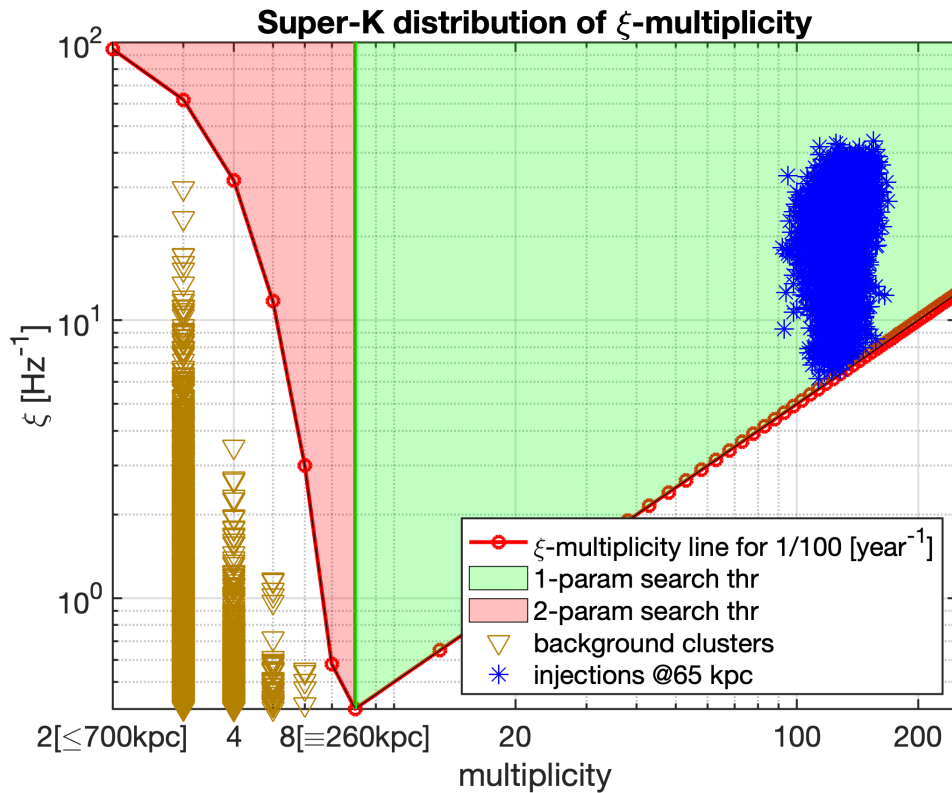


FIGURE 7.8: Super-K ξ -multiplicity map with the 65-kpc injections.

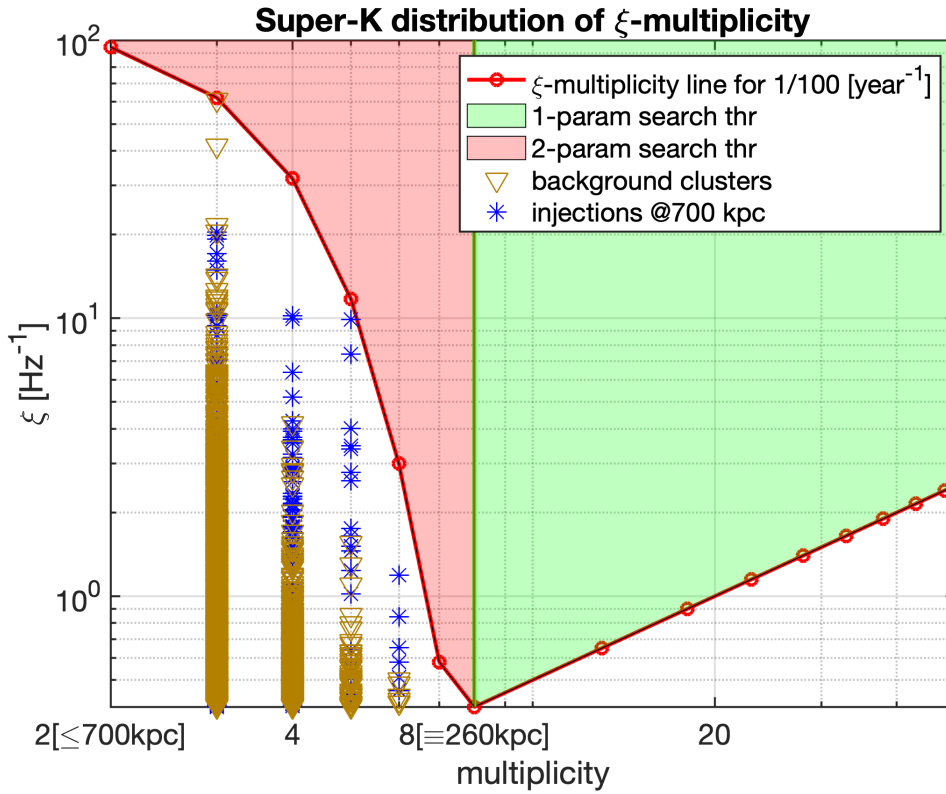


FIGURE 7.9: Super-K ξ -multiplicity map with the 700-kpc injections.

7.6 KamLAND-LVD Coincidence Analysis Result

In this section, we will analyse the network of detectors. We combine two simulated data sets of KamLAND and LVD by implementing the coincidence analysis (chapter 5) to see the improvement of our method. We use 65-kpc injections in those two data sets. As the first step, we would like to see the joint distribution of ξ of background coincident clusters as well as of recovered coincidences. We plot the 3D histogram in figure 7.10 of ξ distribution for background clusters and in figure 7.11 for the recovered injections. We can see from those figures that the accidental coincidences tend to have lower ξ values comparing with the 65-kpc injections⁵. This is expected since the higher the ξ value, the more probable it is due to a signal, which is basically consistent also with figure 6.7 Panel (a).

⁵This was the reason for which in reference [119] as well as chapter 6, the ξ parameter was used as a cut.

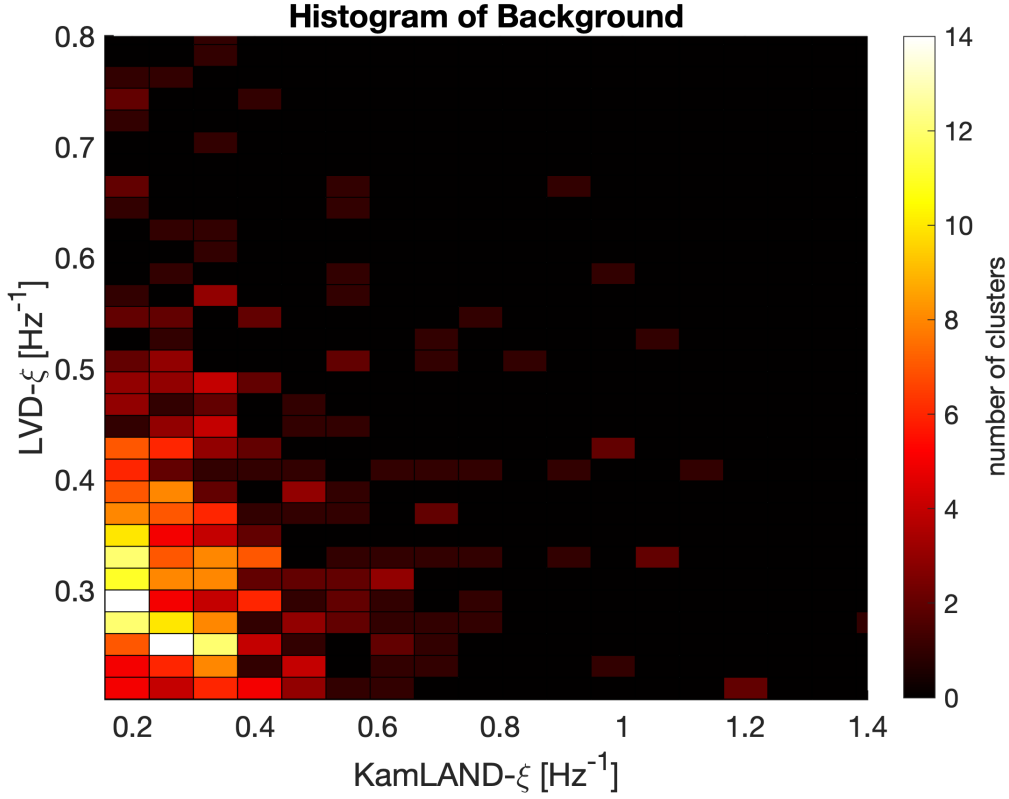


FIGURE 7.10: 3D histogram of the ξ distribution of the accidental coincidences between the simulated-10-year KamLAND and LVD data.

Next, we calculate the efficiency η and misidentification probability ζ discussed previously in chapter 6. However, we distinguish deeper the η and ζ since the previous chapter does not mention any significance in the efficiency and misidentification probability calculation. Meanwhile, here, we work on calculating the new significance (as F^{im}) in the analysis. Thus, we define raw efficiency/misidentification probability and 5σ efficiency/misidentification probability. In this case, the *raw* means that we count only the coincidences without taking into account the significance like in chapter 6 and reference [119], meanwhile the 5σ is when we give a 5σ threshold for the coincidences. This 5σ is different from SNEWS threshold. For SNEWS threshold, it is imposed to the imitation frequency, while for 5σ , the threshold is on jointFAP in equation 5.26, in which,

$$5\sigma \equiv 5.7 \times 10^{-7} = \text{jointFAP}_{\text{thr}}, \quad (7.19)$$

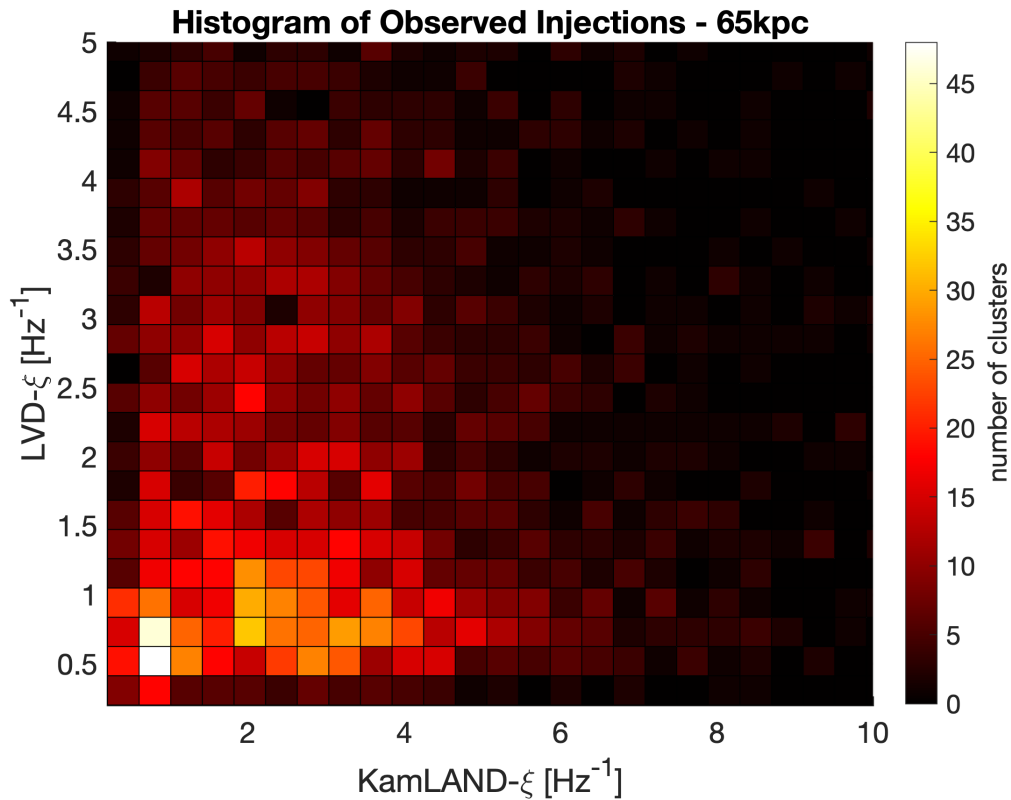


FIGURE 7.11: Same as figure 7.10 but with the observed injections in 65kpc.

where jointFAP is the equation 5.26. Passing the 5σ threshold means that all the coincidences must have $\text{jointFAP} \leq 5.7 \times 10^{-7}$.

In our 10-year data, we have 3654 injections and 3872 total coincidences⁶. We can see our findings in table 7.4. The 5σ efficiency increases of almost 20% with our new 2-parameter method. We need also to remember that this is the efficiency for the distance up to Small Magellanic Cloud (65-kpc), which is not 100% for LVD and KamLAND. Moreover, there is no noise with larger than 5σ signal.

⁶background + the observed injections.

TABLE 7.4: Efficiency η and misidentification probability ζ for KamLAND-LVD 10 year - 65 kpc.

2-detector: LVD - KamLAND	10 year - 65 kpc	
	Old Method	New Method
Raw η	93.7% = 3425/3654	
Raw ζ	11.5% = 447/3872	
5σ η	62.9% = 2298/3654	80.8% = 2951/3654
5σ ζ	0% = 0/3872	0% = 0/3872

7.7 One-module Hyper-K

Besides the current detectors, we are also considering the improvement of the future detector with our 2-parameter method. As an example here we consider the one-module Hyper-K [38], with the detail in table 7.1. We assume here that the background frequency of Hyper-K will be of the same level as the one of the Super-K. Based on this assumption, if there is a CCSN in ~ 700 kpc (M31/Andromeda) galaxy, we expect to gather multiplicity of the order of 7 events in the Hyper-K detector. Similarly as the previous sections, we then plot the background, injections, as well as the 1/100-year threshold line in ξ_i - m_i map in figure 7.12. The improvement can be seen in table 7.5, the efficiency to detect CCSNe for a distance of 700 kpc improves about 15%.

TABLE 7.5: One-module Hyper-K with 700-kpc injections.

Total Background	Background [< 1/100 years]	1-parameter [< 1/100 years]	2-parameter (this work) [< 1/100 years]
49203	0% = 0/49203	70.4% = 2575/3655	85.4% = 3120/3655

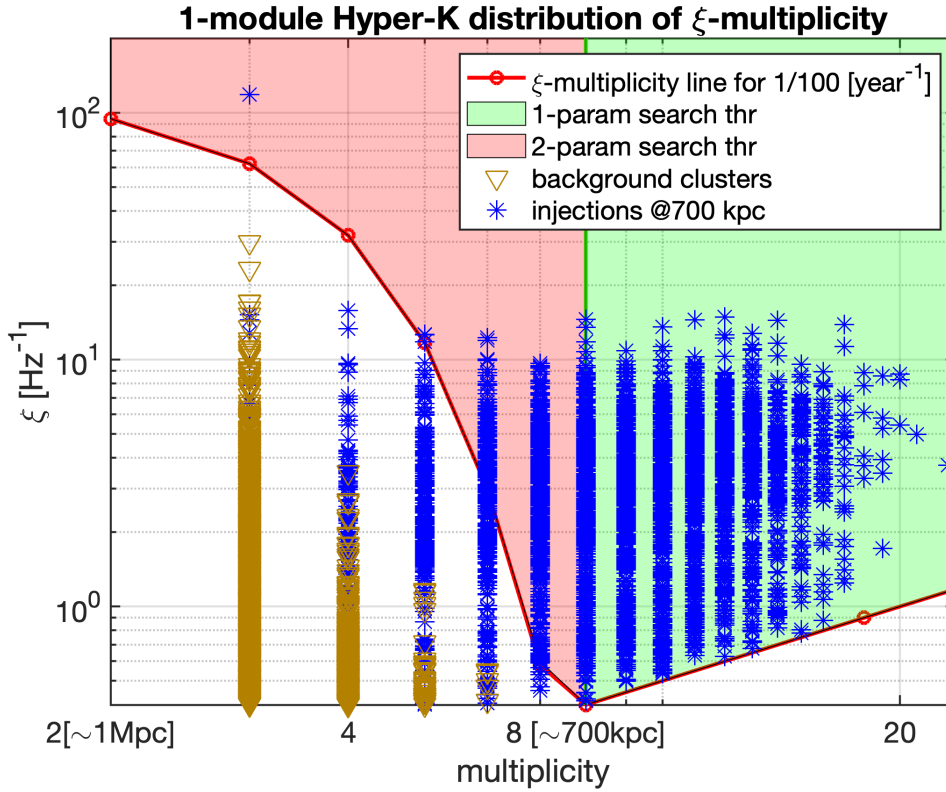


FIGURE 7.12: Hyper-K ξ -multiplicity map with 10-year simulated background and 700-kpc injections.

7.8 Perspectives

We have seen that our 2-parameter method applied in neutrino data may enhance the significance of each injected cluster, so does increase the detection efficiency as well as the horizon, without increasing the misidentification probability. Moreover, our method can simply be applied in terms of a single neutrino detector data set as well as in a network of several neutrino detector data. This is important to be implemented in SNEWS2.0. Our analysis basically has several advantages such as,

1. it is very sensitive to low-statistical signals (far/weak),
2. it is fast, can be implemented for online search with very low latency ,
3. it is adaptive, indeed the background distribution can be estimated using the real data of the detectors, including background fluctuations,

4. it is pretty model-independent, the double exponential model for the neutrino emission from CCSNe is very basic but is enough for low-statistic signals,
5. it only needs minimal information; no need for a complete data sharing among different experiments.

On the other hand, if we use unbinned likelihood method, the analysis is theoretically slower and we also need a complete data sharing.

Based on the results in this chapter and its discussion (as well as our result presented in reference [129]) until now, we can see that there are quite interesting insights that we have found. Those several points can be remarked as,

1. This method can disentangle better the single-detector analysis and give us a better statistical significance calculation. Besides, it is also a one-step further improvement than our previous result in chapter 6 and reference [119].
 - (a) The SNEWS-threshold efficiency of the 65-kpc simulated KamLAND increases from 59.0% to 70.6% without adding any noise.
 - (b) There is also improvement of 5sigma efficiency for 2-detector analysis up to Small Magellanic Cloud for current detectors, where simulated 65-kpc LVD-KamLAND efficiency increases from 62.9% to 80.8%.
2. JUNO-Super-K network may work like LVD-KamLAND.
3. This method could be also useful to enhance the future detectors (Hyper-K) to *expand* the CCSN search horizon in order to reach M31 / Andromeda.
4. Two-module Hyper-K can work as a network to reach ~ 1 Mpc.

Moreover, we also should think of the near future work that can be done. We consider that it is possible to apply the offline analysis of our method for **failed-SN search** by Super-K till Large (Small) Magellanic Cloud together

*Chapter 7. The Modified Imitation Frequency to Expand CCSN Search
Horizon of Neutrino Detectors*

with GWs. This is due to the fact that we expect the failed-SN duration should be smaller than the normal CCSNe (~ 0.5 seconds vs ~ 20 seconds). To be conservative, we may also *assume* that the multiplicity be smaller than the normal CCSNe. In this case, our new method may play a role. Fortunately for us, the multiplicity of failed-SN can be similar to the one of the CCSNe (see reference [66]). Combining this multiplicity with the ~ 0.5 -second duration, the ξ value will soar, therefore, our method may produce even a higher efficiency search.

Chapter 8

GW- ν Joint Search

The expansion of the search horizons discussed in the previous chapter by using our proposed method may enable us a more efficient multimessenger analysis via LENSs and GWs. In fact, the first quantitative study of the possibility to use a neutrino burst has been discussed in [134] and this work motivated us to start this activity. Besides, there are also several multimessenger analyses reported in chapter 4, i.e. the GW-GRB and the GW-HEN search. However the way to statistically combine LENSs and GWs is very different from those analyses chapter 4. In particular, in both these analyses one of the two signals combined is considered as a detection and the statistics of GWs and GRBs or HENSs are not combined. Meanwhile, in our case this combination of statistical significance between LENS bursts and GW bursts is needed because both the signals could be sub-threshold.

One possibility discussed in chapter 5 is to use the product method to find the significance of a joint LENS-GW detection. Thanks to the work discussed in chapter 7, we are now able to provide a FAR for the neutrino burst that takes into account also the new selection criteria based on the temporal shape of the expected signal (the ξ parameter) and then we can apply the product method without losing information. Gravitational wave triggers produced by the `cWB` pipeline, are characterized by FARs. Additionally, of course, the GW livetime (see chapter 3) for each data taking period is provided. Thus, we have all the required information for the coincidence analysis with product method to work.

This method is chosen because we are not bound to find the common statistics between neutrino and GW data. More importantly, the coincidence window between the neutrino list and GW list could be large (of the order of ~ 10 seconds¹), which means we require a year-long common data taking period among the involved detectors, in order to use time-shifting method like in `cWB` pipeline for GW analysis, to get 5σ significance of a signal. Else, we can only give the lower limit of significance, and this lower limit can be much less than 5σ needed to a detection, when we have a very short-lifetime data chunks among detectors (see more detail in chapter 5).

The scheme followed for the GWnu joint search can be seen in more detail in the figure 8.1 below. First, we analyse separately the data of the GW network and of the neutrino network. We use `cWB` pipeline to search for possible GW triggers. Each GW trigger is parametrized by some quantities such as the trigger time, duration, GW statistic, and significance (FAR). Among these parameters, we only need to know the time and FAR of each trigger as well as the common observing time (livetime) to do the coincidence analysis with the product method. Second, we analyse neutrino data from each neutrino detector with our proposed method with the addition of the new parameter following chapter 7. From each detector data set, we produce a list of candidates (or triggers) with the information of time and FAR. Then, the other neutrino data sets are analysed analogously. From the various lists of neutrino triggers, we do coincidence analysis with the product method. This generates the joint list of the neutrino detector data network.

Thus, we have two lists of potential detected signals both from GW and neutrino channel. These two lists are analysed further via coincidence analysis with the product method, in principle the coincidence window used in this last step could be different from the one used to search coincidences among neutrino detectors. In the end, we will have the final joint triggers of $GW-\nu$ network. In the future, we should be able to produce the triggers of neutrino detector data network in low latency thanks to the SNEWS2.0 infrastructure.

¹Meanwhile, the coincidence window in `cWB` is of the order of milliseconds.

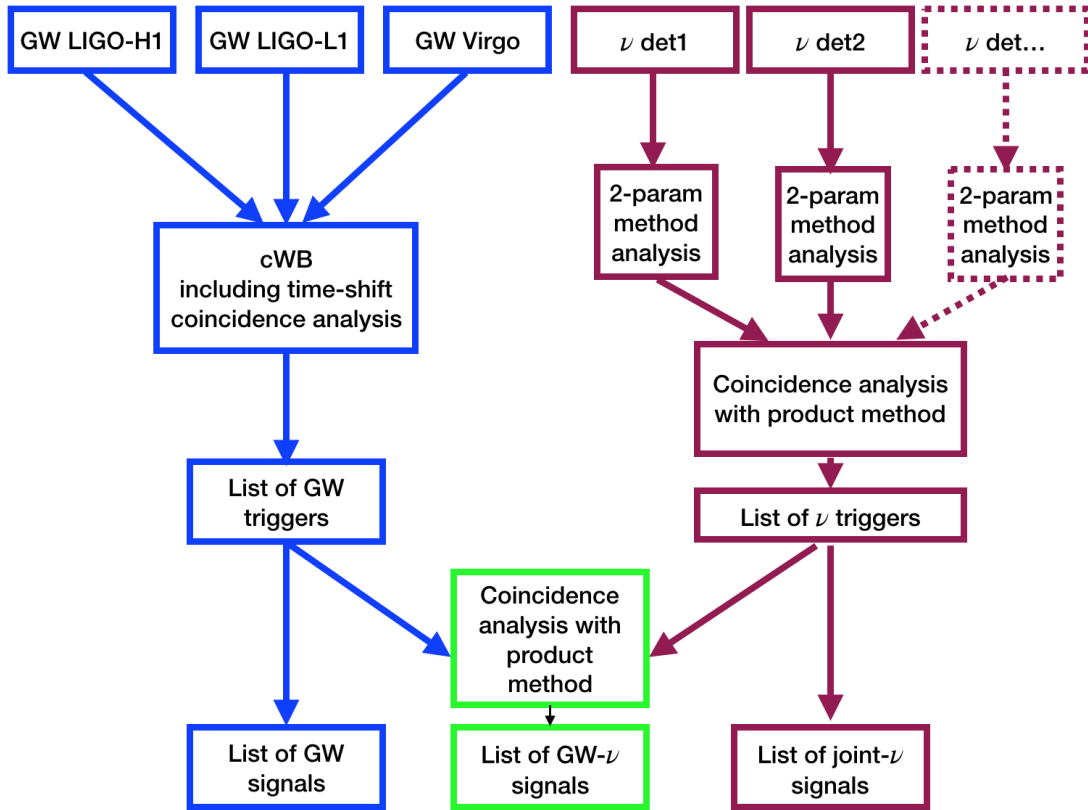


FIGURE 8.1: Scheme of the method for the joint GW-neutrino analysis to search for CCSNe. We use the cWB pipeline with its default/standard configuration. Meanwhile, we use 2-parameter method for each neutrino detector data analysis (chapter 7). We combine the neutrino data with the coincidence analysis with product method (chapter 5). We combine the list of GWs and neutrinos together in terms of multimessenger via product-method coincidence analysis (chapter 5). The final result will be 3 lists: 1 list of joint GW-neutrino signal signals, 1 list of GW signals from cWB , and 1 list of joint neutrino network signals.

Our method in analysing neutrino data should be easily implemented in the SNEWS analysis pipeline.

8.1 Joint $GW-\nu$ Study Case

We have made a study case for this multimessenger search by using the publicly available “observing-run-one” (O1) GW data as well as our injection data used in chapter 6 and 7. This O1 data spans from September 2015 to January 2016 with the data type:

- L1:DCS-CALIB_STRAIN_C02 from LIGO Livingston, and

- H1:DCS-CALIB_STRAIN_C02 from LIGO Hanford.

Our idea for doing this is to answer a question: “What if *all* our neutrino coincident LVD-KamLAND candidates are also in coincidence with GW triggers (meaning that they are triple coincidences)? What will be the significance of those triple coincidences when we use the standard 1-parameter neutrino analysis method comparing with our new 2-parameter method (explained in chapter 7)?”

Therefore, we add some signal injections by using the `cWB` pipeline with Gaussian, sine-Gaussian, as well as white-noise-burst models. The efficiency curve of different signal models in `cWB` can be seen in figure 8.2.

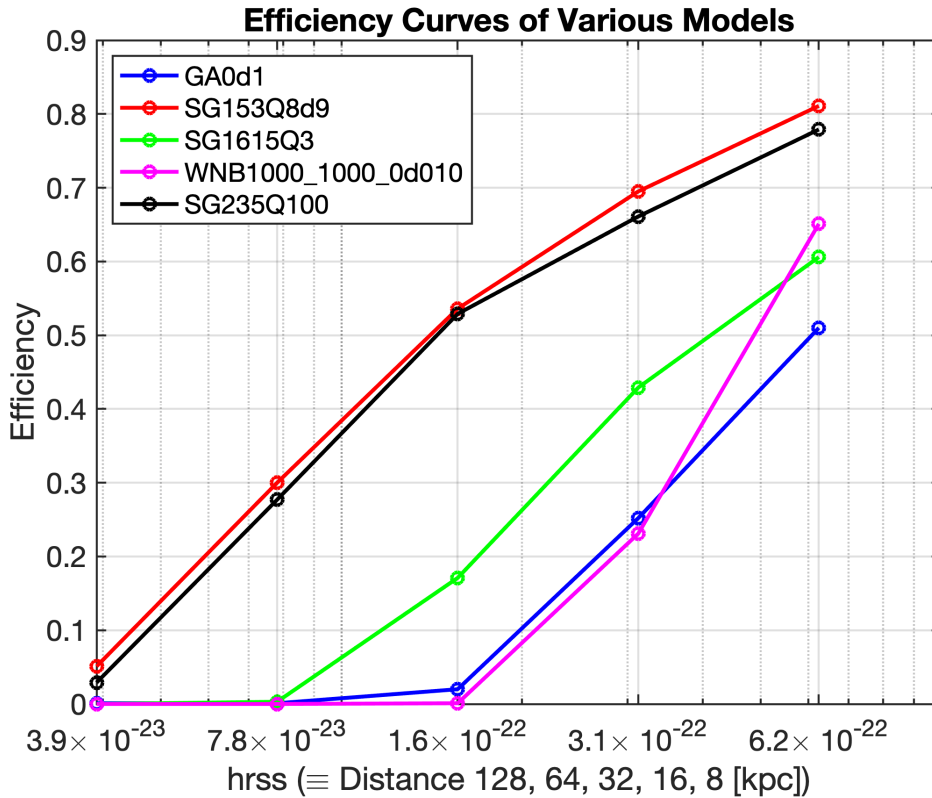


FIGURE 8.2: The efficiency curve from `cWB` of several injection models: Gaussian, sine-Gaussian, and white-noise-burst.

The neutrino injection times are set in such a way to have coherent injection times with the GW simulated signals that we use. In this case, we use neutrino injected signals with LVD and KamLand detector model. Then, we

do the neutrino analysis with 1-parameter method and 2-parameter method following our previous several chapters. The livetime for double-neutrino LVD-KamLAND data analysis is of the order of 4 months, while the livetime for triple LVD-KamLAND-GW coincidence analysis is around 1.7 months due to the fact that the *GW duty cycle*² could be of the order of 40-70%, therefore, there are quite many deadtime periods between September 2015 to January 2016 which makes the GW livetime less than our neutrino livetime.

Due to the short common livetime, we made only 4 injected signals for each CCSN distance coherently: 8, 16, 32, 64, and 128 kpc. In this way, we would like to show what could be the improvement of significance of a *GW- ν* coincidence when we use our method in chapter 7 comparing with the standard method. In table 8.1-8.5, we presented our result for 8, 16, 32, 64, and 128 kpc respectively. Moreover, we also presented the background coincidences for double-neutrino data analysis in table 8.6.

TABLE 8.1: Details of *GW- ν* coincidences for 8 kpc. Column 2-5 are for KamLAND multiplicity, KamLand ξ [Hz], LVD multiplicity, and LVD ξ [Hz]. Column 6 and 7 are for the joint f^{im} [Hz] and the joint F^{im} [Hz] between KamLAND and LVD. Column 8, 9, and 10 are for the FAR [Hz] of GW candidates, the jointFAP of KamLAND-LVD-GW coincidences with the standard f^{im} , and the jointFAP of triple coincidences with the new F^{im} .

Coin.	m_K	ξ_K	m_{LVD}	ξ_{LVD}	f_d^{im}	F_d^{im}	FAR_{GW}	$\text{FAP}_{\text{t,old}}$	$\text{FAP}_{\text{t,new}}$
$c_{8,1}$	519	121.2	447	96.1	0	0	6e-09	0	0
$c_{8,2}$	498	60	428	68.4	0	0	1e-09	0	0
$c_{8,3}$	505	73.9	435	104.8	0	0	2e-08	0	0
$c_{8,4}$	457	75.2	390	83.1	0	0	2e-08	0	0

Table 8.1-8.3 do not give us strong insights. The f^{im} and F^{im} in those tables are already very tiny and our 2-parameter method could not give any strong improvement. The $\text{FAP}_{\text{t,old}}$ and $\text{FAP}_{\text{t,new}}$ (using the old standard f^{im} vs new F^{im}) are already 0, which means basically that our significance values are all

²Duty cycle is the fraction of data taking when the detectors are in a properly working condition.

Chapter 8. GW- ν Joint Search

TABLE 8.2: Details of GW- ν coincidences for 16 kpc. The legends are the same as in table 8.1.

Coin.	m_K	ξ_K	m_{LVD}	ξ_{LVD}	f_d^{im}	F_d^{im}	FAR_{GW}	$\text{FAP}_{t,\text{old}}$	$\text{FAP}_{t,\text{new}}$
$c_{16,1}$	134	11.1	117	16.2	0	0	2e-08	0	0
$c_{16,2}$	124	16.3	107	18.1	0	0	1e-09	0	0
$c_{16,3}$	127	19.2	110	18.9	0	0	6e-09	0	0
$c_{16,4}$	104	23.8	88	21.1	0	0	2e-08	0	0

TABLE 8.3: Details of GW- ν coincidences for 32 kpc. The legends are the same as in table 8.1.

Coin.	m_K	ξ_K	m_{LVD}	ξ_{LVD}	f_d^{im}	F_d^{im}	FAR_{GW}	$\text{FAP}_{t,\text{old}}$	$\text{FAP}_{t,\text{new}}$
$c_{32,1}$	31	5.2	31	4.5	9e-84	1e-85	2e-08	0	0
$c_{32,2}$	28	4.4	30	9.4	5e-76	2e-78	1e-09	0	0
$c_{32,3}$	26	2.6	27	2.7	6e-67	4e-68	5e-09	0	0
$c_{32,4}$	28	4.4	23	3.3	3e-64	4e-66	1e-09	0	0

TABLE 8.4: Details of GW- ν coincidences for 64 kpc. The legends are the same as in table 8.1.

Coin.	m_K	ξ_K	m_{LVD}	ξ_{LVD}	f_d^{im}	F_d^{im}	FAR_{GW}	$\text{FAP}_{t,\text{old}}$	$\text{FAP}_{t,\text{new}}$
$c_{64,1}$	6	1.4	5	1.0	0.3	2e-03	1e-09	6e-02	4e-04
$c_{64,2}$	12	0.8	10	1.4	6e-16	5e-17	1e-08	1e-15	0
$c_{64,3}$	7	1.8	6	1.3	1e-03	4e-06	2e-09	6e-04	2e-06

TABLE 8.5: Details of GW- ν coincidences for 128 kpc. The legends are the same as in table 8.1.

Coin.	m_K	ξ_K	m_{LVD}	ξ_{LVD}	f_d^{im}	F_d^{im}	FAR_{GW}	$\text{FAP}_{t,\text{old}}$	$\text{FAP}_{t,\text{new}}$
$c_{128,1}$	4	0.3	4	0.3	1e+03	3e+02	7e-09	0.7	0.7

better than 8σ , taking into account that $8\sigma \approx 1 \times 10^{-16}$, which is the limit for double precision in computation.

Chapter 8. GW- ν Joint Search

Moreover, the FAR_{GW} can be of the order of $1e-09$ Hz from c_{WB} . This *false-alarm-rate* value, taking into account the livetime of GW data is ~ 1.7 months, by using equation 5.26, the significance becomes $\sim 0.0044 \approx 2.8\sigma$. This means that even if a GW trigger has a lower significance value, by using the triggered search from neutrino analysis, we could increase the triple coincidence, that means also increasing our confidence in the GW trigger that we find.

Moving on to table 8.4, it shows us that our new 2-parameter method (chapter 7) plays a significant role in improving the significance of candidates (see the color cells) for the triple coincidence analysis, which is basically the multimessenger search between neutrino and GW network. This also shows us that our method will improve the 64 kpc injections due to the fact that 64 kpc is the horizon for LVD-KamLAND. Moreover, if we see table 8.6, our new 2-parameter method practically does not change the background significance.

All in all, our method, thus, can also be used to increase the efficiency search of CCSNe in terms of multimessenger between low-energy neutrino and gravitational wave channel. We can basically run GW analysis with c_{WB} and then we could use the list of triggers for the coincidence analysis with low-energy neutrino data sets, with the significance estimation of each coincidence calculated by the method explained in this thesis.

Chapter 8. GW- ν Joint Search

TABLE 8.6: Details of background coincidences for 2ν network analysis. Column 2-5 are for KamLAND multiplicity, KamLand ξ [Hz], LVD multiplicity, and LVD ξ [Hz]. Column 6 and 7 are for the joint f_d^{im} [Hz] and the joint F_d^{im} [Hz] between KamLAND and LVD. Column 8 and 9 are for their FAPs with the f_d^{im} and F_d^{im} .

Coin.	m_K	ξ_K	m_{LVD}	ξ_{LVD}	f_d^{im}	F_d^{im}	FAP _{d,old}	FAP _{d,new}
$c_{\text{bg},1}$	3	0.2	5	0.3	1.6e+03	1e+03	1	1
$c_{\text{bg},2}$	3	0.2	5	0.3	1.6e+03	1e+03	1	1
$c_{\text{bg},3}$	3	0.2	5	0.5	1.6e+03	4e+02	1	1
$c_{\text{bg},4}$	3	0.2	5	0.4	1.6e+03	6e+02	1	1
$c_{\text{bg},5}$	4	0.4	4	0.2	1.0e+03	3e+02	1	1
$c_{\text{bg},6}$	4	0.4	4	0.3	1.0e+03	2e+02	1	1
$c_{\text{bg},7}$	3	1.0	4	0.2	1.4e+04	8e+02	1	1
$c_{\text{bg},8}$	3	0.2	4	0.3	1.4e+04	6e+03	1	1
$c_{\text{bg},9}$	3	0.2	4	0.3	1.4e+04	7e+03	1	1
$c_{\text{bg},10}$	3	0.7	4	0.5	1.4e+04	4e+02	1	1
$c_{\text{bg},11}$	3	0.7	4	0.5	1.4e+04	4e+02	1	1
$c_{\text{bg},12}$	3	0.3	4	0.2	1.4e+04	5e+03	1	1
$c_{\text{bg},13}$	3	0.5	4	0.5	1.4e+04	7e+02	1	1
$c_{\text{bg},14}$	3	0.5	4	0.5	1.4e+04	7e+02	1	1
$c_{\text{bg},15}$	3	0.3	4	0.2	1.4e+04	6e+03	1	1
$c_{\text{bg},16}$	3	0.4	4	0.2	1.4e+04	5e+03	1	1
$c_{\text{bg},17}$	3	0.2	4	0.3	1.4e+04	1e+04	1	1
$c_{\text{bg},18}$	3	0.4	4	0.3	1.4e+04	4e+03	1	1
$c_{\text{bg},19}$	3	0.6	4	0.3	1.4e+04	1e+03	1	1
$c_{\text{bg},20}$	3	0.3	4	0.5	1.4e+04	2e+03	1	1
$c_{\text{bg},21}$	3	0.5	4	0.2	1.4e+04	3e+03	1	1
$c_{\text{bg},22}$	3	0.8	4	0.3	1.4e+04	8e+02	1	1
$c_{\text{bg},23}$	3	0.8	4	0.3	1.4e+04	7e+02	1	1
$c_{\text{bg},24}$	3	0.8	4	0.3	1.4e+04	7e+02	1	1
$c_{\text{bg},25}$	3	0.3	4	0.5	1.4e+04	3e+03	1	1

Conclusion

In this thesis, the first several chapters were dedicated to review the general discussions regarding core-collapse supernovae, neutrinos and gravitational waves. First of all, we have discussed the standard astrophysical processes happening inside the stellar collapses (chapter 1). In chapter 2, we have studied the possibility to detect these rare astronomical objects in terms of the rate and distribution, the neutrino emission, and the gravitational wave emission (models). In chapter 3 we have recalled the only neutrino detection from a core-collapse supernova up to the present time, the possibility to detect core-collapse supernovae via gravitational wave telescopes, and the successful gravitational wave observations from non-CCSN sources.

Starting from chapter 4, we have moved our discussion on to the core works of this thesis. In chapter 4 we discussed several international efforts to hunt for core-collapse supernovae, as well as some examples of multimessenger search studies that we have also reproduced. We also studied the signal search via network of detectors, namely coincidence analysis (chapter 5) with two possible methods to proceed. In chapter 6, we described our simulated data of CCSNe built from our understanding and assumption of the processes. We also discussed step-by-step how to treat neutrino data. More importantly, we introduced a new powerful parameter, exploiting the temporal behavior of the astrophysical CCSN signal.

We went a step further on discussing this new parameter in chapter 7 by calculating a modification of imitation frequency used in the standard method of CCSN neutrino data analysis. This imitation frequency actually corresponds to the estimate of the significance value of each event cluster in the neutrino

data. We have seen how the new parameter may change our understanding whether a cluster is due to a background or an astrophysical signal. In other words, we discussed the improvement in efficiency which implies the expansion of current and future neutrino detector horizons to catch the CCNS neutrino bursts.

Finally, in chapter 8, we implemented our new parameter method in terms of multimessenger analysis between neutrino network and GW network. This chapter showed us that we can improve the significance of GW- ν coincidences of two orders of magnitude with respect to the standard combined search.

Appendix A

Chandrasekhar Mass Limit

Let's discuss the Chandrasekhar mass limit following cf. Appendix A on [2]. Poisson equation for spherically symmetric body with a gravitational potential Ψ can be written as,

$$\frac{1}{r^2} \frac{d}{dr} \left(r^2 \frac{d\Psi}{dr} \right) = 4\pi G\rho, \quad (\text{A.1})$$

where G is the Newton gravitational constant. In this calculation, we consider the time independent solution.

The hydrostatic equilibrium requires,

$$\frac{dP}{dr} = -\frac{d\Psi}{dr} \rho. \quad (\text{A.2})$$

Then, we also take our EoS in the form of,

$$P = K\rho^\gamma, \quad (\text{A.3})$$

where K and γ are constant, namely, polytropic relation and polytropic exponent. Combining these equations together with the EoS, we can write the hydrostatic equation as,

$$\frac{d\Psi}{dr} = -\gamma K \rho^{\gamma-2} \frac{d\rho}{dr}, \quad (\text{A.4})$$

and for $\gamma \neq 1$ therefore,

$$\rho = \left(\frac{-\Psi(\gamma-1)}{K\gamma} \right)^{\frac{1}{\gamma-1}}. \quad (\text{A.5})$$

Appendix A. Chandrasekhar Mass Limit

Putting equation A.5 to A.1 we get,

$$\frac{2}{r} \frac{d\Psi}{dr} + \frac{d^2\Psi}{dr^2} = 4\pi G \left(-\frac{\Psi(\gamma-1)}{K\gamma} \right)^{\frac{1}{\gamma-1}}. \quad (\text{A.6})$$

Then, let's define the polytropic index $n \equiv \frac{1}{\gamma-1}$, $z = Ar = \frac{4\pi G}{(n+1)^n K^n} (-\Psi_c^{n-1})$, and $w = \Psi/\Psi_c = (\rho/\rho_c)^{1/n}$. With the definitions in our hand, we can get the Lane-Emden equation,

$$\begin{aligned} \frac{d^2w}{dz^2} + \frac{2}{z} \frac{dw}{dz} + w^n &= 0, \\ \Leftrightarrow \frac{1}{z^2} \frac{d}{dz} \left(z^2 \frac{dw}{dz} \right) + w^n &= 0. \end{aligned} \quad (\text{A.7})$$

Appendix B

Gravitational Wave Solutions from Einstein Field Equations

Here, we will discuss some standard GW solutions from solving Einstein field equations with the idea of flat universe ($\eta_{\mu\nu}$) perturbed by a small disturbance¹ ($h_{\mu\nu}$). In other words, we will use our metric as,

$$g_{\mu\nu} = \eta_{\mu\nu} + h_{\mu\nu}. \quad (\text{B.1})$$

This study can be seen in more detail such as in [24, 49, 135] and many more references, as well as some simple summary such as in [50, 51]. As we know, Einstein field equations can be written as,

$$R_{\mu\nu} - \frac{1}{2}Rg_{\mu\nu} = 8\pi GT_{\mu\nu}, \quad (\text{B.2})$$

where $R_{\mu\nu}$, R , and $T_{\mu\nu}$ are Ricci tensor, Ricci scalar, stress-energy tensor respectively. By putting equation B.1 into equation B.2, as well as taking into account the coordinate² & metric transformation³ and Lorenz gauge condition⁴, we can have the solution of equation B.2 to be some kind of a wave equation,

$$\square \bar{h}_{\mu\nu} = -\frac{16\pi G}{c^4}T_{\mu\nu}. \quad (\text{B.3})$$

¹with $\|h_{\mu\nu}\| \ll 1$ and $\bar{h}_{\mu\nu} = h_{\mu\nu} - \frac{1}{2}\eta_{\mu\nu}h$

² $x^\mu \rightarrow x'^\mu = x^\mu + \phi^\mu(x)$; with $\|\partial_\mu \phi_\nu\| O(\|h_{\mu\nu}\|)$

³ $g_{\mu\nu}(x) \rightarrow g'_{\mu\nu}(x') = \frac{\partial x^\rho}{\partial x'^\mu} \frac{\partial x^\sigma}{\partial x'^\nu} g_{\rho\sigma}(x)$.

⁴ $\partial^\nu \bar{h}_{\mu\nu} = 0$.

Appendix B. Gravitational Wave Solutions from Einstein Field Equations

Under the coordinate transformation, we can choose in such a way that $\bar{h} = 0$ (traceless) and some ϕ^μ such that $h_{0i} = 0$ (transverse). Therefore, $\bar{h}_{\mu\nu} = h_{\mu\nu}$. Last, with also the Lorenz condition, we will have,

$$\partial^0 h_{00} + \partial^i h_{0i} = 0 \Rightarrow \partial^0 h_{00} = 0; \quad \text{due to transverse condition.} \quad (\text{B.4})$$

This means h_{00} is constant in time and can be understood as the Newtonian potential (the static part of gravitational interaction). Since it is a constant, we can set in the end h_{00} to be zero. Thus,

$$h_{0\mu} = 0; \quad h_i^i = 0; \quad \partial^j h_{ij} = 0, \quad (\text{B.5})$$

where this is defined as the *transverse-traceless gauge* (TT gauge). In general, equation B.5 can be written in a better way as,

$$h_{ij}^{\text{TT}}(t, z) = e_{ij}(\vec{k}) e^{ikx}, \quad (\text{B.6})$$

where $k^\mu = (\omega/c, \mathbf{k})$ and $\omega/c = \|\mathbf{k}\|$. For the z -axis propagation, our wave equation becomes,

$$h_{ij}^{\text{TT}}(t, z) = \begin{pmatrix} h_+ & h_\times & 0 \\ h_\times & -h_+ & 0 \\ 0 & 0 & 0 \end{pmatrix}_{ij} \cos[\omega(t - z/c)], \quad (\text{B.7})$$

where h_+ & h_\times are the polarization amplitudes. The pattern of test masses passed by gravitational waves can be seen in figure B.1.

Appendix B. Gravitational Wave Solutions from Einstein Field Equations

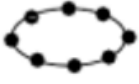
ωt	h_+	h_\times
0		
$\pi / 2$		
π		
$3 \pi / 2$		

FIGURE B.1: The scheme of the deformation of test masses (dots) passed by gravitational waves based on equation B.7 (taken from [24]).

Bibliography

- [1] Hans-Thomas Janka. “Explosion Mechanisms of Core-Collapse Supernovae”. In: *Annual Review of Nuclear and Particle Science* 62.1 (2012), pp. 407–451. DOI: [10.1146/annurev-nucl-102711-094901](https://doi.org/10.1146/annurev-nucl-102711-094901). eprint: <https://doi.org/10.1146/annurev-nucl-102711-094901>. URL: <https://doi.org/10.1146/annurev-nucl-102711-094901>.
- [2] G. Pagliaroli. “Statistical analysis of SN1987A neutrinos: implications for emission models, neutrino properties and gravitational waves search”. In: (2009).
- [3] Rudolf Kippenhahn, Alfred Weigert, and Achim Weiss. *Stellar Structure and Evolution*. Springer, 2012.
- [4] S.E. Woosley and J.S. Bloom. “The Supernova–Gamma-Ray Burst Connection”. In: *Annual Review of Astronomy and Astrophysics* 44.1 (2006), pp. 507–556. DOI: [10.1146/annurev.astro.43.072103.150558](https://doi.org/10.1146/annurev.astro.43.072103.150558). eprint: <https://doi.org/10.1146/annurev.astro.43.072103.150558>. URL: <https://doi.org/10.1146/annurev.astro.43.072103.150558>.
- [5] H A. Bethe and J R. Wilson. “Revival of a stalled supernova shock by neutrino heating”. In: *The Astrophysical Journal* 295 (July 1985), pp. 14–23. DOI: [10.1086/163343](https://doi.org/10.1086/163343).
- [6] H. A. Bethe. “Supernova mechanisms”. In: *Rev. Mod. Phys.* 62 (4 1990), pp. 801–866. DOI: [10.1103/RevModPhys.62.801](https://doi.org/10.1103/RevModPhys.62.801). URL: <https://link.aps.org/doi/10.1103/RevModPhys.62.801>.

Bibliography

- [7] Hans-Thomas Janka et al. "Core-Collapse Supernovae: Reflections and Directions". In: *Progress of Theoretical and Experimental Physics* 2012 (Nov. 2012). DOI: [10.1093/ptep/pts067](https://doi.org/10.1093/ptep/pts067).
- [8] William F. Bleam. "Chapter 1 - Elements: Their Origin and Abundance". In: *Soil and Environmental Chemistry*. Ed. by William F. Bleam. Boston: Academic Press, 2012, pp. 1–39. ISBN: 978-0-12-415797-2. DOI: <https://doi.org/10.1016/B978-0-12-415797-2.00001-7>. URL: <http://www.sciencedirect.com/science/article/pii/B9780124157972000017>.
- [9] M. A. Ivanov and G. A. Shulman. "Photodissociation of Iron Nuclei in the Collapse of a Magnetic Star". In: 34 (1990), p. 163.
- [10] P. Goldreich and S. V. Weber. "Homologously collapsing stellar cores". In: 238 (1980), pp. 991–997. DOI: [10.1086/158065](https://doi.org/10.1086/158065).
- [11] T. Totani et al. "Future Detection of Supernova Neutrino Burst and Explosion Mechanism". In: *The Astrophysical Journal* 496.1 (1998), pp. 216–225. DOI: [10.1086/305364](https://doi.org/10.1086/305364). URL: <https://doi.org/10.1086%2F305364>.
- [12] Marek, A., Janka, H.-T., and Müller, E. "Equation-of-state dependent features in shock-oscillation modulated neutrino and gravitational-wave signals from supernovae". In: *A&A* 496.2 (2009), pp. 475–494. DOI: [10.1051/0004-6361/200810883](https://doi.org/10.1051/0004-6361/200810883). URL: <https://doi.org/10.1051/0004-6361/200810883>.
- [13] Jeremiah W. Murphy, Christian D. Ott, and Adam Burrows. "A MODEL FOR GRAVITATIONAL WAVE EMISSION FROM NEUTRINO-DRIVEN CORE-COLLAPSE SUPERNOVAE". In: *The Astrophysical Journal* 707.2 (2009), pp. 1173–1190. DOI: [10.1088/0004-637x/707/2/1173](https://doi.org/10.1088/0004-637x/707/2/1173). URL: <https://doi.org/10.1088%2F0004-637x%2F707%2F2%2F1173>.

Bibliography

- [14] Takami Kuroda, Kei Kotake, and Tomoya Takiwaki. “A new Gravitational-wave Signature From Standing Accretion Shock Instability in Supernovae”. In: *Astrophys. J.* 829.1 (2016), p. L14. DOI: [10.3847/2041-8205/829/1/L14](https://doi.org/10.3847/2041-8205/829/1/L14). arXiv: [1605.09215](https://arxiv.org/abs/1605.09215) [astro-ph.HE].
- [15] John M. Blondin, Anthony Mezzacappa, and Christine DeMarino. “Stability of Standing Accretion Shocks, with an Eye toward Core-Collapse Supernovae”. In: *The Astrophysical Journal* 584.2 (2003), pp. 971–980. DOI: [10.1086/345812](https://doi.org/10.1086/345812). URL: <https://doi.org/10.1086%2F345812>.
- [16] Hans-Thomas Janka, Tobias Melson, and Alexander Summa. “Physics of Core-Collapse Supernovae in Three Dimensions: A Sneak Preview”. In: *Annual Review of Nuclear and Particle Science* 66.1 (2016), pp. 341–375. DOI: [10.1146/annurev-nucl-102115-044747](https://doi.org/10.1146/annurev-nucl-102115-044747). eprint: <https://doi.org/10.1146/annurev-nucl-102115-044747>. URL: <https://doi.org/10.1146/annurev-nucl-102115-044747>.
- [17] Jade Powell et al. “Inferring the core-collapse supernova explosion mechanism with gravitational waves”. In: *Phys. Rev.* D94.12 (2016), p. 123012. DOI: [10.1103/PhysRevD.94.123012](https://doi.org/10.1103/PhysRevD.94.123012). arXiv: [1610.05573](https://arxiv.org/abs/1610.05573) [astro-ph.HE].
- [18] H. Th. Janka. “Neutrino-driven Explosions”. In: (2017). DOI: [10.1007/978-3-319-21846-5_109](https://doi.org/10.1007/978-3-319-21846-5_109). arXiv: [1702.08825](https://arxiv.org/abs/1702.08825) [astro-ph.HE].
- [19] Michele Maggiore. *Gravitational Waves. Vol. 2: Astrophysics and Cosmology*. Oxford University Press, 2018. ISBN: 9780198570899.
- [20] Enrico Cappellaro and Massimo Turatto. “Supernova types and rates”. In: *Astrophys. Space Sci. Libr.* 264 (2001), p. 199. DOI: [10.1007/978-94-015-9723-4_16](https://doi.org/10.1007/978-94-015-9723-4_16). arXiv: [astro-ph/0012455](https://arxiv.org/abs/astro-ph/0012455) [astro-ph].
- [21] K. Hirata et al. “Observation of a neutrino burst from the supernova SN1987A”. In: *Phys. Rev. Lett.* 58 (14 1987), pp. 1490–1493. DOI: [10.1103/PhysRevLett.58.1490](https://doi.org/10.1103/PhysRevLett.58.1490). URL: <https://link.aps.org/doi/10.1103/PhysRevLett.58.1490>.

Bibliography

- [22] R. M. Bionta et al. "Observation of a Neutrino Burst in Coincidence with Supernova SN 1987a in the Large Magellanic Cloud". In: *Phys. Rev. Lett.* 58 (1987), p. 1494. DOI: [10.1103/PhysRevLett.58.1494](https://doi.org/10.1103/PhysRevLett.58.1494).
- [23] E.N. Alexeyev et al. "Detection of the neutrino signal from SN 1987A in the LMC using the INR Baksan underground scintillation telescope". In: *Physics Letters B* 205.2 (1988), pp. 209–214. ISSN: 0370-2693. DOI: [https://doi.org/10.1016/0370-2693\(88\)91651-6](https://doi.org/10.1016/0370-2693(88)91651-6). URL: <http://www.sciencedirect.com/science/article/pii/0370269388916516>.
- [24] M. Maggiore. *Gravitational Waves: Volume 1: Theory and Experiments*. OUP Oxford, 2007. ISBN: 9780198570745. URL: <https://books.google.it/books?id=AqVpQgAACAAJ>.
- [25] Roland Diehl et al. "Radioactive Al-26 and massive stars in the galaxy". In: *Nature* 439 (2006), pp. 45–47. DOI: [10.1038/nature04364](https://doi.org/10.1038/nature04364). arXiv: [astro-ph/0601015](https://arxiv.org/abs/astro-ph/0601015) [astro-ph].
- [26] Matthew D. Kistler et al. "Core-Collapse Astrophysics with a Five-Megaton Neutrino Detector". In: *Phys. Rev. D* 83 (2011), p. 123008. DOI: [10.1103/PhysRevD.83.123008](https://doi.org/10.1103/PhysRevD.83.123008). arXiv: [0810.1959](https://arxiv.org/abs/0810.1959) [astro-ph].
- [27] Markus Ahlers, Philipp Mertsch, and Subir Sarkar. "Cosmic ray acceleration in supernova remnants and the FERMI/PAMELA data". In: *Phys. Rev. D* 80 (12 2009), p. 123017. DOI: [10.1103/PhysRevD.80.123017](https://doi.org/10.1103/PhysRevD.80.123017). URL: <https://link.aps.org/doi/10.1103/PhysRevD.80.123017>.
- [28] Matthew D. Kistler, W. C. Haxton, and Hasan Yüksel. "TOMOGRAPHY OF MASSIVE STARS FROM CORE COLLAPSE TO SUPERNOVA SHOCK BREAKOUT". In: *The Astrophysical Journal* 778.1 (2013), p. 81. DOI: [10.1088/0004-637x/778/1/81](https://doi.org/10.1088/0004-637x/778/1/81). URL: <https://doi.org/10.1088%2F0004-637x%2F778%2F1%2F81>.

Bibliography

- [29] A. Odrzywolek, M. Misiaszek, and M. Kutschera. "Detection possibility of the pair-annihilation neutrinos from the neutrino-cooled pre-supernova star". In: *Astroparticle Physics* 21.3 (2004), pp. 303–313. ISSN: 0927-6505. DOI: <https://doi.org/10.1016/j.astropartphys.2004.02.002>. URL: <http://www.sciencedirect.com/science/article/pii/S0927650504000349>.
- [30] Chinami Kato et al. "PRE-SUPERNOVA NEUTRINO EMISSIONS FROM ONe CORES IN THE PROGENITORS OF CORE-COLLAPSE SUPERNOVAE: ARE THEY DISTINGUISHABLE FROM THOSE OF Fe CORES?" In: *The Astrophysical Journal* 808.2 (2015), p. 168. DOI: [10.1088/0004-637x/808/2/168](https://doi.org/10.1088/0004-637x/808/2/168). URL: <https://doi.org/10.1088/0004-637x/808/2/168>.
- [31] K. Asakura et al. "KamLAND SENSITIVITY TO NEUTRINOS FROM PRE-SUPERNOVA STARS". In: *The Astrophysical Journal* 818.1 (2016), p. 91. DOI: [10.3847/0004-637x/818/1/91](https://doi.org/10.3847/0004-637x/818/1/91). URL: <https://doi.org/10.3847/0004-637x/818/1/91>.
- [32] Takashi Yoshida et al. "Presupernova neutrino events relating to the final evolution of massive stars". In: *Phys. Rev. D* 93 (12 2016), p. 123012. DOI: [10.1103/PhysRevD.93.123012](https://doi.org/10.1103/PhysRevD.93.123012). URL: <https://link.aps.org/doi/10.1103/PhysRevD.93.123012>.
- [33] G. Alimonti et al. "Ultra-low background measurements in a large volume underground detector". In: *Astroparticle Physics* 8.3 (1998), pp. 141–157. ISSN: 0927-6505. DOI: [https://doi.org/10.1016/S0927-6505\(97\)00050-9](https://doi.org/10.1016/S0927-6505(97)00050-9). URL: <http://www.sciencedirect.com/science/article/pii/S0927650597000509>.
- [34] F. Suekane et al. "An overview of the kamland 1-kiloton liquid scintillator". In: *Scintillating crystals. Proceedings, International School and Mini-Workshop for scintillating crystals and their applications in particle and nuclear physics, Tsukuba, Japan, November 17-18, 2003*. 2004, pp. 279–290. arXiv: [physics/0404071](https://arxiv.org/abs/physics/0404071) [physics].

Bibliography

- [35] Yu-Feng Li. “Jiangmen Underground Neutrino Observatory: Status and Prospectives”. In: *Proceedings, 17th Lomonosov Conference on Elementary Particle Physics: Moscow, Russia, August 20-26, 2015*. 2017, pp. 27–33. DOI: [10.1142/9789813224568_0004](https://doi.org/10.1142/9789813224568_0004). arXiv: [1606.04743](https://arxiv.org/abs/1606.04743) [[physics.ins-det](#)].
- [36] B. Abi et al. “The DUNE Far Detector Interim Design Report, Volume 2: Single-Phase Module”. In: (2018). arXiv: [1807.10327](https://arxiv.org/abs/1807.10327) [[physics.ins-det](#)].
- [37] Y. Fukuda et al. “The Super-Kamiokande detector”. In: *Nucl. Instrum. Meth. A* 501 (2003), pp. 418–462. DOI: [10.1016/S0168-9002\(03\)00425-X](https://doi.org/10.1016/S0168-9002(03)00425-X).
- [38] K. Abe et al. “Hyper-Kamiokande Design Report”. In: (2018). arXiv: [1805.04163](https://arxiv.org/abs/1805.04163) [[physics.ins-det](#)].
- [39] Pasquale D. Serpico et al. “Probing the neutrino mass hierarchy with the rise time of a supernova burst”. In: *Phys. Rev. D* 85 (2012), p. 085031. DOI: [10.1103/PhysRevD.85.085031](https://doi.org/10.1103/PhysRevD.85.085031). arXiv: [1111.4483](https://arxiv.org/abs/1111.4483) [[astro-ph.SR](#)].
- [40] M. Kachelrieß et al. “Exploiting the neutronization burst of a galactic supernova”. In: *Phys. Rev. D* 71 (6 2005), p. 063003. DOI: [10.1103/PhysRevD.71.063003](https://doi.org/10.1103/PhysRevD.71.063003). URL: <https://link.aps.org/doi/10.1103/PhysRevD.71.063003>.
- [41] M.G. Aartsen et al. “The IceCube Neutrino Observatory: instrumentation and online systems”. In: *Journal of Instrumentation* 12.03 (2017), P03012–P03012. DOI: [10.1088/1748-0221/12/03/p03012](https://doi.org/10.1088/1748-0221/12/03/p03012). URL: <https://doi.org/10.1088/1748-0221/12/03/p03012>.
- [42] F. Halzen and G. G. Raffelt. “Reconstructing the supernova bounce time with neutrinos in IceCube”. In: ().
- [43] Takaaki Yokozawa et al. “PROBING THE ROTATION OF CORE-COLLAPSE SUPERNOVA WITH A CONCURRENT ANALYSIS OF GRAVITATIONAL WAVES AND NEUTRINOS”. In: *The Astrophysical Journal* 811.2 (2015),

Bibliography

- p. 86. DOI: [10.1088/0004-637x/811/2/86](https://doi.org/10.1088/0004-637x/811/2/86). URL: <https://doi.org/10.1088/0004-637x/811/2/86>.
- [44] B. Muller. “Neutrino Emission as Diagnostics of Core-Collapse Supernovae”. In: *arXiv e-prints* (2019). arXiv: [1904.11067](https://arxiv.org/abs/1904.11067) [[astro-ph.HE](https://arxiv.org/abs/1904.11067)].
- [45] Bernhard Müller and Hans-Thomas Janka. “A NEW MULTI-DIMENSIONAL GENERAL RELATIVISTIC NEUTRINO HYDRODYNAMICS CODE FOR CORE-COLLAPSE SUPERNOVAE. IV. THE NEUTRINO SIGNAL”. In: *The Astrophysical Journal* 788.1 (2014), p. 82. DOI: [10.1088/0004-637x/788/1/82](https://doi.org/10.1088/0004-637x/788/1/82). URL: <https://doi.org/10.1088/0004-637x/788/1/82>.
- [46] G. Pagliaroli et al. “Improved analysis of SN1987A antineutrino events”. In: *Astroparticle Physics* 31.3 (2009), pp. 163–176. ISSN: 0927-6505. DOI: <https://doi.org/10.1016/j.astropartphys.2008.12.010>. URL: <http://www.sciencedirect.com/science/article/pii/S0927650508001965>.
- [47] C. Casentini. “Coincident search for astrophysical bursts in Gravitational Waves and Low Energy Neutrino detectors”. In: (2017).
- [48] Alessandro Strumia and Francesco Vissani. “Precise quasielastic neutrino/nucleon cross-section”. In: *Physics Letters B* 564.1 (2003), pp. 42–54. ISSN: 0370-2693. DOI: [https://doi.org/10.1016/S0370-2693\(03\)00616-6](https://doi.org/10.1016/S0370-2693(03)00616-6). URL: <http://www.sciencedirect.com/science/article/pii/S0370269303006166>.
- [49] Charles W. Misner, K. S. Thorne, and J. A. Wheeler. *Gravitation*. San Francisco: W. H. Freeman, 1973. ISBN: 9780716703440, 9780691177793.
- [50] O. Halim. “WAVES EMERGED BY SMALL PERTURBATION ON THE MINKOWSKI METRIC”. In: (2012).
- [51] O. Halim. “Efficiency Studies of the All-sky Frequency-Hough Search for Continuous Gravitational Waves”. In: (2016).

Bibliography

- [52] Christian D Ott. “The gravitational-wave signature of core-collapse supernovae”. In: *Classical and Quantum Gravity* 26.6 (2009), p. 063001. DOI: [10.1088/0264-9381/26/6/063001](https://doi.org/10.1088/0264-9381/26/6/063001). URL: <https://doi.org/10.1088%2F0264-9381%2F26%2F6%2F063001>.
- [53] S. E. Gossan et al. “Observing Gravitational Waves from Core-Collapse Supernovae in the Advanced Detector Era”. In: *Phys. Rev. D* 93.4 (2016), p. 042002. DOI: [10.1103/PhysRevD.93.042002](https://doi.org/10.1103/PhysRevD.93.042002). arXiv: [1511.02836](https://arxiv.org/abs/1511.02836) [astro-ph.HE].
- [54] Harald Dimmelmeier et al. “Gravitational wave burst signal from core collapse of rotating stars”. In: *Phys. Rev. D* 78 (6 2008), p. 064056. DOI: [10.1103/PhysRevD.78.064056](https://doi.org/10.1103/PhysRevD.78.064056). URL: <https://link.aps.org/doi/10.1103/PhysRevD.78.064056>.
- [55] A. Burrows et al. “A New Mechanism for Core-Collapse Supernova Explosions”. In: *The Astrophysical Journal* 640.2 (2006), pp. 878–890. DOI: [10.1086/500174](https://doi.org/10.1086/500174). URL: <https://doi.org/10.1086%2F500174>.
- [56] Kazuhiro Hayama et al. “Circular polarization of gravitational waves from non-rotating supernova cores: a new probe into the pre-explosion hydrodynamics”. In: *Mon. Not. Roy. Astron. Soc.* 477.1 (2018), pp. L96–L100. DOI: [10.1093/mnrasl/sly055](https://doi.org/10.1093/mnrasl/sly055). arXiv: [1802.03842](https://arxiv.org/abs/1802.03842) [astro-ph.HE].
- [57] Hajime Kawahara et al. “A Linear and Quadratic Time-Frequency Analysis of Gravitational Waves from Core-collapse Supernovae”. In: *Astrophys. J.* 867.2 (2018), p. 126. DOI: [10.3847/1538-4357/aae57b](https://doi.org/10.3847/1538-4357/aae57b). arXiv: [1810.00334](https://arxiv.org/abs/1810.00334) [astro-ph.HE].
- [58] Alejandro Torres-Forné et al. “Towards asteroseismology of core-collapse supernovae with gravitational wave observations — II. Inclusion of space-time perturbations”. In: *Mon. Not. Roy. Astron. Soc.* 482.3 (2019), pp. 3967–3988. DOI: [10.1093/mnras/sty2854](https://doi.org/10.1093/mnras/sty2854). arXiv: [1806.11366](https://arxiv.org/abs/1806.11366) [astro-ph.HE].

Bibliography

- [59] David Radice et al. “Characterizing the Gravitational Wave Signal from Core-collapse Supernovae”. In: *The Astrophysical Journal* 876.1 (2019), p. L9. DOI: [10.3847/2041-8213/ab191a](https://doi.org/10.3847/2041-8213/ab191a). URL: <https://doi.org/10.3847%2F2041-8213%2Fab191a>.
- [60] Andrew W. Steiner, Matthias Hempel, and Tobias Fischer. “Core-collapse supernova equations of state based on neutron star observations”. In: *Astrophys. J.* 774 (2013), p. 17. DOI: [10.1088/0004-637X/774/1/17](https://doi.org/10.1088/0004-637X/774/1/17). arXiv: [1207.2184](https://arxiv.org/abs/1207.2184) [astro-ph.SR].
- [61] Kate Scholberg. “Supernova neutrino detection”. In: *Nucl. Phys. Proc. Suppl.* 91 (2001). [331(2000)], pp. 331–337. DOI: [10.1016/S0920-5632\(00\)00959-2](https://doi.org/10.1016/S0920-5632(00)00959-2). arXiv: [hep-ex/0008044](https://arxiv.org/abs/hep-ex/0008044) [hep-ex].
- [62] Pietro Antonioli et al. “SNEWS: the SuperNova Early Warning System”. In: *New Journal of Physics* 6 (2004), pp. 114–114. DOI: [10.1088/1367-2630/6/1/114](https://doi.org/10.1088/1367-2630/6/1/114). URL: <https://doi.org/10.1088%2F1367-2630%2F6%2F1%2F114>.
- [63] IceCube Collaboration et al. “IceCube sensitivity for low-energy neutrinos from nearby supernovae”. In: *A&A* 535 (2011), A109. DOI: [10.1051/0004-6361/201117810](https://doi.org/10.1051/0004-6361/201117810). URL: <https://doi.org/10.1051/0004-6361/201117810>.
- [64] M. Ikeda et al. “Search for Supernova Neutrino Bursts at Super-Kamiokande”. In: *Astrophys. J.* 669 (2007), pp. 519–524. DOI: [10.1086/521547](https://doi.org/10.1086/521547). arXiv: [0706.2283](https://arxiv.org/abs/0706.2283) [astro-ph].
- [65] K. Abe et al. “Real-Time Supernova Neutrino Burst Monitor at Super-Kamiokande”. In: *Astropart. Phys.* 81 (2016), pp. 39–48. DOI: [10.1016/j.astropartphys.2016.04.003](https://doi.org/10.1016/j.astropartphys.2016.04.003). arXiv: [1601.04778](https://arxiv.org/abs/1601.04778) [astro-ph.HE].
- [66] Evan O’Connor. “AN OPEN-SOURCE NEUTRINO RADIATION HYDRODYNAMICS CODE FOR CORE-COLLAPSE SUPERNOVAE”. In: *The Astrophysical Journal Supplement Series* 219.2 (2015), p. 24. DOI: [10.](https://doi.org/10.1088/0004-6361/20152192a)

Bibliography

- 1088/0067-0049/219/2/24. URL: <https://doi.org/10.1088%2F0067-0049%2F219%2F2%2F24>.
- [67] R. Brun et al. *GEANT 3: user's guide Geant 3.10, Geant 3.11; rev. version*. Geneva: CERN, 1987. URL: <https://cds.cern.ch/record/1119728>.
- [68] N.Y. Agafonova et al. "Implication for the Core-collapse Supernova Rate From 21 Years of Data of the Large Volume Detector". In: *Astrophys. J.* 802.1 (2015), p. 47. DOI: [10.1088/0004-637X/802/1/47](https://doi.org/10.1088/0004-637X/802/1/47). arXiv: [1411.1709](https://arxiv.org/abs/1411.1709) [astro-ph.HE].
- [69] Thomas Morris and Philipp Podsiadlowski. "The Triple-Ring Nebula Around SN 1987A: Fingerprint of a Binary Merger". In: *Science* 315.5815 (2007), pp. 1103–1106. ISSN: 0036-8075. DOI: [10.1126/science.1136351](https://doi.org/10.1126/science.1136351). eprint: <https://science.sciencemag.org/content/315/5815/1103.full.pdf>. URL: <https://science.sciencemag.org/content/315/5815/1103>.
- [70] M. Koshiya et al. "Supernova 1987A in the Large Magellanic Cloud". In: 4338 (1987). URL: <https://ui.adsabs.harvard.edu/abs/1987IAUC.4338....1K>.
- [71] R. A. Hulse and J. H. Taylor. "Discovery of a pulsar in a binary system". In: *APJL* 195 (Jan. 1975), pp. L51–L53. DOI: [10.1086/181708](https://doi.org/10.1086/181708).
- [72] Nobel prize in physics in 1993. URL: <https://www.nobelprize.org/prizes/physics/1993/summary/>.
- [73] Joel M. Weisberg and Joseph H. Taylor. "Relativistic binary pulsar B1913+16: Thirty years of observations and analysis". In: *ASP Conf. Ser.* 328 (2005), p. 25. arXiv: [astro-ph/0407149](https://arxiv.org/abs/astro-ph/0407149) [astro-ph].
- [74] Francesco Ronga. "Detection of gravitational waves with resonant antennas". In: *Journal of Physics: Conference Series* 39 (2006), pp. 18–24. DOI: [10.1088/1742-6596/39/1/005](https://doi.org/10.1088/1742-6596/39/1/005). URL: <https://doi.org/10.1088%2F1742-6596%2F39%2F1%2F005>.

Bibliography

- [75] P. Astone et al. "EXPLORER and NAUTILUS gravitational wave detectors: A status report". In: *Class. Quant. Grav.* 25 (2008), p. 114048. DOI: [10.1088/0264-9381/25/11/114048](https://doi.org/10.1088/0264-9381/25/11/114048).
- [76] A. Abramovici et al. "LIGO: The Laser Interferometer Gravitational-Wave Observatory". In: *Science* 256.5055 (1992). cited By 1699, pp. 325–333. DOI: [10.1126/science.256.5055.325](https://doi.org/10.1126/science.256.5055.325). URL: <https://www.scopus.com/inward/record.uri?eid=2-s2.0-0011490655&doi=10.1126%2fscience.256.5055.325&partnerID=40&md5=18d5121e2c5cd5107f754fa77d72c244>.
- [77] Nautilus View. URL: <http://w3.lnf.infn.it/research/astroparticle-physics/nautilus/?lang=en>.
- [78] H Lück and. "The GEO600 project". In: *Classical and Quantum Gravity* 14.6 (1997), pp. 1471–1476. DOI: [10.1088/0264-9381/14/6/012](https://doi.org/10.1088/0264-9381/14/6/012). URL: <https://doi.org/10.1088%2F0264-9381%2F14%2F6%2F012>.
- [79] T. Akutsu et al. "KAGRA: 2.5 Generation Interferometric Gravitational Wave Detector". In: *Nat. Astron.* 3.1 (2019), pp. 35–40. DOI: [10.1038/s41550-018-0658-y](https://doi.org/10.1038/s41550-018-0658-y). arXiv: [1811.08079 \[gr-qc\]](https://arxiv.org/abs/1811.08079).
- [80] C. S. Unnikrishnan. "IndIGO and LIGO-India: Scope and plans for gravitational wave research and precision metrology in India". In: *Int. J. Mod. Phys. D* 22 (2013), p. 1341010. DOI: [10.1142/S0218271813410101](https://doi.org/10.1142/S0218271813410101). arXiv: [1510.06059 \[physics.ins-det\]](https://arxiv.org/abs/1510.06059).
- [81] LIGO Livingston Aerial View. URL: <https://www.ligo.caltech.edu/image/ligo20150731c>.
- [82] LIGO Hanford Aerial View. URL: <https://www.skyandtelescope.com/astronomy-news/advanced-ligo-switches-on-10142015/>.
- [83] Virgo Aerial View. URL: <https://physicstoday.scitation.org/doi/10.1063/PT.6.1.20170927a/full/>.

Bibliography

- [84] T Accadia et al. “Virgo: a laser interferometer to detect gravitational waves”. In: *Journal of Instrumentation* 7.03 (2012), P03012–P03012. DOI: [10.1088/1748-0221/7/03/p03012](https://doi.org/10.1088/1748-0221/7/03/p03012). URL: <https://doi.org/10.1088%2F1748-0221%2F7%2F03%2Fp03012>.
- [85] Samantha A Usman et al. “The PyCBC search for gravitational waves from compact binary coalescence”. In: *Classical and Quantum Gravity* 33.21 (2016), p. 215004. DOI: [10.1088/0264-9381/33/21/215004](https://doi.org/10.1088/0264-9381/33/21/215004). URL: <https://doi.org/10.1088%2F0264-9381%2F33%2F21%2F215004>.
- [86] Patrick J Sutton et al. “X-Pipeline: an analysis package for autonomous gravitational-wave burst searches”. In: *New Journal of Physics* 12.5 (2010), p. 053034. DOI: [10.1088/1367-2630/12/5/053034](https://doi.org/10.1088/1367-2630/12/5/053034). URL: <https://doi.org/10.1088%2F1367-2630%2F12%2F5%2F053034>.
- [87] S Klimenko and G Mitselmakher. “A wavelet method for detection of gravitational wave bursts”. In: *Classical and Quantum Gravity* 21.20 (2004), S1819–S1830. DOI: [10.1088/0264-9381/21/20/025](https://doi.org/10.1088/0264-9381/21/20/025). URL: <https://doi.org/10.1088%2F0264-9381%2F21%2F20%2F025>.
- [88] S Klimenko et al. “A coherent method for detection of gravitational wave bursts”. In: *Classical and Quantum Gravity* 25.11 (2008), p. 114029. DOI: [10.1088/0264-9381/25/11/114029](https://doi.org/10.1088/0264-9381/25/11/114029). URL: <https://doi.org/10.1088%2F0264-9381%2F25%2F11%2F114029>.
- [89] M. Drago. “SEARCH FOR TRANSIENT GRAVITATIONAL WAVE SIGNALS WITH UNKNOWN WAVEFORM IN THE LIGO VIRGO NETWORK OF INTERFEROMETRIC DETECTORS USING A FULLY COHERENT ALGORITHM”. In: (2010).
- [90] V Neucula, S Klimenko, and G Mitselmakher. “Transient analysis with fast Wilson-Daubechies time-frequency transform”. In: *Journal of Physics: Conference Series* 363 (2012), p. 012032. DOI: [10.1088/1742-6596/](https://doi.org/10.1088/1742-6596/)

Bibliography

- 363/1/012032. URL: <https://doi.org/10.1088%2F1742-6596%2F363%2F1%2F012032>.
- [91] coherent WaveBurst. URL: ldas-jobs.ligo.caltech.edu/~waveburst/doc/cwb/xman/running.html.
- [92] B. P. Abbott et al. "Observation of Gravitational Waves from a Binary Black Hole Merger". In: *Phys. Rev. Lett.* 116 (6 2016), p. 061102. DOI: [10.1103/PhysRevLett.116.061102](https://doi.org/10.1103/PhysRevLett.116.061102). URL: <https://link.aps.org/doi/10.1103/PhysRevLett.116.061102>.
- [93] J. C. van den Berg. (editor). *Wavelets in Physics*. Cambridge University Press, 2004.
- [94] R. Ganesan, T. K. Das, and V. Venkataraman. "Wavelet-based multi-scale statistical process monitoring: A literature review". In: *IIE Transactions* 36.9 (2004), pp. 787–806. DOI: [10.1080/07408170490473060](https://doi.org/10.1080/07408170490473060). eprint: <https://doi.org/10.1080/07408170490473060>. URL: <https://doi.org/10.1080/07408170490473060>.
- [95] B. P. Abbott et al. "An Optically Targeted Search for Gravitational Waves emitted by Core-Collapse Supernovae during the First and Second Observing Runs of Advanced LIGO and Advanced Virgo". In: (2019). arXiv: [1908.03584](https://arxiv.org/abs/1908.03584) [astro-ph.HE].
- [96] B. P. Abbott et al. "GW170814: A Three-Detector Observation of Gravitational Waves from a Binary Black Hole Coalescence". In: *Phys. Rev. Lett.* 119 (14 2017), p. 141101. DOI: [10.1103/PhysRevLett.119.141101](https://doi.org/10.1103/PhysRevLett.119.141101). URL: <https://link.aps.org/doi/10.1103/PhysRevLett.119.141101>.
- [97] B. P. Abbott et al. "Multi-messenger Observations of a Binary Neutron Star Merger". In: *The Astrophysical Journal* 848.2 (2017), p. L12. DOI: [10.3847/2041-8213/aa91c9](https://doi.org/10.3847/2041-8213/aa91c9). URL: <https://doi.org/10.3847%2F2041-8213%2Faa91c9>.

Bibliography

- [98] B. P. Abbott et al. “GW170817: Observation of Gravitational Waves from a Binary Neutron Star Inspiral”. In: *Phys. Rev. Lett.* 119 (16 2017), p. 161101. DOI: [10.1103/PhysRevLett.119.161101](https://doi.org/10.1103/PhysRevLett.119.161101). URL: <https://link.aps.org/doi/10.1103/PhysRevLett.119.161101>.
- [99] A. Goldstein et al. “An Ordinary Short Gamma-Ray Burst with Extraordinary Implications: Fermi-GBM Detection of GRB 170817A”. In: *Astrophys. J.* 848.2 (2017), p. L14. DOI: [10.3847/2041-8213/aa8f41](https://doi.org/10.3847/2041-8213/aa8f41). arXiv: [1710.05446](https://arxiv.org/abs/1710.05446) [astro-ph.HE].
- [100] SNEWS2.0 Workshop. URL: <https://snews2.0.snolab.ca/>.
- [101] SuperNova Early Warning System (SNEWS). URL: <https://snews.bnl.gov/whatisnews.html>.
- [102] M. Aglietta et al. “The most powerful scintillator supernovae detector: LVD”. In: *Il Nuovo Cimento A Series 11* 105.12 (1992). cited By 103, pp. 1793–1804. DOI: [10.1007/BF02740929](https://doi.org/10.1007/BF02740929).
- [103] F. P. An et al. “The Detector System of The Daya Bay Reactor Neutrino Experiment”. In: *Nucl. Instrum. Meth.* A811 (2016), pp. 133–161. DOI: [10.1016/j.nima.2015.11.144](https://doi.org/10.1016/j.nima.2015.11.144). arXiv: [1508.03943](https://arxiv.org/abs/1508.03943) [physics.ins-det].
- [104] C. A. Duba et al. “HALO: The helium and lead observatory for supernova neutrinos”. In: *J. Phys. Conf. Ser.* 136 (2008), p. 042077. DOI: [10.1088/1742-6596/136/4/042077](https://doi.org/10.1088/1742-6596/136/4/042077).
- [105] Pagliaroli G. Fafone V. Katsavounidis E. *GWnu Memorandum of Understanding*.
- [106] M. Szczepanczyk. “Multimessenger Astronomy with Gravitational Waves from Core-Collapse Supernovae”. In: (2018).
- [107] D. S. Ayres et al. “The NOvA Technical Design Report”. In: (2007). DOI: [10.2172/935497](https://doi.org/10.2172/935497).

Bibliography

- [108] B. Abbott et al. “Search for gravitational waves associated with 39 gamma-ray bursts using data from the second, third, and fourth LIGO runs”. In: *Phys. Rev. D* 77 (6 2008), p. 062004. DOI: [10.1103/PhysRevD.77.062004](https://doi.org/10.1103/PhysRevD.77.062004). URL: <https://link.aps.org/doi/10.1103/PhysRevD.77.062004>.
- [109] S Adrián-Martínez et al. “A first search for coincident gravitational waves and high energy neutrinos using LIGO, Virgo and ANTARES data from 2007”. In: *Journal of Cosmology and Astroparticle Physics* 2013.06 (2013), pp. 008–008. DOI: [10.1088/1475-7516/2013/06/008](https://doi.org/10.1088/1475-7516/2013/06/008). URL: <https://doi.org/10.1088/1475-7516/2013/06/008>.
- [110] Irene Di Palma. “Multimessenger astrophysics: When gravitational waves meet high energy neutrinos”. In: *Nuclear Instruments and Methods in Physics Research Section A: Accelerators, Spectrometers, Detectors and Associated Equipment* 742 (2014). 4th Roma International Conference on Astroparticle Physics, pp. 124 –129. ISSN: 0168-9002. DOI: <https://doi.org/10.1016/j.nima.2013.10.076>. URL: <http://www.sciencedirect.com/science/article/pii/S0168900213014836>.
- [111] Gravitational Wave Open Science Center. URL: <https://losc.ligo.org/mysources/>.
- [112] WebPlotDigitizer 4.2. URL: <https://apps.automeris.io/wpd/>.
- [113] P. Bagley et al. “KM3NeT: Technical Design Report for a Deep-Sea Research Infrastructure in the Mediterranean Sea Incorporating a Very Large Volume Neutrino Telescope”. In: (2009).
- [114] Illustration of ANTARES telescope. URL: <https://tinyurl.com/y3gosdmr>.
- [115] HEN plot. URL: <https://dcc.ligo.org/cgi-bin/DocDB/ShowDocument?docid=p1200006>.

Bibliography

- [116] I Leonor et al. “Searching for prompt signatures of nearby core-collapse supernovae by a joint analysis of neutrino and gravitational wave data”. In: *Classical and Quantum Gravity* 27.8 (2010), p. 084019. DOI: [10.1088/0264-9381/27/8/084019](https://doi.org/10.1088/0264-9381/27/8/084019). URL: <https://doi.org/10.1088%2F0264-9381%2F27%2F8%2F084019>.
- [117] Samantha A. Usman et al. “The PyCBC search for gravitational waves from compact binary coalescence”. In: *Class. Quant. Grav.* 33.21 (2016), p. 215004. DOI: [10.1088/0264-9381/33/21/215004](https://doi.org/10.1088/0264-9381/33/21/215004). arXiv: [1508.02357](https://arxiv.org/abs/1508.02357) [gr-qc].
- [118] Cody Messick et al. “Analysis Framework for the Prompt Discovery of Compact Binary Mergers in Gravitational-wave Data”. In: *Phys. Rev. D* 95.4 (2017), p. 042001. DOI: [10.1103/PhysRevD.95.042001](https://doi.org/10.1103/PhysRevD.95.042001). arXiv: [1604.04324](https://arxiv.org/abs/1604.04324) [astro-ph.IM].
- [119] C. Casentini et al. “Pinpointing astrophysical bursts of low-energy neutrinos embedded into the noise”. In: *JCAP* 1808.08 (2018), p. 010. DOI: [10.1088/1475-7516/2018/08/010](https://doi.org/10.1088/1475-7516/2018/08/010). arXiv: [1801.09062](https://arxiv.org/abs/1801.09062) [astro-ph.HE].
- [120] Mathias Th. Keil, Georg G. Raffelt, and Hans-Thomas Janka. “Monte Carlo Study of Supernova Neutrino Spectra Formation”. In: *The Astrophysical Journal* 590.2 (2003), pp. 971–991. DOI: [10.1086/375130](https://doi.org/10.1086/375130). URL: <https://doi.org/10.1086%2F375130>.
- [121] Irene Tamborra et al. “Flavor-dependent Neutrino Angular Distribution in Core-collapse Supernovae”. In: *The Astrophysical Journal* 839.2 (2017), p. 132. DOI: [10.3847/1538-4357/aa6a18](https://doi.org/10.3847/1538-4357/aa6a18). URL: <https://doi.org/10.3847%2F1538-4357%2Faa6a18>.
- [122] Francesco Vissani. “Comparative analysis of SN1987A antineutrino fluence”. In: *Journal of Physics G: Nuclear and Particle Physics* 42.1 (2014), p. 013001. DOI: [10.1088/0954-3899/42/1/013001](https://doi.org/10.1088/0954-3899/42/1/013001). URL: <https://doi.org/10.1088%2F0954-3899%2F42%2F1%2F013001>.

Bibliography

- [123] Alessandro Mirizzi et al. “Supernova Neutrinos: Production, Oscillations and Detection”. In: *Riv. Nuovo Cim.* 39.1-2 (2016), pp. 1–112. DOI: [10.1393/ncr/i2016-10120-8](https://doi.org/10.1393/ncr/i2016-10120-8). arXiv: 1508.00785 [astro-ph.HE].
- [124] Cecilia Lunardini and Alexei Yu Smirnov. “Probing the neutrino mass hierarchy and the 13-mixing with supernovae”. In: *Journal of Cosmology and Astroparticle Physics* 2003.06 (2003), pp. 009–009. DOI: [10.1088/1475-7516/2003/06/009](https://doi.org/10.1088/1475-7516/2003/06/009). URL: <https://doi.org/10.1088/1475-7516/2003/06/009>.
- [125] M. Tanabashi et al. “Review of Particle Physics”. In: *Phys. Rev.* D98.3 (2018), p. 030001. DOI: [10.1103/PhysRevD.98.030001](https://doi.org/10.1103/PhysRevD.98.030001).
- [126] K. Abe et al. “Observation of Electron Neutrino Appearance in a Muon Neutrino Beam”. In: *Phys. Rev. Lett.* 112 (2014), p. 061802. DOI: [10.1103/PhysRevLett.112.061802](https://doi.org/10.1103/PhysRevLett.112.061802). arXiv: 1311.4750 [hep-ex].
- [127] K. Abe et al. “Real-time supernova neutrino burst monitor at Super-Kamiokande”. In: *Astroparticle Physics* 81 (2016), pp. 39–48. ISSN: 0927-6505. DOI: <https://doi.org/10.1016/j.astropartphys.2016.04.003>. URL: <http://www.sciencedirect.com/science/article/pii/S0927650516300457>.
- [128] Kenichiro Nakazato et al. “SUPERNOVA NEUTRINO LIGHT CURVES AND SPECTRA FOR VARIOUS PROGENITOR STARS: FROM CORE COLLAPSE TO PROTO-NEUTRON STAR COOLING”. In: *The Astrophysical Journal Supplement Series* 205.1 (2013), p. 2. DOI: [10.1088/0067-0049/205/1/2](https://doi.org/10.1088/0067-0049/205/1/2). URL: <https://doi.org/10.1088/0067-0049/205/1/2>.
- [129] Odysse Halim et al. “Expanding Core-Collapse Supernova Search Horizon of Neutrino Detectors”. In: *Journal of Physics: Conference Series* 1468 (2020), p. 012154. DOI: [10.1088/1742-6596/1468/1/012154](https://doi.org/10.1088/1742-6596/1468/1/012154). URL: <https://doi.org/10.1088/1742-6596/1468/1/012154>.

Bibliography

- [130] Topics in Astroparticle and Underground Physics. URL: <http://taup2019.icrr.u-tokyo.ac.jp/>.
- [131] Matlab Gamma Distribution formula. URL: <https://it.mathworks.com/help/stats/gamma-distribution.html>.
- [132] Matlab Generalized Extreme Value (GEV) Distribution formula. URL: <https://bit.ly/2n1mc2j>.
- [133] Matlab Burr Type XII Distribution formula. URL: <https://it.mathworks.com/help/stats/burr-type-xii-distribution.html>.
- [134] G. Pagliaroli et al. "Neutrinos from Supernovae as a Trigger for Gravitational Wave Search". In: *Phys. Rev. Lett.* 103 (2009), p. 031102. DOI: [10.1103/PhysRevLett.103.031102](https://doi.org/10.1103/PhysRevLett.103.031102). arXiv: [0903.1191](https://arxiv.org/abs/0903.1191) [hep-ph].
- [135] Sean M. Carroll. *Spacetime and geometry: An introduction to general relativity*. 2004. ISBN: 0805387323, 9780805387322. URL: <http://www.slac.stanford.edu/spires/find/books/www?cl=QC6:C37:2004>.